TACTILE SENSATION IMAGING SYSTEM AND ALGORITHMS FOR TUMOR DETECTION

A Dissertation
Submitted to
the Temple University Graduate Board

---

in Partial Fulfillment
of the Requirements for the Degree
DOCTOR OF PHILOSOPHY

---

by
Jong-Ha Lee
August, 2011

Examining Committee Members:

Chang-Hee Won, Advisory Chair, Electrical and Computer Engineering
Joseph Picone, Electrical and Computer Engineering
Saroj Biswas, Electrical and Computer Engineering
Kurosh Darvish, Mechanical Engineering
Shan Lin, Computer and Information Sciences

ACKNOWLEDGEMENTS

I would like to extend my heart-felt gratitude to my adviser, Dr. Chang-Hee Won of the Electrical and Computer Engineering Department at Temple University. He was an unending source of patience, advice, and encouragement during my years of study. Dr. Chang-Hee Won encouraged me to grow as an engineer and to become an independent thinker. I am fortunate to have had an adviser who gave me constant support while encouraging my independence and self-sufficiency. Dr. Chang-Hee Won taught me to express my individuality while providing a strong foundation on which to rely. His mentorship inspired me to become well-rounded in my studies, supporting me as I formulated and worked towards my long-term goals.

I also wish to offer my thanks to Dr. Joseph Picone, Dr. Saroj Biswas, Dr. Kurosh Darvish, and Dr. Shan Lin, the other members of my doctoral committee at Temple University. Words cannot express the value of their guidance, comments, and suggestions.

In addition, I would like to thank my labmates. I especially appreciate the friendship of Dr. Bei Kang and Firdous Saleheen as we often found ourselves working closely to answer the same questions, and gave each other encouragement.

I would also like to thank my parents, Soo-Kon Lee and Young-Soo Kim, for having faith in me and encouraging me to fulfill all my ambitious dreams. Their drive for success and willingness to tackle challenges gave me wonderful examples with which to build my own professional and personal life. I would also like to take this opportunity to thank my wife's parents, Byung-Oh Cho and Bok Im, who offered their help and encouragement throughout this endeavor. My friends, Kyung Jun Park and Young Woo Shin, and their families must also be mentioned. Their ongoing support helped me to successfully complete my studies.

Most of all, I want to thank my wife, Yun-Sook Cho, for loving and supporting me throughout the development of this work. Her quiet patience, support, and encouragement were given with unfaltering love, and became the firm ground on which I have built the past five years. Her near-infinite forbearance of my occasional bad mood is a testament of a partner with unlimited love and devotion.

Finally, I would like to extend my thanks for the financial support from National Science Foundation ECS-0554748 and ECCS-0969430, Pennsylvania Department of Health, Tobacco Formula Fund, and the Office of the Senior Vice Provost for Research and Graduate Education at Temple University.

ABSTRACT

Diagnosing early formation of tumors or lumps, particularly those caused by cancer, has been a challenging problem. To help physicians detect tumors more efficiently, various imaging techniques with different imaging modalities such as computer tomography, ultrasonic imaging, nuclear magnetic resonance imaging, and mammography, have been developed. However, each of these techniques has limitations, including exposure to radiation, excessive costs, and complexity of machinery. Tissue elasticity is an important indicator of tissue health, with increased stiffness pointing to an increased risk of cancer. In addition to increased tissue elasticity, geometric parameters such as size of a tissue inclusion are also important factors in assessing the tumor. The combined knowledge of tissue elasticity and its geometry would aid in tumor identification. In this research, we present a tactile sensation imaging system (TSIS) and algorithms which can be used for practical medical diagnostic experiments for measuring stiffness and geometry of tissue inclusion. The TSIS incorporates an optical waveguide sensing probe unit, a light source unit, a camera unit, and a computer unit. The optical method of total internal reflection phenomenon in an optical waveguide is adapted for the tactile sensation imaging principle. The light sources are attached along the edges of the waveguide and illuminates at a critical angle to totally reflect the light within the waveguide. Once the waveguide is deformed due to the stiff object, it causes the trapped light to change the critical angle and diffuse outside the waveguide. The scattered light is captured by a camera. To estimate various target parameters, we develop the tactile data processing algorithm for the target elasticity measurement via direct contact. This algorithm is accomplished by adopting a new non-rigid point matching algorithm called "topology preserving relaxation labeling (TPRL)." Using this algorithm, a series of tactile data is registered and strain information is calculated. The stress information is measured through the summation of pixel values of the tactile data. The stress and strain measurements are used to estimate the elasticity of the touched object. This method is validated by commercial soft polymer samples with a known Young's modulus. The experimental results show that using the TSIS and its algorithm, the elasticity of the touched object is estimated within 5.38% relative estimation error. We also develop a tissue inclusion parameter estimation method via indirect contact for the characterization of tissue inclusion. This method includes developing a forward algorithm and an inversion algorithm. The finite element modeling (FEM) based forward algorithm is designed to comprehensively predict the tactile data based on the parameters of an inclusion in the soft tissue. This algorithm is then used to develop an artificial neural network (ANN) based inversion algorithm for extracting various characteristics of tissue inclusions, such as size, depth, and Young's modulus. The estimation method is then validated by using realistic tissue phantoms with stiff inclusions. The experimental results show that the minimum relative estimation errors for the tissue inclusion size, depth, and hardness are 0.75%, 6.25%, and 17.03%, respectively. The work presented in this dissertation is the initial step towards early detection of malignant breast tumors.

TABLE OF CONTENTS

Page

ACKNOWLEDGEMENTS . . . ii

ABSTRACT . . . iv

LIST OF FIGURES . . . viii

CHAPTER

1 INTRODUCTION . . . 1
- 1.1 Contributions . . . 4
- 1.2 Dissertation Scope and Outline . . . 4

2 BACKGROUND AND LITERATURE REVIEW . . . 7
- 2.1 Human Tactile Sensing Mechanism . . . 7
  - 2.1.1 Tissue Structure . . . 7
  - 2.1.2 Mechanoreceptor Functionality . . . 8
- 2.2 Artificial Tactile Sensors . . . 9
  - 2.2.1 Capacitive Sensors . . . 9
  - 2.2.2 Piezoresistive Sensors . . . 10
  - 2.2.3 Piezoelectric Sensors . . . 11
  - 2.2.4 Magnetic-Based Sensors . . . 11
  - 2.2.5 Optical Sensors . . . 12
- 2.3 Elasticity Determination System . . . 13
  - 2.3.1 Elastography . . . 13
  - 2.3.2 Elasticity Imaging Using Tactile Sensors . . . 15
- 2.4 Application of Breast Tumor Detection . . . 18

3 TACTILE SENSATION IMAGING PRINCIPLE AND NUMERICAL SIMULATIONS . . . 24
- 3.1 Total Internal Reflection . . . 24
- 3.2 Analytical Solution: Wave Optics . . . 25
- 3.3 Numerical Simulations: Wave Optics . . . 31
- 3.4 Geometric Optics Approximation . . . 33
- 3.5 Multi-layered Sensing Probe Characterization . . . 36

4 TACTILE SENSATION IMAGING SYSTEM . . . 40
- 4.1 Overview of Tactile Sensation Imaging System . . . 40
- 4.2 Hardware Design of Tactile Sensation Imaging System . . . 41
  - 4.2.1 Components . . . 41
  - 4.2.2 Optical Waveguide Fabrication . . . 43
- 4.3 Software Implementation of Tactile Sensation Imaging System . . . 44
  - 4.3.1 Overview . . . 44

4.3.2 Procedure and Functionality of TSIS Software . . . 45
4.4 Sample Tactile Images . . . 48
4.5 The Specification of the Tactile Sensation Imaging System . . . 49

5 TARGET HARDNESS ESTIMATION BY DIRECT CONTACT . . . 51
5.1 Stress Estimation . . . 51
5.2 Strain Estimation . . . 55
5.2.1 Problem Definition . . . 56
5.2.2 Topology Preserving Relaxation Labeling (TPRL) algorithm . . . 59
5.2.3 Searching Point Correspondence . . . 60
5.2.4 Transformation Function . . . 63
5.2.5 Validation and Performance Evaluation . . . 65
5.3 Young's Modulus Estimation from Stress and Strain . . . 73
5.4 Experimental Results . . . 74
5.5 Discussions . . . 75

6 TISSUE INCLUSION PARAMETER ESTIMATION BY INDIRECT CONTACT . . . 78
6.1 Problem Formulation . . . 78
6.2 Relative Tissue Inclusion Parameter Estimation . . . 79
6.2.1 Relative Size Estimation Method . . . 79
6.2.2 Relative Size Estimation Experimental Results . . . 80
6.2.3 Relative Depth Estimation Method . . . 82
6.2.4 Relative Depth Estimation Experimental Results . . . 84
6.2.5 Relative Hardness Estimation Method . . . 86
6.2.6 Relative Hardness Estimation Experimental Results . . . 86
6.2.7 Other Tissue Inclusion Parameters – Shape and Mobility . . . 89
6.3 Absolute Tissue Inclusion Parameter Estimation . . . 90
6.3.1 Forward Algorithm . . . 91
6.3.2 Mapping Tactile Data . . . 94
6.3.3 Inversion Algorithm . . . 95
6.3.4 Experimental Results . . . 96
6.4 Sensitivity and Specificity Test . . . 99
6.5 Discussions . . . 101

7 CONCLUSIONS AND FUTURE WORK . . . 104
7.1 Conclusions . . . 104
7.2 Future Work . . . 106

REFERENCES . . . 109

LIST OF FIGURES

1.1 THE GRAPHICAL OVERVIEW OF THE DISSERTATION SCOPE. 5

2.1 THE STRUCTURE OF THE SKIN AND LOCATION OF ITS PRIMARY MECHANORECEPTORS. 8

2.2 THE SCHEMATIC OF CAPACITIVE SENSOR (Najarian et al., 2009). 10

2.3 THE SCHEMATIC OF PIEZORESISTIVE SENSOR (Najarian et al., 2009). 11

2.4 THE SCHEMATIC OF PIEZOELECTRIC SENSOR. (A) RANDOMLY DIRECTED DIPOLES IN CERAMIC STRUCTURE (Najarian et al., 2009). (B) ALIGNMENT OF DIPOLES IN THE DIRECTION OF APPLIED ELECTRIC FIELD (Najarian et al., 2009). 12

2.5 THE ULTRASONIC ELASTOGRAPHY SYSTEM AND ITS IMAGE SAMPLE. (A) THE CONVENTIONAL ULTRASONIC ELASTOGRAPHY MODALITY (Siemens, 2011), (B) THE BREAST ELASTOGRAM (Siemens, 2011). 14

2.6 THE SURETOUCH VISUAL MAPPING SYSTEM OF MEDICAL TACTILE INC (Medical-Tactile, 2011). 16

2.7 THE PIEZOELECTRIC FINGER USING PIEZOELECTRIC ZIRCONATE TITANATE (PZT) (Yegingil et al., 2010). 17

2.8 THE EXAMPLE OF THE BREAST SELF-EXAMINATION. (A) THE PATTERN OF SEARCH, (B) THE PALPATION METHOD. 19

2.9 THE MAMMOGRAPHY MODALITY AND ITS IMAGE SAMPLE. (A) THE CONVENTIONAL MAMMOGRAM MODALITY (Mommography, 2011), (B) THE BREAST MAMMOGRAPHY (Mommography, 2011). 20

2.10 THE ULTRASOUND IMAGING MODALITY AND ITS IMAGE SAMPLE. (A) THE CONVENTIONAL ULTRASOUND MODALITY (Ultrasound, 2011), (B) THE BREAST ULTRASOUND IMAGE (Ultrasound, 2011). 21

2.11 THE MAGNETIC RESONANCE IMAGING MODALITY AND ITS IMAGE SAMPLE. (A) THE CONVENTIONAL MAGNETIC RESONANCE IMAGING MODALITY (MRI, 2011), (B) THE BREAST MAGNETIC RESONANCE IMAGE (MRI, 2011). 22

2.12 THE THERMOGRAPHY IMAGING MODALITY AND ITS IMAGE SAMPLE. (A) THE CONVENTIONAL THERMOGRAPHY IMAGING MODALITY (Thermography, 2011), (B) THE BREAST THERMOGRAPHY IMAGE (Thermography, 2011). 22

3.1 THE SNELL'S LAW DESCRIPTION. (A) THE INCIDENCE ANGLE IS SMALLER THAN THE CRITICAL ANGLE. (B) THE ANGLE OF INCIDENCE IS EQUAL TO THE CRITICAL ANGLE. (C) THE ANGLE OF INCIDENCE IS BIGGER THAN THE CRITICAL ANGLE. . . 25

3.2 THE SCHEMATIC DIAGRAM OF THE TACTILE SENSATION IMAGING PRINCIPLE. (A) THE LIGHT IS INJECTED INTO THE WAVEGUIDE TO TOTALLY REFLECT. (B) THE LIGHT SCATTERS AS THE WAVEGUIDE DEFORMS DUE TO THE EXTERNAL FORCE PRESENTED BY A STIFF OBJECT. 26

3.3 THE SCHEMATIC DIAGRAM OF THE MULTI-LAYERED OPTICAL WAVEGUIDE. THE WAVEGUIDE CONSISTS OF THREE DIFFERENT DENSITIES OF POLYDIMETHYLSILOXANE (PDMS) LAYERS AND ONE GLASS PLATE LAYER. THE WAVEGUIDE IS SURROUNDED BY AIR. 26

3.4 (A) THE MULTI-LAYERED OPTICAL WAVEGUIDE SENSING PROBE AS SEEN FROM ITS SIDE. (B) THE LIGHT PROPAGATION UNDER THE TOTAL INTERNAL REFLECTION IN THE WAVEGUIDE. 32

3.5 (A) THE MULTI-LAYERED WAVEGUIDE WITH SMALL DEFORMATION AT A DISTANCE OF 1000 MM AS SEEN FROM ITS SIDE. (B) THE LIGHT DISPERSION IN THE WAVEGUIDE. NOTICE THAT SCATTERING LIGHTS GOING OUT OF THE WAVEGUIDE AT A DISTANCE OF 1000 MM. 33

3.6 THE SCATTERED LIGHT CAPTURED FROM THE TOP SURFACE OF THE WAVEGUIDE WHEN (A) THE WAVEGUIDE IS VERTICALLY DEFORMED WITH 0 MM DEFORMATION DEPTH, (B) THE WAVEGUIDE IS VERTICALLY DEFORMED WITH 2 MM DEFORMATION DEPTH, (C) THE WAVEGUIDE IS VERTICALLY DEFORMED WITH 4 MM DEFORMATION DEPTH (D) THE WAVEGUIDE IS VERTICALLY DEFORMED WITH 6 MM DEFORMATION DEPTH. 34

3.7 GRAPHIC REPRESENTATION OF LIGHT PROPAGATION AS A RAY, PROPAGATING IN THE WAVEGUIDE AT PROPAGATION ANGLES γ_I, $I = 0, 1, 2, 3, 4, 5$. 35

3.8 THE SCHEMATIC OF THE THREE-LAYERED SENSING PROBE. 36

3.9 MAXIMUM DEFORMATION OF SENSING PROBE WHEN THE UNIFORM FORCE F IS APPLIED TO THE SURFACE OF SENSING PROBE. 38

3.10 DEFORMATION AREA OF SENSING PROBE WHEN THE UNIFORM FORCE F IS APPLIED TO THE SURFACE OF SENSING PROBE. 39

4.1 THE DESIGN OVERVIEW OF THE TACTILE SENSATION IMAGING SYSTEM. 40

4.2 DESIGN SCHEMATIC. 42

4.3 THE FABRICATED OPTICAL WAVEGUIDE SENSING PROBE. THE OPTICAL WAVEGUIDE IS FLEXIBLE AND TRANSPARENT. (A) THE SAMPLE OF OPTICAL WAVEGUIDE, (B) THE OPTICAL WAVEGUIDE WITH LED LIGHT INJECTION. 44

4.4 THE BLOCK DIAGRAM OF THE SOFTWARE ARCHITECTURE. 45

4.5 INITIAL WINDOW OF TACTILE SENSATION IMAGING SYSTEM SOFTWARE. 46

4.6 THE GRAPHICAL USER INTERFACE OF TACTILE SENSATION IMAGING SYSTEM SOFTWARE. 46

4.7 THE TACTILE IMAGING EXPERIMENTS FOR A TISSUE INCLUSION. (A) OBTAINING TACTILE IMAGE OF A TISSUE INCLUSION USING TSIS, (B) RAW GRAY-SCALE TACTILE IMAGE, (C) COLOR VISUALIZATION WITH 3-D RECONSTRUCTION. 48

5.1 THE LOADING MACHINE EXPERIMENT SETUP. THIS SETUP IS USED TO FIND THE RELATIONSHIP BETWEEN THE NORMAL FORCE AND THE SUMMATION OF PIXEL VALUES IN TACTILE DATA. 52

5.2 THE PIXEL VALUE ALONG THE CONTACT AREA (HORIZONTAL DIRECTION) AS THE NORMAL FORCE VARIES. 53

5.3 THE RELATIONSHIP CURVE BETWEEN THE NORMAL FORCE AND THE SUMMATION OF PIXEL VALUES IN TACTILE DATA. 54

5.4 THE RELATIONSHIP BETWEEN THE NORMAL FORCE AND SUMMATION OF PIXEL VALUES IN TACTILE DATA IN RESPONSE TO THE DIFFERENT LOADING MACHINE TIP RADIUS. 55

5.5 TRACKING CONTROL POINTS EXTRACTED FROM SURFACE OF TWO DIFFERENT TACTILE DATA TO ESTIMATE THE STRAIN. 56

5.6 THE DISTANCE AND ANGLE COMPUTATION. (A) DIAGRAM OF LOG-POLAR BINS USED IN COMPUTING THE DISTANCE AND ANGLE. WE USE 5 BINS FOR THE DISTANCES AND 12 BINS FOR THE ANGLES. (B) A POINT $S_I \in S$ (BLACK) FROM THE FISH SHAPE WITH ITS SETS $\mathcal{DS}(S_I)$ AND $\mathcal{ANG}(S_I)$ OF ITS 6 ADJACENT POINTS IN S. (C) THE POINT $T_J \in T$ (BLACK) IN THE DEFORMED FISH SHAPE WHICH HAVE 6 ADJACENT POINTS AND ITS DISTANCE AND ANGLE SETS $\mathcal{DS}(T_J)$ AND $\mathcal{ANG}(T_J)$. . . 61

5.7 THE GENERAL CASE OF THE CORRELATION STRENGTH DEPENDS ON THE DIFFERENCES OF DISTANCE AND ANGLE BETWEEN POINT PAIRS. THE SIMILARITY CONSTRAINTS α, β AND THE SPATIAL SMOOTHNESS CONSTRAINT γ COMPRISE THE FINAL COMPATIBILITY COEFFICIENT FOR THE RELAXATION LABELING PROCESS. 62

5.8 SYNTHESIZED ORIGINAL DATA SETS FOR STATISTICAL TESTS. (A) FISH SHAPE. (B) CHINESE CHARACTER SHAPE. 66

5.9 SYNTHESIZED DEFORMATION DATA SETS FOR STATISTICAL TESTS. (A) FISH SHAPE. (B) CHINESE CHARACTER SHAPE. 66

5.10 SYNTHESIZED NOISE DATA SETS FOR STATISTICAL TESTS. (A) FISH SHAPE. (B) CHINESE CHARACTER SHAPE. 67

5.11 SYNTHESIZED OUTLIER DATA SETS FOR STATISTICAL TESTS. (A) FISH SHAPE. (B) CHINESE CHARACTER SHAPE. 67

5.12 SYNTHESIZED ROTATION DATA SETS FOR STATISTICAL TESTS. (A) FISH SHAPE. (B) CHINESE CHARACTER SHAPE. 67

5.13 SYNTHESIZED OCCLUSION DATA SETS FOR STATISTICAL TESTS. (A) FISH SHAPE. (B) CHINESE CHARACTER SHAPE. 68

5.14 COMPARISON OF THE MATCHING PERFORMANCE OF TPRL (▼) WITH SHAPE CONTEXT (■), TPS-RPM ($*$), RPM-LNS (♦), AND CPD (·). (A) FISH SHAPE DEFORMATION TEST. (B) CHARACTER SHAPE DEFORMATION TEST. 69

5.15 COMPARISON OF THE MATCHING PERFORMANCE OF TPRL (▼) WITH SHAPE CONTEXT (■), TPS-RPM ($*$), RPM-LNS (♦), AND CPD (·). (A) FISH SHAPE NOISE TEST. (B) CHARACTER SHAPE NOISE TEST. 69

5.16 COMPARISON OF THE MATCHING PERFORMANCE OF TPRL (▼) WITH SHAPE CONTEXT (■), TPS-RPM ($*$), RPM-LNS (♦), AND CPD (·). (A) FISH SHAPE OUTLIER TEST. (B) CHARACTER SHAPE OUTLIER TEST. 70

5.17 COMPARISON OF THE MATCHING PERFORMANCE OF TPRL (▼) WITH SHAPE CONTEXT (■), TPS-RPM ($*$), RPM-LNS (♦), AND CPD (·). (A) FISH SHAPE ROTATION TEST. (B) CHARACTER SHAPE ROTATION TEST. 70

5.18 COMPARISON OF THE MATCHING PERFORMANCE OF TPRL (▼) WITH SHAPE CONTEXT (■), TPS-RPM ($*$), RPM-LNS (♦), AND CPD (·). (A) FISH SHAPE OCCLUSION TEST. (B) CHARACTER SHAPE OCCLUSION TEST. 71

5.19 SEQUENCE IMAGES OF TOY HOTEL. (A) FRAMES 0, (B) FRAMES 10, (C) FRAMES 20, (D) FRAMES 30, (E) FRAMES 40, (F) FRAMES 50, (G) FRAMES 60, (H) FRAMES 70, (I) FRAMES 80, (J) FRAMES 90, (J) FRAMES 100. 71

5.20 COMPARISON OF THE MATCHING PERFORMANCE OF TPRL (▼) WITH SHAPE CONTEXT (■), TPS-RPM ($*$), RPM-LNS (♦), AND CPD (·) IN THE HOTEL SEQUENCE FOR INCREASING FRAME SEPARATION AND DIFFERENT OCCLUSION RATIO [(A) 0.0, (B) 0.1, (C) 0.2, (D) 0.3]. ERROR BARS CORRESPOND TO THE STANDARD DEVIATION OF EACH PAIR'S RMS ERROR. 72

5.21 ROBUSTNESS TEST ON LARGE DATA SET. (A) A STRAW IMAGE AND (B) 1000 POINTS EXTRACTED FROM THE STRAW IMAGE. 73

5.22 CONTROL POINTS EXTRACTED FROM TWO TACTILE DATA OBTAINED UNDER DIFFERENT LOADING FORCES ON THE SAME OBJECT. (A) BEFORE POINT MATCHING, (B) AFTER POINT MATCHING. 74

5.23 THE HARDNESS ESTIMATION RESULTS OF SOFT POLYMERS, CL2000X AND CL2003X. 75

6.1 THE CROSS-SECTION OF AN IDEALIZED BREAST TISSUE MODEL FOR ESTIMATING INCLUSION PARAMETERS. THE TISSUE INCLUSION HAS THREE PARAMETERS – DIAMETER D, DEPTH H, AND HARDNESS E. 79

6.2 THE SCHEMATIC OF THE SIZE PHANTOM. 81

6.3 THE MANUFACTURED SIZE PHANTOM. 81

6.4 THE TACTILE DATA OF THREE INCLUSIONS EMBEDDED IN THE SIZE PHANTOM. (A) 2 MM SIZE INCLUSION, (B) 8 MM SIZE INCLUSION, (C) 14 MM SIZE INCLUSION. . 81

6.5 ERROR BAR CHART OF ESTIMATED RELATIVE DIAMETER OF EACH INCLUSION. . . 82

6.6 DEFINITION OF MOMENT OF A FORCE. 82

6.7 N POINT MASSES SITUATED ALONG A HORIZONTAL LINE. 83

6.8 THE SCHEMATIC OF THE DEPTH PHANTOM. 84

6.9 THE MANUFACTURED DEPTH PHANTOM. 85

6.10 THE TACTILE DATA OF THREE INCLUSIONS EMBEDDED IN THE DEPTH PHANTOM. (A) 4 MM DEPTH INCLUSION, (B) 8 MM DEPTH INCLUSION, (C) 12 MM DEPTH INCLUSION. 85

6.11 ERROR BAR CHART OF ESTIMATED RELATIVE DEPTH OF EACH INCLUSION. 85

6.12 THE SCHEMATIC OF THE HARDNESS PHANTOM. 87

6.13 THE MANUFACTURED HARDNESS PHANTOM. 87

6.14 THE TACTILE DATA OF THREE INCLUSIONS EMBEDDED IN THE HARDNESS PHANTOM. (A) 40 KPA YOUNG'S MODULUS INCLUSION, (B) 70 KPA YOUNG'S MODULUS INCLUSION, (C) 100 KPA YOUNG'S MODULUS INCLUSION. 88

6.15 ERROR BAR CHART OF ESTIMATED RELATIVE HARDNESS OF EACH INCLUSION. . . 88

6.16 THE FEM MODEL OF AN IDEALIZED BREAST TISSUE MODEL. THE SENSING PROBE OF TSIS IS ALSO MODELED ON TOP OF THE BREAST TISSUE MODEL. IN FEM, THE DEFORMED SHAPE OF THE SENSING PROBE IS CAPTURED AS MAXIMUM DEFORMATION, TOTAL DEFORMATION, AND DEFORMATION AREA. 91

6.17 THE DIAGRAM OF INPUT VARIABLES (D, H, E) AND OUTPUT VARIABLES (O^1_{FEM}, O^2_{FEM}, O^3_{FEM}) IN FORWARD ALGORITHM. 92

6.18 (A) THE MAXIMUM DEFORMATION O^1_{FEM}, (B) TOTAL DEFORMATION VALUE O^2_{FEM}, (C) DEFORMATION AREA O^3_{FEM} OF TSIS SENSING PROBE DEPENDING ON THE INCLUSION SIZE D, DEPTH H, AND YOUNG'S MODULUS E. THE 4-D DIMENSION SHOWS THE MAXIMUM DEFORMATION VALUE O^1_{FEM}, RESCALED FROM 0 TO 255. . 93

6.19 THE LINEAR REGRESSION RESULTS BETWEEN FEM TACTILE DATA AND TSIS TACTILE DATA. (A) THE LINEAR REGRESSION RESULT BETWEEN MAXIMUM DEFORMATION O^1_{FEM} AND MAXIMUM PIXEL VALUE O^1_{TSIS}, (B) THE LINEAR REGRESSION RESULT BETWEEN TOTAL DEFORMATION O^2_{FEM} AND TOTAL PIXEL VALUE O^2_{TSIS}, (C) THE LINEAR REGRESSION RESULT BETWEEN DEFORMATION AREA O^3_{FEM} AND DEFORMATION AREA OF PIXEL O^3_{TSIS}. 95

6.20 THE DIAGRAM OF INPUT VARIABLES AND OUTPUT VARIABLES IN INVERSION ALGORITHM. 96

6.21 THE MULTI-LAYERED ARTIFICIAL NEURAL NETWORK STRUCTURE. 97

6.22 THE MEAN SQUARE ERROR OF INCLUSION'S PARAMETER ESTIMATION OVER 100 EXPERIMENTS. (A) INCLUSION SIZE CASE, (B) INCLUSION DEPTH CASE, (C) INCLUSION HARDNESS CASE. 98

6.23 RECEIVER OPERATING CHARACTERISTIC (ROC) CURVE OF TSIS. 100

CHAPTER 1
INTRODUCTION

Tactile sensation, or touch sensation, is the information produced by mechanoreceptors in the skin. When a fingertip presses onto an object, pressure information is induced at the interface by mechanoreceptors. Sensing and processing this pressure information provides humans with a rich source of information about the physical environment. This information can be used for object detection and characterization through the determination of object size, shape, temperature, and hardness (Lee, 2000), (Fearing, 1990).

Much as they are for humans, the measurement and processing of tactile information have been shown to be of great importance in many applications, such as robotic systems or medical devices. A number of articles provide reviews of the tactile sensors in the robotic field (Hosoda et al., 2006), (Beebe et al., 1995), (Engel et al., 2003), (Futai et al., 2004). Several articles also cover the topic of tactile sensors in minimally invasive surgery and medical diagnostics tools (Howe et al., 1995), (Howe and Matsuoka, 1999), (Dario and Rossi, 1985). The tasks accomplished with tactile data processing may be grouped into two broad categories: object detection and object characterization.

In the first category, many researchers have shown artificial tactile sensing to be useful in executing many tasks of object detection by measuring contact pressure (Lamotte and Srinivasan, 1987). For instance, tactile sensors have been used to detect surface texture (Kim et al., 2005), (Saxena et al., 2008). Object shape and curvature have also been detected with tactile elements array (Fearing and Binford, 1988), (Gupta et al., 2006). Tactile elements have been used as the sensing mechanism for feature recognition algorithms capable of identifying edges, corners, and holes (Zhang and Chen, 2000).

Compared to object detection, object characterization using tactile information has been investigated relatively infrequently. This is because most tactile sensors have a form of pressure sensor array, which makes it difficult to obtain three-dimensional (3-D) tactile data of the contacted object. In addition, high-resolution tactile data are necessary for the precise contact pressure measurement, but the current array type tactile sensor has limitations in tactile resolution. Recently, some tactile sensors that use microelectromechanical systems (MEMS) technology have provided good spatial resolution (Hwang et al., 2007), (Lee et al., 2006). However, in comparison to the human fingertip with its millions of mechanoreceptors per square inch of skin, most tactile sensors have limited resolution. Moreover, the small measurable force range due to the brittle sensing elements, such as piezoresistors, has not proven to be effective in real applications.

It is widely agreed that artificial tactile sensors will play an important role in the future realization of diagnostic devices (Lee et al., 2010b). For instance, artificial tactile sensors can be applicable to early breast tumor warning. This application can be realized based on the observation that breast nodule stiffness is an indicator of breast health, and increased tissue stiffness of nodules points to an increased risk of breast cancer. In fact, palpation of the breast to identify a stiff tumor is an established screening method. This is referred to as breast self examination (BSE) or clinical breast examination (CBE). BSE is still recommended for the early detection of tumors, whereas CBE is performed by a medical specialist and has a sensitivity of over 57% and specificity of 97% (Ratanachaikanont, 2005a). Another study shows that a sensitivity of CBE is approximately 59% and a specificity of CBE is approximately 93% (Bobo et al., 2000). The major drawbacks of BSE and CBE are that the examinations are subjective and the performance is highly dependent upon the healthcare provider. The efficacy of CBE is also limited by the experience of the physician.

To help physicians detect tumors more efficiently, various imaging techniques utilizing different modalities such as computer tomography (CT), ultrasonic imaging (US), magnetic resonance imaging (MRI), and mammography (MG) have been developed (Shojaku et al., 2008), (Fenster and Downey, 1996), (Degani et al., 1997), (Gentle, 1988). However, each of these techniques has disadvantages, such as harmful radiation to the body (CT, MG), low specificity

(MRI), complicated systems (US, MRI), etc. Moreover, these techniques can provide only spatial information on the tumor. They do not directly measure the mechanical characteristics (e.g. stiffness), which are very important in detecting the severity of the tumor (Regini et al., 2010). The use of tissue stiffness helps in differentiating between benign and malignant tumors (Thitaikumar et al., 2008). In addition to increased tissue stiffness, geometric properties such as size and depth of an inclusion are also important factors in assessing the tumor. The combined knowledge of tissue stiffness and its geometry would aid breast tumor identification. Thus, a non-invasive and real-time method using artificial tactile sensors for estimating and recording tissue inclusion properties such as size, depth, and hardness would offer great clinical utility.

The scope of this dissertation is focused on estimating and recording the mechanical properties of biological tissue and tissue inclusion. The primary goal of the research is the development of a new tactile sensor named "tactile sensation imaging system (TSIS)," which can be used for practical medical diagnostic experiments for measuring stiffness and geometry of tissue inclusion. The TSIS incorporates an optical waveguide unit, a light source unit, a camera unit, and a computer unit. The optical waveguide is the main sensing probe of TSIS. The multi-layered polydimethylsiloxane (PDMS) is fabricated for the sensing probe. The mechanical properties of each sensing probe layer have been designed to emulate the biological human tissue layers in order to maximize the touch sensation. The optical method of total internal reflection (TIR) phenomenon in a multi-layered sensing probe has been adapted for the tactile sensation imaging principle. A complementary metal oxide semiconductor (CMOS) camera is used to measure contact pressure resulting from scattered light due to the sensing probe deformation. Since the scattered light is directly captured by a CMOS camera, the tactile resolution is based on the resolution of the camera.

The second goal, which is to develop the tactile data processing algorithm for the target hardness estimation, is accomplished by adopting a new non-rigid point matching algorithm called "topology preserving relaxation labeling (TPRL)." Using this algorithm, a series of tactile data is registered and strain information is calculated. The stress information is measured throughout the integration of pixel values of the tactile data. The stress and strain measurements are taken for unique identification of the elasticity of the touched object. The measurement method is validated by commercial polymer samples with a known hardness.

The third goal is to develop a tissue inclusion parameter estimation method for the characterization of tissue inclusion. This includes the developing a forward algorithm and an inversion algorithm. The finite element modeling (FEM) based forward algorithm is designed to comprehensively predict the tactile data based on the parameters of an inclusion in the soft tissue. This algorithm is then used to develop an artificial neural network (ANN) based inversion algorithm for extracting various characteristics of tissue inclusions, such as size, depth, and hardness. The estimation method is then validated by using realistic tissue phantoms with stiff inclusions.

1.1 Contributions

The major contributions of this dissertation are as follows.

• A new tactile sensation imaging apparatus for detecting the touched object via TIR imaging principle is presented.

• A new approach to estimating the elasticity of the touched object based on registering the series of tactile data is developed and tested.

• A new approach to estimating tissue inclusion parameters such as size, depth, and hardness by the forward and inversion algorithms is developed and validated.

• Evaluation of tactile sensation imaging method for tissue inclusion detection and characterization tasks in a realistic tissue phantom is conducted.

1.2 Dissertation Scope and Outline

The primary goal of this dissertation is the development of a tactile sensation imaging apparatus together with its algorithms for tumor detection. The graphical overview of this dissertation scope is given in Fig. 1.1

The document is composed of seven chapters, this being the first. In Chapter 2, a review of relevant tactile sensing mechanisms is presented, followed by a discussion of current artificial tactile sensors and elasticity determination systems developed thus far. Modern breast cancer

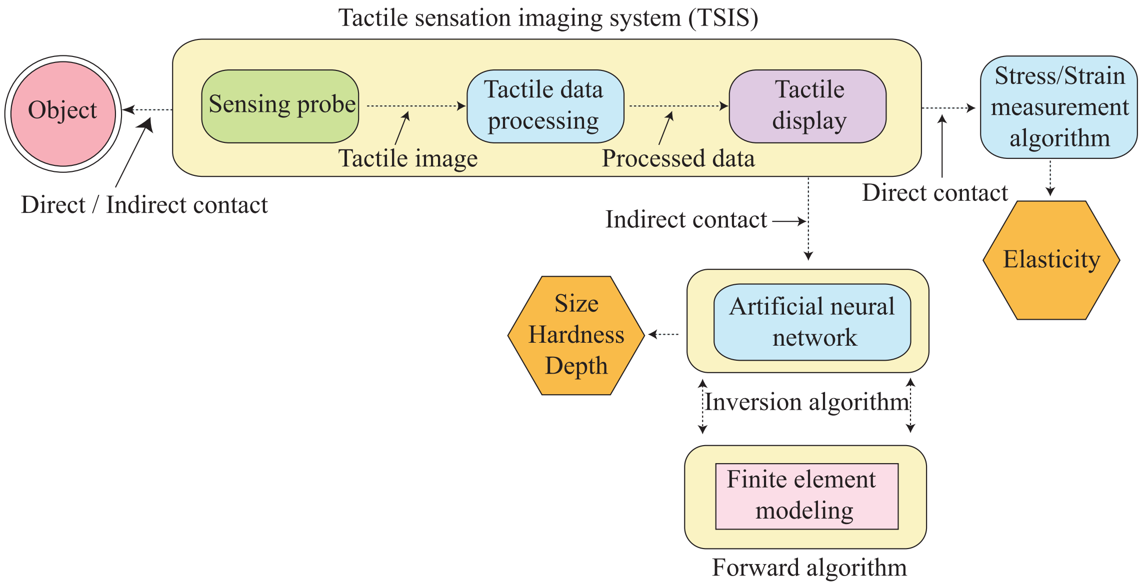

Figure 1.1: The graphical overview of the dissertation scope.

detection methods are also discussed in this chapter. Chapter 3 describes the tactile sensation imaging principle, which utilizes the TIR in the optical sensing probe. The analytic formulation, numerical simulation, and geometric optics approximation of the imaging principle are also provided.

Chapter 4 presents the hardware and software design descriptions of the TSIS. The description of each component for the TSIS hardware design is presented first, followed by the optical waveguide fabrication method and software design description.

In Chapter 5, the target stiffness estimation method via direct contact is outlined. To estimate the strain information of the contacted object, the non-rigid point matching algorithm called TPRL is developed and presented. Soft polymer experiments are presented, which validate the ability of the algorithm to measure the absolute elasticity.

If the object is embedded into the bulk medium such as tissue, the direct stiffness measurement method described in Chapter 5 is not accurate. Chapter 6 concerns the general case of estimating hardness as well as geometric properties, such as size and depth, of tissue inclusions. We provide relative and absolute inclusion parameter estimation methods. To estimate the absolute inclusion mechanical properties, the finite element modeling (FEM) based forward algorithm and artificial neural network (ANN) based inversion algorithm are provided. The results of those studies using realistic tissue phantoms are then presented and compared.

Chapter 7 provides a conclusion with a summary of the major results and a discussion of the future work.

CHAPTER 2
BACKGROUND AND LITERATURE REVIEW

In this chapter, we present a background and literature review of artificial tactile sensors. A review of the human tactile sensing mechanism is presented, followed by a review of various artificial tactile sensor designs, and elasticity determination systems. The application of modern breast tumor detection methods is also discussed.

2.1 Human Tactile Sensing Mechanism

The tactile sensation, also called touch sensation, is where external objects or forces are perceived through physical contact, mainly with the skin (Johnson and Hsiao, 1992). Whereas the other four senses - smell, taste, sight, and hearing - are located in specific areas of the body, human tactile sensors are located throughout the body (Uttal, 1973), (Jayawant, 1989). It is known that human tactile perception is largely dependent upon the properties of mechanoreceptors in the skin (Johannson and Vallbo, 1979). When a mechanoreceptor is stimulated, potential impulses are generated and transmitted along myelinated axons to the central nervous system (Kandel et al., 2000), (Pirznieks et al., 2001). There are several types of mechanoreceptors, and each generates a different type of stimulus. The existence of a variety of mechanoreceptor types provides additional evidence for the peripheral processing that occurs in human tactile sensing mechanism.

2.1.1 Tissue Structure

In terms of the human skin anatomy, the layers of human skin, epidermis, dermis, and subcutanea, have different mechanical properties and distinct physical properties. The outermost layer, the epidermis, is the stiffest layer (1.4×10^5 Pa) and is approximately 1 to 2 mm thick. The middle layer, the dermis, is softer than the epidermis (8.0×10^4 Pa) and is approximately

1 to 3 mm thick. The bottom layer, the subcutanea, is the softest layer (3.4×10^4 Pa) and is composed of fat. The thickness of the subcutanea layer is over 3 mm (Kandel et al., 2000). Due to the difference in hardness of each layer, when the pressure is applied to the tissue, the inner layers (dermis and subcutanea) deform more than the outermost layer (epidermis). Fig. 2.1 shows the structure of the skin and the locations of mechanoreceptors.

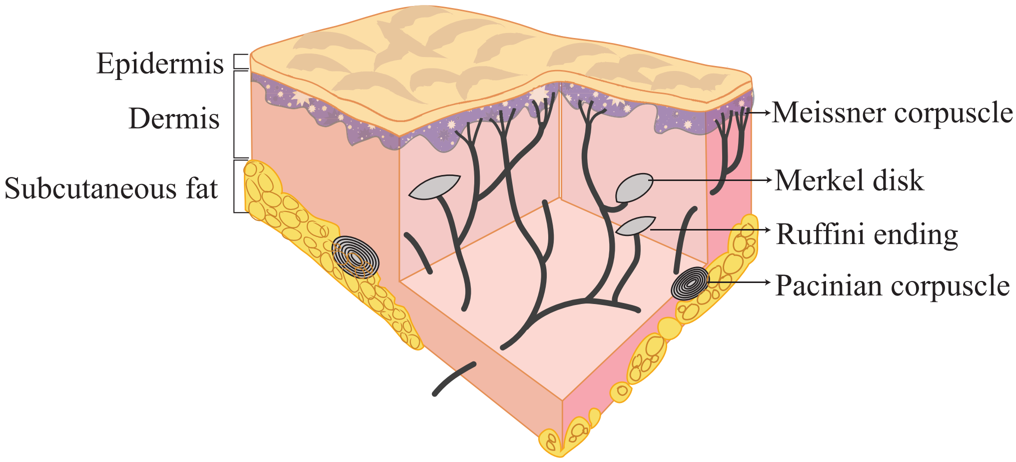

Figure 2.1: The structure of the skin and location of its primary mechanoreceptors.

2.1.2 Mechanoreceptor Functionality

The human mechanoreceptors are correlated with the four response characteristics. Thus mechanoreceptors can also be classified into four types based on functionality: Meissener's corpuscles, Merkel's disks, Pacinian corpuscles, and Ruffini endings (Uttal, 1973), (Kandel et al., 2000).

Meissener corpuscles are located in the boundary of the epidermis and dermis layers, and they are effective in detecting the surface roughness. They detect vibration of the skin and respond in a range of approximately 20 to 100 Hz. Merkel disks are composed of a group of spherical tactile cells, each in close association with a nerve terminal that is attached to a single myelinated axon. Among the four main types of mechanoreceptors, Merkel disks are the most sensitive to vibrations at low frequencies. The firing frequency of Merkel disks is 0 to 200 Hz. Pacinian corpuscles are located in the subcutaneous fat. They respond to deep-pressure touch, for which they have a wide receptive field. The response to vibrations occurs at relatively high frequencies of 100 to 300 Hz. Finally, Ruffini endings have a wide receptive field and are believed to detect pressure and elongation. It is also believed that they are useful for monitoring the slippage or the grip of objects.

2.2 Artificial Tactile Sensors

Many artificial tactile sensors have been developed over the past decade or so to mimic the tactile spatial resolution of the human finger (Schmidt et al., 2006). Artificial tactile sensors can be categorized using different sensing principles. Sensing mechanism, defined as the conversion of one form of energy into another, occurs when human mechanoreceptors receive stimuli and transduce physical energy into a nervous signal. Several types of artificial tactile sensors exist according to the different sensing mechanism available. In this section, some examples of artificial tactile sensors are presented.

2.2.1 Capacitive Sensors

The capacitive type of tactile sensor transforms the applied force into capacitance variation (Chu et al., 1996), (Leineweber et al., 2000), (Morimura et al., 2000). A single tactile sensor consists of three layers, while parallel-plate capacitors and dielectric materials fill the gaps between the plates. The dielectric layer is usually made up of air or silicone. If force is applied to one plate, the distance between the two plates decreases, resulting in increased capacitance (Webster, 1988), (Kolesar and Dyson, 1995). By measuring the increased capacitance, the tactile data can be perceived. The basic principle behind capacitive sensors is that they monitor changes in capacitance resulting from contact. The diagram of the capacitive sensor is shown in Fig. 2.2. Let A be the area of the plates and d be the distance between the top and bottom plates, and it is much smaller than the plate dimensions. Then the capacitance of the cell can be expressed by

$$C = \varepsilon_0 \varepsilon_r (A/d), \tag{2.1}$$

where $\varepsilon_0 = 8.85 \times 10^{-12} F \cdot m^{-1}$ is the permittivity and ε_r is the dielectric constant of the dielectric layer (Najarian et al., 2009).

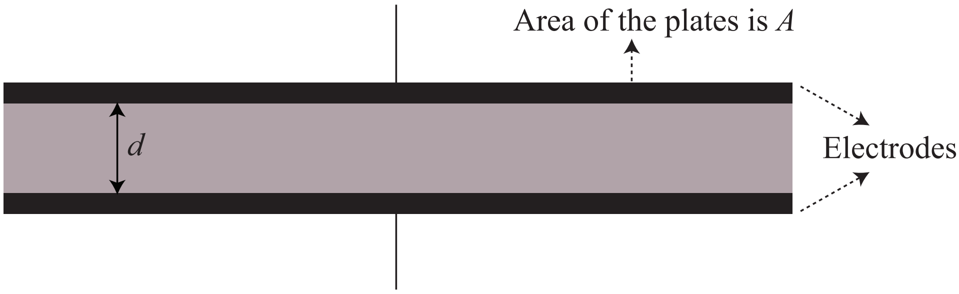

Figure 2.2: The schematic of capacitive sensor (Najarian et al., 2009).

The main advantage of capacitive sensors is their high density due to the small size of the sensor (Dargahi et al., 2000), (Lee and Nicholls, 1999). Some researchers have reported 8 $\times$ 8 capacitive sensor arrays within a 1 mm spatial resolution; this shows compatible spatial resolution of human mechanoreceptors (Kandel et al., 2000). The disadvantages of this type of sensor include significant hysteresis and temperature sensitivity (Dargahi et al., 2000).

2.2.2 Piezoresistive Sensors

The tactile sensing method for piezoresistive sensors is to monitor the resistance change in a conductive material under the applied force (Samaun et al., 1973). The resistance value is maximum when there is no force, and it decreases as the applied force increases. Fig. 2.3 shows the schematic of the cylinder-shaped piezoresistive sensor (Najarian et al., 2009). In Fig. 2.3, the silicone-rubber electrode is used for the piezo material. The advantages of these types of sensors are their high sensitivity, low cost, and wide dynamic range (Kolesar and Dyson, 1995). However, they can measure only a single touch, not a multi-touch at the same time. Also, they consume a great deal of power. Their limited tactile spatial resolution is another disadvantage (Schaffner et al., 1991).

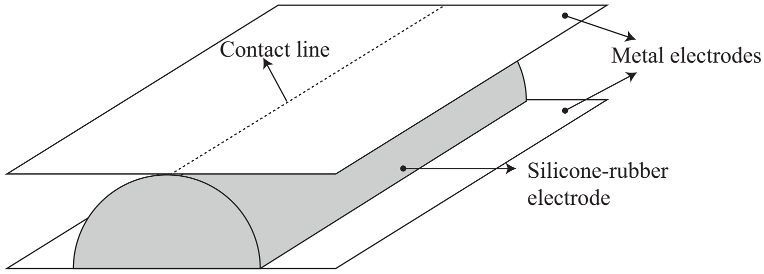

Figure 2.3: The schematic of piezoresistive sensor (Najarian et al., 2009).

2.2.3 Piezoelectric Sensors

The piezoelectric sensors use the piezoelectric effect, which is the voltage generation across a piezoelectric material when the force is applied (Rossi and Domenici, 1986). Fig. 2.4(a) and Fig. 2.4(b) show the general concept of the piezoelectric mechanism (Najarian et al., 2009). In a piezoelectric material, the dipoles are randomly spread without voltage. Once the electricity is applied, the dipoles are aligned along the direction of the applied electric field. Under this condition, when the sensors are pressed by an external force, the dipoles shift from the axis, causing the charges to become unbalanced and the voltage to be induced (Krishna and Rajanna, 2004). The applied force is measured by the generated voltage due to the imbalance in charge. Many tactile sensors have been developed based on the piezoelectric mechanism (Dargahi et al., 2000), (Najarian et al., 2006). These types of sensors have a wide dynamic range and durability. They are also simple, inexpensive, and easy to fabricate; however they are sensitive to temperature (Balsky et al., 1989). Furthermore, as with the piezoresistive tactile sensor, limited tactile spatial resolution and hysteresis are disadvantages (Krishna and Rajanna, 2004).

2.2.4 Magnetic-Based Sensors

Magnetic-based sensors measure the movement of a small magnet by an applied force generating flux density. This phenomenon is known as the Villari effect (Ong et al., 2009). The sensor uses magnetoelastic material, which deforms under force, causing changes in its magnetic characteristics (Hackwood et al., 1983). A micro-machined, magnetic-based sensor is introduced in (DiLella et al., 2000), demonstrating that the sensor is very small, sensitive, and requires little

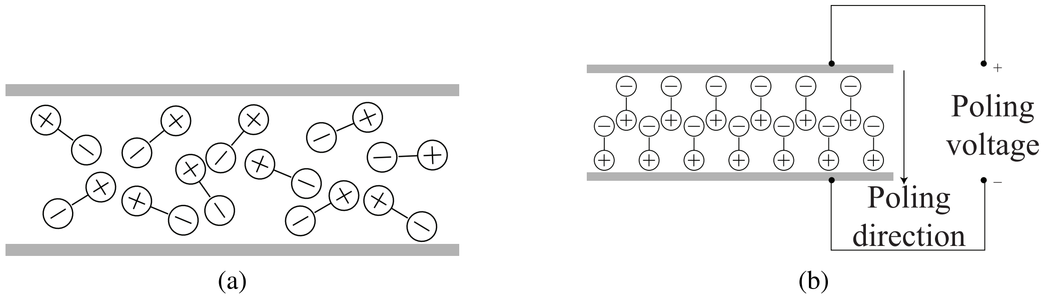

Figure 2.4: The schematic of piezoelectric sensor. (a) Randomly directed dipoles in ceramic structure (Najarian et al., 2009). (b) Alignment of dipoles in the direction of applied electric field (Najarian et al., 2009).

power consumption. The general advantages of the magnetic-based sensor include its good dynamic range, lack of mechanical hysteresis, high sensitivity, and linear response. However, this type of sensor can be used only in non-magnetic objects, which is a major drawback.

2.2.5 Optical Sensors

The optical sensor is also commonly used in artificial tactile sensors. This type of sensor uses the optical tactile sensing mechanism called "phenomenon of photoelasticity" (Katz, 2002). If pressure is applied to the photoelastic sensing probe of optical sensors while light is injected into it, light intensity changes, which can be measured. Various research groups have explored optical sensors for tactile sensing, primarily because these sensors are immune to elastomagnetic noise, and have the ability to process tactile data using a charged-coupled device (CCD) without complex wiring (Kamiyama et al., 2003). In (Ohka et al., 2004), optical sensors are developed using an elastic sheet and a transparent board parallel to the sheet. The applied force makes the protrusion contact of the sheet, and the amount of force is measured by the contact area. The optical sensor that uses markers inside an elastic body and a fiber scope is introduced in (Ferrier and Brockett, 2000). The sensor is formed as a miniaturized fingertip shape, which measures a relatively small amount of force. An optical-based three axial tactile sensor capable of measuring the normal and shear forces is also reported in (Heo et al., 2006), (Ohmura et al., 2006), (Cheung and Lumelsky, 1992), (Koh et al., 2006). The general advantages of this type of sensor include its high resolution, flexibility, sensitivity, and electromagnetic interference immunity, whereas common disadvantages are loss of light by chirping and bending, difficulty in calibration, as well as bulkiness (Cheung and Lumelsky, 1992), (Begej, 1988).

2.3 Elasticity Determination System

Tissue stiffness or elasticity is an indicator of tissue health, with increased tissue stiffness pointing to an increased risk of cancer. Over the past two decades, various methods have been devised for measuring or estimating soft tissue stiffness (Gao et al., 1996), (Garra et al., 1997). Generally, this is called "elasticity determination system." In this section, we review the current elasticity determination system.

2.3.1 Elastography

Elastography is a non-invasive method in which tissue elasticity is used to detect or classify tumors (Ophir et al., 1991). When a compression or vibration is applied to the tissue, the included tumor deforms less than the surrounding tissue. Under this observation, elastography records the distribution of tissue elasticity (Rogowska et al., 2004). Elastography has been successfully applied to tumor characterization to improve diagnostic accuracy and surgical guidance. It is currently performed using ultrasonic, magnetic resonance (MR), and atomic force microscopy (AFM).

Ultrasonic elastography is the most intensely investigated area of elastography (Vinckier and Semenza, 1998). There are three types of ultrasonic elastography: compressive elastography, transient elastography, and sonoelastography. In compressive elastography, controlled compression of the transducer probe is loaded to the tissue, and signals of pre- and post-compression are compared to calculate the tissue stiffness distribution map (Rivaz et al., 2008). The compression is applied by the operator or the external compressor attached in the transducer probe. Transient elastography uses a transient vibration, produced by the transient probe, that generates under low frequency to create tissue deformation. The transient probe consists of a transducer probe which is located at the end of a vibrating piston. The piston produces a vibration of low amplitude and frequency, which generates a shear wave that passes through the tissue. The quantity of tissue deformation is then detected by pulse-echo ultrasound. Sonoelastography uses a real-time ultrasound Doppler technique to record the propagation pattern through the tissue with low-frequency shear waves. The linear array broad-band transducer probe with a frequency range of 6 to 14 MHz is used to produce the low-frequency shear waves.

Ultrasonic elastography in three different groups is carried out with the same equipment except the transducer probe. The embedded software module with an algorithm is also different to process different techniques. Ultrasonic elastography is relatively well-developed method that is being used in a wide range of medical applications (Stravros et al., 2011), (Bhatia et al., 2010). However, compared to the TSIS that we propose in this dissertation, ultrasonic elastography is computationally expensive, making it challenging to display data in real time (Hoyt et al., 2006). Other disadvantage is that the ultrasonic elastography is very expensive (over $150K for eSie Touch Elasticity Imaging System, ACUSON S2000). The size of ACUSON S2000 system is approximately 51.2 inch (height), 24.5 inch (width), and 43.4 inch (depth). The weight of the system is 365 pounds. The ultrasonic elastography has 86.5% sensitivity, 89.8% specificity, and 88.3% accuracy (Itoh et al., 2006). Fig. 2.5(a) shows the conventional ultrasonic elastography modality and Fig. 2.5(b) shows the breast elastogram.

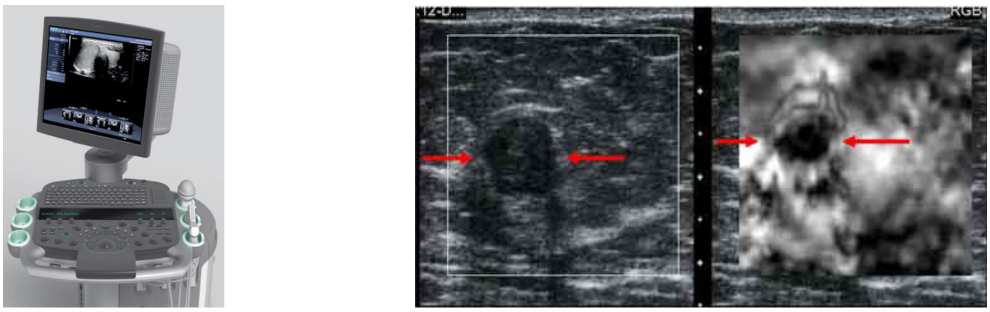

(a) (b)

Figure 2.5: The ultrasonic elastography system and its image sample. (a) The conventional ultrasonic elastography modality (Siemens, 2011), (b) The breast elastogram (Siemens, 2011).

MR elastography is another elastography technique capable of measuring tissue stiffness. It provides a tissue stiffness map using propagating cyclic waves in the tissue. External vibrations are applied into the tissue in order to generate propagating waves within the tissue. The external vibrations are matched with motion encoding gradients (MEG) in the image sequence, which extracts the motion in the phase of MR images. These images are then processed to generate the final tissue stiffness map. Although MR elastography is successfully tested to static organs such as breast, brain, and liver, the modality is still expensive and it is cumbersome to use in the small size of clinic room (Insana et al., 2004).

AFM is a very high resolution scanning probe microscopy, with the order of fractions of a nanometer resolution (Giessibi, 2003). AFM elastography combines indentation and imaging modalities to map the spatial distribution of cell mechanical properties such as stiffness, non-linearity, anisotropy, and heterogeneity. Despite its high-resolution imaging capability, AFM elastography is suitable only for local area measurements and is not suitable to the large tissue area such as breast (Giessibi, 2003).

2.3.2 Elasticity Imaging Using Tactile Sensors

Recently, a new technological method entitled "elasticity imaging using tactile sensor" has been explored (Dargahi and Najarian, 2004), (Eltaib and Hewit, 2003). This type of technology calculates and visualizes tissue elasticity by sensing mechanical stresses on the surface of tissues using tactile sensors. Elasticity imaging using tactile sensors is also called mechanical imaging, tactile imaging, elastic modulus imaging, or biomechanical imaging (Dargahi and Najarian, 2004), (Eltaib and Hewit, 2003), (Wang et al., 2009), (Yates et al., 2005).

The medical device named "SureTouch Visual Mapping System" produced by Medical Tactile Inc. is an elasticity imaging system using capacitive tactile sensors (Egorov and Savazyan, 2008). The device consists of a probe with capacitive pressure sensor arrays and electronic units to transmit tactile data to the computer. Using a 32×32 capacitive tactile sensor array, the device obtains the stress distribution on the tissue surface (Wellman et al., 2001a), (Weber, 2000), (Galea, 2004). The device is capable of computing and visualizing the pressure pattern of the tissue. One of its advantages is that it is small and portable, thus it is easy to use. Also it utilizes no ionizing radiation and magnetic fields, unlike CT or MRI. A disadvantages is that the tactile spatial resolution of the device is not as good as the optically based tactile sensing method. Thus, obtaining precise tissue stiffness map through this device is difficult. It also requirs extensive calibration. In addition, the device is expensive because it requires extra sensors to detect the applied force.

To estimate tissue inclusion parameters using tactile data obtained from capacitive tactile sensors, different approaches have been explored. In (Wellman et al., 2001a), the FEM based forward algorithm and Gaussian fitting model-based inversion algorithm are devised. This work was extended in (Weber, 2000) to attempt to find a more complete set of tissue inclusions. They showed that the estimation results are more accurate in determining the size of a tissue inclusion than manual palpation. Nevertheless, the results are limited to tissue inclusions at least 100 times stiffer than the surrounding tissues. In addition, other tissue inclusion parameters such as depth and hardness are not available. In (Galea, 2004), the FEM based forward algorithm and transformation matrix based inversion algorithm are proposed to estimate size, depth, and hardness of the tissue inclusion. However, the relative error in estimating the tissue inclusion modulus was still large (over 90%). Fig. 2.6 shows the SureTouch Visual Mapping System using capacitive tactile sensors (MedicalTactile, 2011).

Figure 2.6: The SureTouch Visual Mapping System of Medical Tactile Inc (MedicalTactile, 2011).

Another type of elasticity imaging system using tactile sensors is the "piezoelectric finger (PEF)" (Yegingil et al., 2007). In this work, the micro-machined artificial finger using a piezoelectric tactile sensing mechanism is introduced. The PEF is a type of cantilever system. For driving, a top layer consists of piezoelectric zirconate titanate (PZT); for sensing, a bottom layer consists of PZT (Yegingil et al., 2010). In the initial condition, an electric field is induced to the top layer for driving, causing the PEF to bend. Under this condition, if an external force is applied to the sensing layer, the sensing layer bends more and the voltage is induced across it.

By measuring this voltage, the PEF measures the elasticity of the target. The PEF has several advantages, such as low cost, small form factor, and large dynamic range. However, it is sensitive to temperature variation and, thus requires somewhat extensive calibration. Furthermore, limited spatial resolution and hysteresis are disadvantages. Fig. 2.7 shows the PEF using PZT.

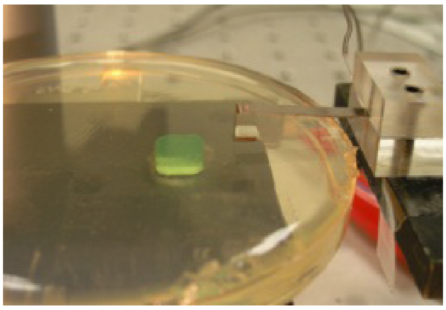

Figure 2.7: The piezoelectric finger using piezoelectric zirconate titanate (PZT) (Yegingil et al., 2010).

The elasticity imaging system using a piezoelectric polyvinylidene fluoride (PVDF) tactile sensor is also investigated in (Dargahi et al., 2007). The PVDF sensor structure consists of three layers. The top layer is a tooth-like protrusion using a silicon wafer. The middle layer is a patterned PVDF film and works as a transducer. These two layers are sustained by a plexiglas bottom layer. Although PVDF is capable of measuring tissue property such as hardness, the calculation of other important parameters such as size, depth, and shape is still unavailable. To estimate tissue inclusion parameters using PVDF, the FEM based forward algorithm and ANN based inversion algorithm are investigated in (Dargahi et al., 2007). For the ANN training algorithm, they used the resilient back-propagation algorithm. In their work, a small number of forward algorithm data used to train an inversion algorithm also makes the parameter estimation results less accurate. Also, the calculation of inclusion parameters such as size, depth, and shape is still not available. In addition, the performance of the proposed method was validated using only simulated data without phantom experimental data or clinical data.

The piezoresistive tactile sensor for tissue elasticity measurement is also investigated in (Heever et al., 2009). In their work, an array of force sensing resistors (FSRs) is integrated into the polymer sheet to get a tactile distribution of a target. The obtained low resolution tactile image is improved by the super-resolution image processing algorithm. The study shows that the elasticity imaging system using FSRs has the capability to distinguish between a hard and soft object. However, the absolute tissue inclusion parameter estimation is still impossible through this device and algorithms.

2.4 Application of Breast Tumor Detection

The TSIS, proposed in this dissertation, will be applicable to various areas. The one applicable area is early breast tumor monitoring and warning. In this dissertation, we focus our attention on the human breast; however, the technology can be applicable to other soft tissues throughout the body.

According to the American Cancer Society, more than 178,000 women and 2,000 men in the U.S. are found to be afflicted with breast cancer every year; international statistics report an estimated 1,152,161 new cases annually (Jemal et al., 2009), (Kamangar et al., 2006). In 2009, approximately 40,610 people were dying of breast cancer in the United States (Jemal et al., 2009). This form of the disease is the leading killer of females aged between 40 and 55 years and is statistically the second cause of death overall in women. The current approach to this disease involves early detection and treatment. This approach yields a 98% survival rate of those women who are diagnosed at the early stages of the disease (stages 0 - I); whereas for those where the cancer has progressed to stage III, the survival rate for 10 years is 65% (Ratanachaikanont, 2005b).

Clearly, early detection and diagnosis is the key to surviving this fatal illness (Karahaliou et al., 2008). There are many methods used today to detect various forms of breast tumor. The criteria for breast tumor detection modalities include high sensitivity, acceptable specificity, accuracy, ease of use, acceptability in terms of levels of discomfort and time taken to perform the test, and cost effectiveness. This section reviews the modern breast tumor detection techniques.

Breast Self-Examination

The breast self-examination (BSE) is still recommended for the early detection of tumors, and a clinical breast examination (CBE) performed by a medical specialist has a sensitivity of over 57.14% and a specificity of 97.11% (Ratanachaikanont, 2005b). Another study shows that a sensitivity of CBE is approximately 59% and a specificity of CBE is approximately 93% (Bobo et al., 2000). Figs. 2.8(a) and 2.8(b) shows how we palpate the breast manually. In the pattern of search, a vertical strip pattern is used to search the full extent of breast tissue. In the palpation, the middle three fingers are used to palpate a breast at a time to detect stiffness beneath the breast surface.

(a)

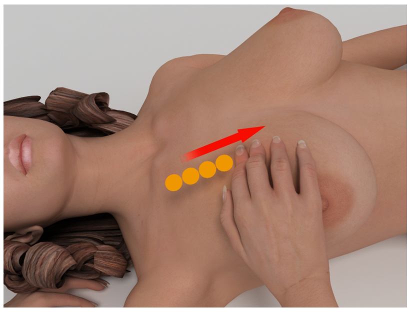

(b)

Figure 2.8: The example of the breast self-examination. (a) The pattern of search, (b) The palpation method.

Although these methods cannot determine the degree of malignancy, they do detect lesions that require further testing. In comparison with patients who have not been screened, patients who are screened with CBE and BSE received twice as many biopsies (Ratanachaikanont, 2005b). However, there are several drawbacks to these methods. The main drawbacks of CBE and BSE are that the physicians record the verbal description of their palpable finding along with a hand drawing of target mass. Thus the examination is subjective and the performance is highly dependent upon the healthcare provider.

Mammography

One breast tumor imaging technique that has been in use for the past 30 years and is still widely used today is the mammography (Olsen and Gotzsche, 2001), (Gotzsche and Olsen, 2000). This method of breast tumor detection is widely acclaimed as the best available at present (Mushlin et al., 1998). It uses X-rays to photograph the breast while it is compressed, giving 83% to 95% true-positive results and 0.9% to 6.5% false-positive results. The main disadvantage of mammography is that it uses harmful radiation. Also, the results are skewed at times by the density of the breast tissue, body mass index, age, and even genetic issues. Mammography has to be performed by a specially trained mammography technician on a dedicated machine, using radiographic film that requires chemicals to develop the picture; after this point, a radiologist is required to diagnose the results. Fig. 2.9(a) shows the conventional mammogram modality and Fig. 2.9(b) shows the example of the breast mammography.

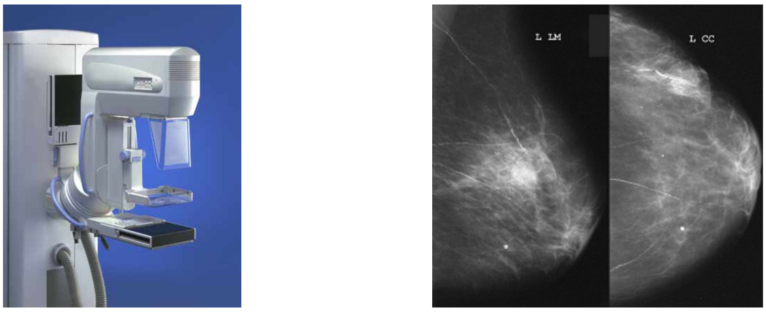

(a) (b)

Figure 2.9: The mammography modality and its image sample. (a) The conventional mammogram modality (Mommography, 2011), (b) The breast mammography (Mommography, 2011).

Ultrasound Imaging

Ultrasound, also known as sonomammography, is a method used to create an image of palpable breast masses using sound waves (Sehgal et al., 2006), (Rahbar et al., 1999). This method is non-invasive and is performed by a technician who rotates a handheld transducer on the breast surface to form an image of what is directly below the transducer (Huber et al., 2002). Ultrasound is most commonly used on pregnant women who cannot be subjected to X-rays, as X-rays may harm the fetus. The downside of this method is that each individual image has to be labeled by the technician performing the test to create a map of each breast. Interference, such as specks, often shows up to blur the image, and the lateral margins of lesions are not easy to detect. Furthermore, in general, ultrasound suffers from low contrast. Fig. 2.10(a) shows the conventional ultrasound modality and Fig. 2.10(b) shows the example of the breast ultrasound image.

(a) (b)

Figure 2.10: The ultrasound imaging modality and its image sample. (a) The conventional ultrasound modality (Ultrasound, 2011), (b) The breast ultrasound image (Ultrasound, 2011).

Magnetic Resonance Imaging

Another non-invasive breast tumor detection method is magnetic resonance imaging (MRI), which generates either 2-D or 3-D images of the breast, and has been in use since 1977 (Orel and Schnall, 2001). The advantages of MRI over other methods of early breast cancer detection are: 1) it does not use radiation; 2) it forms images from multiple angles and is able to capture the difference between soft and hard tissues; and 3) the image has high resolution and contrast (Orel and Schnall, 2001). MRI uses radio waves and a magnetic field in order to change the alignment of hydrogen nuclei which, in turn, create the image. The process of capturing an MRI image is complicated because fat in the breast has to be suppressed. In order to get around this problem, contrasting dyes or agents, which are usually gadolinium-based, are used to distinguish the different tissues in the image. The major drawback of the MRI is that it is expensive due to the combination of the cost of the actual machine, the cost of running it, and the expenses incurred in having a trained professional to operate it and a specialist radiologist to interpret the images. In addition, MRI has relatively low specificity. Fig. 2.11(a) shows the conventional MRI modality and Fig. 2.11(b) shows the example of the breast MRI image.

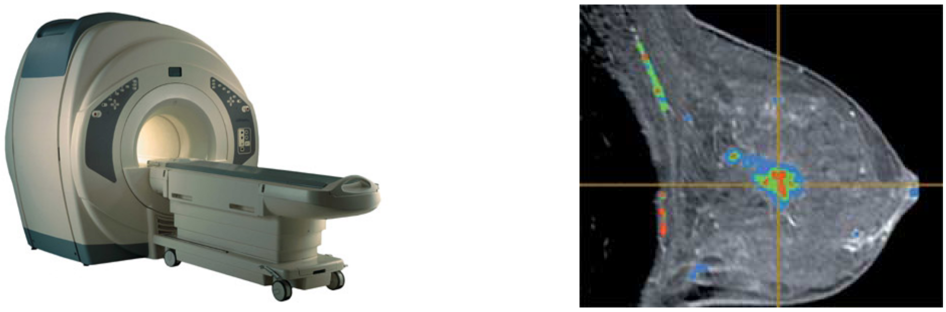

(a) (b)

Figure 2.11: The magnetic resonance imaging modality and its image sample. (a) The conventional magnetic resonance imaging modality (MRI, 2011), (b) The breast magnetic resonance image (MRI, 2011).

Thermography Imaging

The thermography imaging method measures the temperature potential across breasts through an infrared scan (Gautherie and Gros, 1980). Because malignant tumors are fed through neoangiogenesis as well as existing blood vessels, blood circulation is higher and so is the temperature of the suspicious region. The thermograph performs best when the patient's body temperature is most stable. Dense breast tissue increases specificity in thermography, and larger tumors are easier to detect as well. The disadvantage of the thermograph is that it is highly affected by procedural effects, such as how cool the breast is and how the breast is positioned. Large breasts and surrounding areas receive poor imaging, and uneven body temperature distribution usually results in false-positives or false-negatives. Fig. 2.12(a) shows the conventional thermography imaging modality and Fig. 2.11(b) shows the example of the breast thermography image.

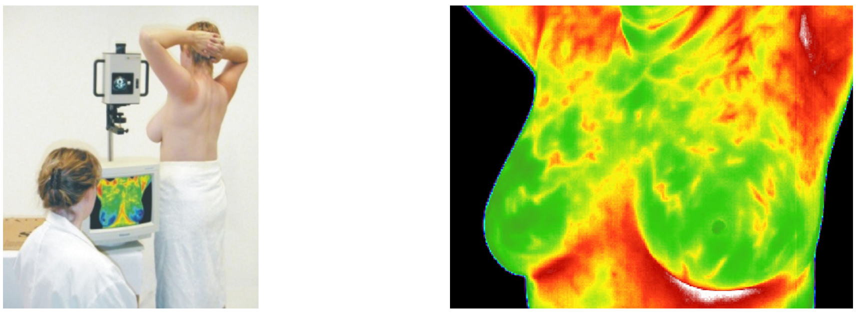

(a) (b)

Figure 2.12: The thermography imaging modality and its image sample. (a) The conventional thermography imaging modality (Thermography, 2011), (b) The breast thermography image (Thermography, 2011).

Sensitivity and Specificity

Sensitivity and specificity are good measures for the performance evaluation of each breast tumor detection modality. In statistics, sensitivity means the performance measures of the actual positives which are correctly identified, and specificity means the performance measures of the actual negatives (Altman and Bland, 1994). Imagine a scenario where people are tested for a tumor. The test outcome can be positive (tumor) or negative (healthy), whereas the actual health status of the people may be different. The true-positive, T_p, false-positive, F_p, true-negative, T_n, and false-negative, F_n, can be defined as below (Rangayan, 2005).

1) True-positive, T_p: Tumor patient correctly diagnosed as tumor.
2) False-positive, F_p: Healthy people incorrectly identified as tumor.
3) True-negative, T_n: Healthy people correctly identified as healthy.
4) False-negative, F_n: Tumor patient incorrectly identified as healthy.

Then the sensitivity and the specificity can be calculated as follows.

$$\text{Sensitivity} = \frac{\text{Number of true positive, } T_p}{\text{Number of subjects with the tumor}}, \tag{2.2}$$

$$\text{Specificity} = \frac{\text{Number of true negative, } T_n}{\text{Number of subjects without the tumor}}. \tag{2.3}$$

Table 2.1 shows the literature survey of sensitivity and specificity of various breast tumor detection modalities.

Table 2.1: The sensitivity and specificity of breast tumor detection modality.

	Sensitivity	Specificity
Clinical breast examination (Ratanachaikanont, 2005b)	57.14%	97.11%
Mammography (Carney et al., 2003)	68.6%	91.4%
Doppler ultrasound (Raza and Baum, 1997)	68.1%	95.1%
Magnetic resonance imaging (Bluemke et al., 2004)	88.2%	67.7%
Positron emission tomography (Lind et al., 2004)	96.4%	77.3%
Thermography imaging (Parisky et al., 2003)	97.3%	14.1%

CHAPTER 3

TACTILE SENSATION IMAGING PRINCIPLE AND NUMERICAL SIMULATIONS

During the past decades, many artificial tactile sensors have been proposed. Some have provided good tactile spatial resolution using MEMS technology. However, in comparison to human fingertips, with millions of mechanoreceptors per square inch of skin, most artificial tactile sensors still lack tactile spatial resolution. In this chapter, we present a new artificial tactile traction mechanism using the TIR principle to achieve the high spatial resolution.

3.1 Total Internal Reflection

The proposed tactile sensation imaging is based on the TIR principle. According to Snell's law, if two mediums have different refraction indices, and the light is shone throughout those two mediums, then a fraction of light is transmitted and the rest is reflected (Keiser, 1999). This is TIR. The angle above which the light is completely reflected is the critical angle. Figs. 3.1(a) to 3.1(c) explain the TIR phenomenon. In Fig. 3.1(a), the incidence angle is smaller than the critical angle. Thus, the light is transmitted to the other medium. In Fig. 3.1(b), the angle of incidence is equal to the critical angle. The critical angle is the minimum angle for the TIR. In Fig. 3.1(c), the incidence angle is larger than the critical angle, and TIR occurs.

In the TSIS design, the optical waveguide sensing probe is surrounded by air, having a lower refractive index than any of the layers in the waveguide, and the incident light directed into the waveguide can be trapped inside the waveguide. The basic principle of TSIS lies in the monitoring of the reflected light caused by changing of the critical angle by the contacted object. Figs. 3.2(a) and 3.2(b) illustrate the conceptual diagram of the imaging principle.

In the next section, we analyze the light propagation pattern in the optical waveguide using the wave optics analysis method. From this analysis, we show that TIR can be achieved in

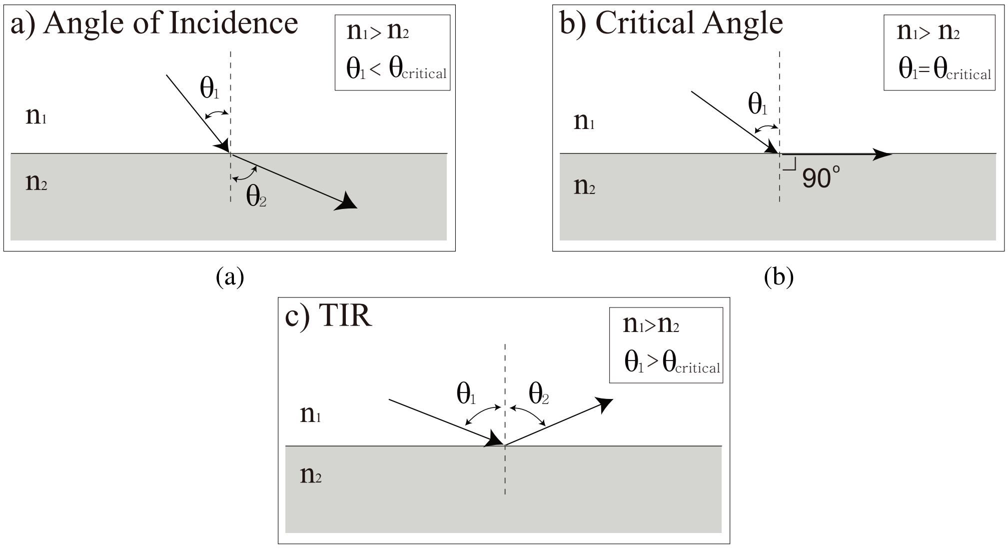

(a) (b) (c)

Figure 3.1: The Snell's law description. (a) The incidence angle is smaller than the critical angle. (b) The angle of incidence is equal to the critical angle. (c) The angle of incidence is bigger than the critical angle.

the multi-layered optical waveguide and the light is scattered out the waveguide if the force is applied to the waveguide. Second, we consider the geometric optics approximation to calculate the acceptance angle of light for the TIR in the waveguide. The obtained acceptance angle is finally used for the position of the light source in the TSIS design.

3.2 Analytical Solution: Wave Optics

In this section, we investigate the TSIS principle using the wave optics analysis method. The optical analysis for the one-layer waveguide case is done by the optical communications area (Katz, 2002). In this section, we extend the one-layer waveguide case into the four-layer waveguide case. Fig. 3.3 represents an optical waveguide consisting of three PDMS layers with one glass plate layer on top.

The refractive indices n_0 and n_5 are the refractive indices of the medium surrounding the waveguide; in this case it is the air. The refractive index of air is n_0 = n_5 = 1. The waveguide layers are positioned in the order of increasing refractive index, $n_1 > n_2 > n_3 > n_4 > n_0 = n_5$. Light propagates in z-direction, and the layers are positioned in x-direction. We assume an infinite length in planar y-direction.

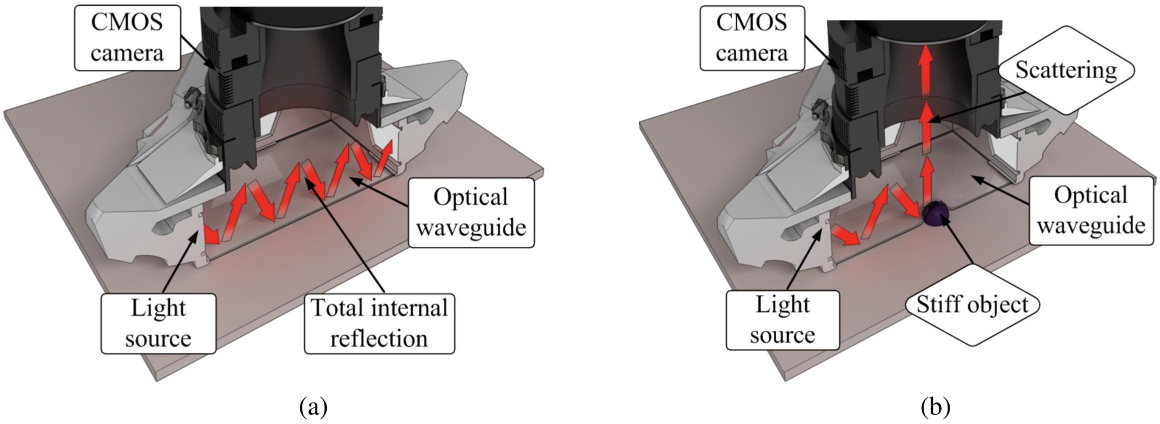

Figure 3.2: The schematic diagram of the tactile sensation imaging principle. (a) The light is injected into the waveguide to totally reflect. (b) The light scatters as the waveguide deforms due to the external force presented by a stiff object.

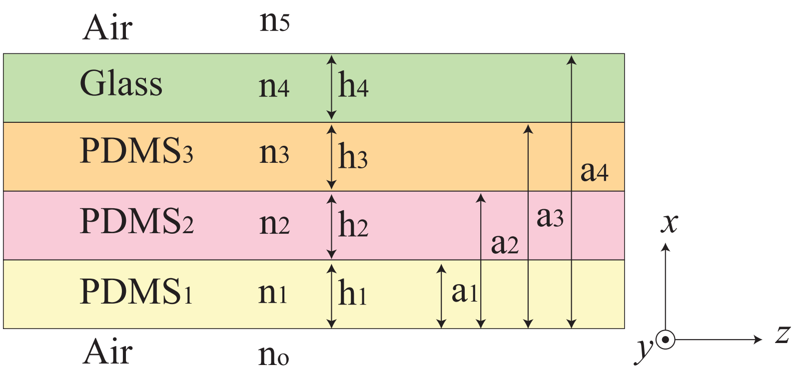

Figure 3.3: The schematic diagram of the multi-layered optical waveguide. The waveguide consists of three different densities of polydimethylsiloxane (PDMS) layers and one glass plate layer. The waveguide is surrounded by air.

1) Layer 1: PDMS, refractive index n_1 and height h_1,

2) Layer 2: PDMS, refractive index n_2 and height h_2,

3) Layer 3: PDMS, refractive index n_3 and height h_3,

4) Layer 4: Borosilicate glass plate, refractive index n_4 and height h_4.

Let us begin with the Maxwell wave equation describing light propagation in an optical waveguide (Saleh and Teich, 1991).

$$\nabla^2 \mathbf{E}(x, y, z, t) - [n^2/c^2]\partial^2 \mathbf{E}(x, y, z, t)/\partial t^2 = 0. \tag{3.1}$$

Here $\mathbf{E}(x, y, z, t)$ is the electric field, n is the refractive index, and c is the speed of light in vacuum. A similar equation is valid for the magnetic field $\mathbf{H}(x, y, z, t)$:

$$\nabla^2\mathbf{H}(x, y, z, t) - [n^2/c^2]\partial^2\mathbf{H}(x, y, z, t)/\partial t^2 = 0. \tag{3.2}$$

Since the components of electric and magnetic fields can be generally determined from one another, we will only focus on the electric field. For monochromatic waves with frequency ω, the solution of Eq. (3.1) has the following form.

$$\mathbf{E}(x, y, z, t) = \mathbf{E}(x, y, z)\exp(i\omega t). \tag{3.3}$$

Using form given in Eq. (3.3) into Eq. (3.1), the spatial distribution of electric field $\mathbf{E}(x, y, z)$ follows below form (Boyd, 2008).

$$\frac{\partial^2\mathbf{E}(x, y, z)}{\partial x^2} + \frac{\partial^2\mathbf{E}(x, y, z)}{\partial y^2} + \frac{\partial^2\mathbf{E}(x, y, z)}{\partial z^2} + k_0^2 n^2\mathbf{E}(x, y, z) = 0, \tag{3.4}$$

where k_0 is the wave vector in vacuum: $k_0 = \omega/c$. Since the waveguide is uniform in z-direction, we can look for only planar wave solutions.

$$\mathbf{E}(x, y, z) = \mathbf{E}(x, y)\exp(-i\beta z), \tag{3.5}$$

where β is the propagation constant. Since we are only looking for plane wave solutions, which are independent of y-direction, the field distribution varies only across x-direction. Given that form, the spatial distribution of electric field

$$\mathbf{E}(x, y) = \mathbf{E}(x). \tag{3.6}$$

Further, let us first consider the solution for the transverse y-component of the electric field. For that purpose, let us assume

$$\mathbf{E}(x) = e(x)\mathbf{j}, \tag{3.7}$$

where $\mathbf{j}$ is the unit vector along the y-direction. By substituting Eq. (3.5) into Eq. (3.4) we can reduce it to the following ordinary differential equation.

$$d^2e(x)/dx^2 + [k_0^2 n^2 - \beta^2]e(x) = 0. \tag{3.8}$$

This equation has to hold throughout all regions including the waveguide and the air.

$$d^2e(x)/dx + [k_0^2 n_0^2 - \beta^2]e(x) = 0, \qquad \text{Region 0: } x < 0 \tag{3.9}$$

$$d^2e(x)/dx + [k_0^2 n_1^2 - \beta^2]e(x) = 0, \qquad \text{Region 1: } 0 < x < a_1 \tag{3.10}$$

$$d^2e(x)/dx + [k_0^2 n_2^2 - \beta^2]e(x) = 0, \qquad \text{Region 2: } a_1 < x < a_2 \tag{3.11}$$

$$d^2e(x)/dx + [k_0^2 n_3^2 - \beta^2]e(x) = 0, \qquad \text{Region 3: } a_2 < x < a_3 \tag{3.12}$$

$$d^2e(x)/dx + [k_0^2 n_4^2 - \beta^2]e(x) = 0, \qquad \text{Region 4: } a_3 < x < a_4 \tag{3.13}$$

$$d^2e(x)/dx + [k_0^2 n_5^2 - \beta^2]e(x) = 0. \qquad \text{Region 5: } x > a_4 \tag{3.14}$$

Here regions 0 and 5 are outside the waveguide, and regions 1 to 4 are inside each respective waveguide layer. Since no light propagates outside the waveguide, the assumed solution in region 0 and 5 must decay exponentially with the distance from the surface. In the meantime, the propagating lights in region 1, 2, 3, 4 are oscillating and have sinusoidal form. Thus we assume that the solution form of Eqs. (3.9) to (3.14) as below.

$$e(x) = e_0 \exp[\kappa_0 x], \qquad \text{Region 0: } x < 0 \tag{3.15}$$

$$e(x) = e_1 \cos[\kappa_1 x + \varphi_1], \qquad \text{Region 1: } 0 < x < a_1 \tag{3.16}$$

$$e(x) = e_2 \cos[\kappa_2 x + \varphi_2], \qquad \text{Region 2: } a_1 < x < a_2 \tag{3.17}$$

$$e(x) = e_3 \cos[\kappa_3 x + \varphi_3], \qquad \text{Region 3: } a_2 < x < a_3 \tag{3.18}$$

$$e(x) = e_4 \cos[\kappa_4 x + \varphi_4], \qquad \text{Region 4: } a_3 < x < a_4 \tag{3.19}$$

$$e(x) = e_5 \exp[\kappa_5 (a_4 - x)]. \qquad \text{Region 5: } x > a_4 \tag{3.20}$$

The solutions are determined with unknown parameters such as amplitudes e_i, transverse wave vectors κ_i, and phases φ_i, i = 0, 1, 2, 3, 4, 5. These parameters will have to be determined from the boundary conditions, matching the fields in different regions. Substituting these pieces of the solution in Eqs. (3.15) to (3.20) into their respective equation in Eqs. (3.9) to (3.14), we obtain the following dispersion relations:

$$-\kappa_0^2 + \beta^2 = k_0^2 n_0^2, \qquad \text{Region 0: } x < 0 \tag{3.21}$$

$$\kappa_1^2 + \beta^2 = k_0^2 n_1^2, \qquad \text{Region 1: } 0 < x < a_1 \tag{3.22}$$

$$\kappa_2^2 + \beta^2 = k_0^2 n_2^2, \qquad \text{Region 2: } a_1 < x < a_2 \tag{3.23}$$

$$\kappa_3^2 + \beta^2 = k_0^2 n_3^2, \qquad \text{Region 3: } a_2 < x < a_3 \tag{3.24}$$

$$\kappa_4^2 + \beta^2 = k_0^2 n_4^2, \qquad \text{Region 4: } a_3 < x < a_4 \tag{3.25}$$

$$-\kappa_5^2 + \beta^2 = k_0^2 n_5^2. \qquad \text{Region 5: } x > a_4 \tag{3.26}$$

Further, we need to apply the boundary conditions and match the field components. For that purpose, we need to first determine the magnetic field. It has a similar form to the electric field, but now has only one nonzero component along the z-direction.

$$\mathbf{H}(x, y, z) = \mathbf{k}h(x)\exp(-i\beta z + i\omega t), \tag{3.27}$$

where $\mathbf{k}$ is the unit vector along z-direction. Substituting Eqs. (3.5) and (3.27) into the following Maxwell equation,

$$\nabla \times \mathbf{E} = -(1/c)\partial \mathbf{H}/\partial t, \tag{3.28}$$

where c is the speed of light in vacuum. Then we can obtain the following general solution for the magnetic field, expressed through the same parameters, as the electric field:

$$h(x) = -(ic/\omega)\kappa_0 e_0 \exp[\kappa_0 x], \qquad \text{Region 0: } x < 0 \tag{3.29}$$

$$h(x) = (ic/\omega)\kappa_1 e_1 \sin[\kappa_1 x + \varphi_1], \qquad \text{Region 1: } 0 < x < a_1 \tag{3.30}$$

$$h(x) = (ic/\omega)\kappa_2 e_2 \sin[\kappa_2 x + \varphi_2], \qquad \text{Region 2: } a_1 < x < a_2 \tag{3.31}$$

$$h(x) = (ic/\omega)\kappa_3 e_3 \sin[\kappa_3 x + \varphi_3], \qquad \text{Region 3: } a_2 < x < a_3 \tag{3.32}$$

$$h(x) = (ic/\omega)\kappa_4 e_4 \sin[\kappa_4 x + \varphi_4], \qquad \text{Region 4: } a_3 < x < a_4 \tag{3.33}$$

$$h(x) = (ic/\omega)\kappa_5 e_5 \exp[\kappa_5(a_4 - x)]. \qquad \text{Region 5: } x > a_4 \tag{3.34}$$

The ratio between the field amplitude of the electric and magnetic fields, $h(x)/e(x)$, is called impedance. The impedance $h(x)/e(x)$ has to stay continuous on all boundaries at $x = 0$,

$x = a_1$, $x = a_2$, $x = a_3$, $x = a_4$ as below.

$$-(ic/\omega)\kappa_0 e_0 \exp[\kappa_0 x]/e_0 \exp[\kappa_0 x]$$
$$= (ic/\omega)\kappa_1 e_1 \sin[\kappa_1 x + \varphi_1]/e_1 \cos[\kappa_1 x + \varphi_1], \text{Boundary 1: } x = 0 \quad (3.35)$$
$$(ic/\omega)\kappa_1 e_1 \sin[\kappa_1 x + \varphi_1]/e_1 \cos[\kappa_1 x + \varphi_1]$$
$$= (ic/\omega)\kappa_2 e_2 \sin[\kappa_2 x + \varphi_2]/e_2 \cos[\kappa_2 x + \varphi_2], \text{Boundary 2: } x = a_1 \quad (3.36)$$
$$(ic/\omega)\kappa_2 e_2 \sin[\kappa_2 x + \varphi_2]/e_2 \cos[\kappa_2 x + \varphi_2]$$
$$= (ic/\omega)\kappa_3 e_3 \sin[\kappa_3 x + \varphi_3]/e_3 \cos[\kappa_3 x + \varphi_3], \text{Boundary 3: } x = a_2 \quad (3.37)$$
$$(ic/\omega)\kappa_3 e_3 \sin[\kappa_3 x + \varphi_3]/e_3 \cos[\kappa_3 x + \varphi_3]$$
$$= (ic/\omega)\kappa_4 e_4 \sin[\kappa_4 x + \varphi_4]/e_4 \cos[\kappa_4 x + \varphi_4], \text{Boundary 4: } x = a_3 \quad (3.38)$$
$$(ic/\omega)\kappa_4 e_4 \sin[\kappa_4 x + \varphi_4]/e_4 \cos[\kappa_4 x + \varphi_4]$$
$$= (ic/\omega)\kappa_5 e_5 \exp[\kappa_5(a_4 - x)]/e_5 \exp[\kappa_5(a_4 - x)]. \text{Boundary 5: } x = a_4 \quad (3.39)$$

Then we get the following equations:

$$\kappa_0 = -\kappa_1 \tan(\varphi_1), \qquad \text{Boundary 1: } x = 0 \quad (3.40)$$
$$\kappa_1 \tan(\kappa_1 a_1 + \varphi_1) = \kappa_2 \tan(\kappa_2 a_1 + \varphi_2), \qquad \text{Boundary 2: } x = a_1 \quad (3.41)$$
$$\kappa_2 \tan(\kappa_2 a_2 + \varphi_2) = \kappa_3 \tan(\kappa_3 a_2 + \varphi_3), \qquad \text{Boundary 3: } x = a_2 \quad (3.42)$$
$$\kappa_3 \tan(\kappa_3 a_3 + \varphi_3) = \kappa_4 \tan(\kappa_4 a_3 + \varphi_4), \qquad \text{Boundary 4: } x = a_3 \quad (3.43)$$
$$\kappa_4 \tan(\kappa_4 a_4 + \varphi_4) = \kappa_5, \qquad \text{Boundary 5: } x = a_4 \quad (3.44)$$

where the following substitutions must be made.

$$\varphi_1 = -\arctan(\kappa_0/\kappa_1), \quad (3.45)$$

$$\varphi_2 = \arctan[(\kappa_1/\kappa_2)\tan(\kappa_1 a_1 + \varphi_1)] - \kappa_2 a_2, \quad (3.46)$$

$$\varphi_3 = \arctan[(\kappa_4/\kappa_3)\tan(\kappa_4 a_3 + \varphi_4)] - \kappa_3 a_3, \quad (3.47)$$

$$\varphi_4 = \arctan(\kappa_5/\kappa_4) - \kappa_4 a_4, \quad (3.48)$$

$$\kappa_0 = \sqrt{\beta^2 - {k_0}^2 {n_0}^2}, \quad (3.49)$$

$$\kappa_1 = \sqrt{{k_0}^2{n_1}^2 - \beta^2}, \tag{3.50}$$

$$\kappa_2 = \sqrt{{k_0}^2{n_2}^2 - \beta^2}, \tag{3.51}$$

$$\kappa_3 = \sqrt{{k_0}^2{n_3}^2 - \beta^2}, \tag{3.52}$$

$$\kappa_4 = \sqrt{{k_0}^2{n_4}^2 - \beta^2}, \tag{3.53}$$

$$\kappa_5 = \sqrt{\beta^2 - {k_5}^2{n_5}^2}. \tag{3.54}$$

Field amplitudes e are also determined from the boundary conditions.

$$e_1 = e_0 \cos(\varphi_1), \qquad \text{Boundary 1: } x = 0 \tag{3.55}$$

$$e_2 = e_1 \cos(\kappa_1 a_1 + \varphi_1)/\cos(\kappa_2 a_1 + \varphi_2), \qquad \text{Boundary 2: } x = a_1 \tag{3.56}$$

$$e_3 = e_2 \cos(\kappa_2 a_2 + \varphi_2)/\cos(\kappa_3 a_2 + \varphi_3), \qquad \text{Boundary 3: } x = a_2 \tag{3.57}$$

$$e_4 = e_3 \cos(\kappa_3 a_3 + \varphi_3)/\cos(\kappa_4 a_3 + \varphi_4), \qquad \text{Boundary 4: } x = a_3 \tag{3.58}$$

$$e_5 = e_4 \cos(\kappa_4 a_4 + \varphi_4). \qquad \text{Boundary 5: } x = a_4 \tag{3.59}$$

After all substitutions of Eqs. (3.45) to (3.54) into Eqs. (3.40) to (3.44) are made, the only remaining variable is the propagation constant β. The solutions of Eqs (3.40) to (3.44) provide the complete spectrum of the light propagation in the waveguide.

3.3 Numerical Simulations: Wave Optics

In this section, the tactile sensation imaging principle is numerically simulated using Eqs. (3.40) to (3.44). Throughout the numerical simulation, we obtain the electromagnetic wave pattern in the multi-layered optical waveguide and demonstrate the TIR. We also show that if an optical waveguide is deformed by an external force, the light is scattered and seen from the surface of an optical waveguide. The wave optics analysis in Section 3.2 becomes too complex for a thick waveguide such as ours because the number of modes in the thick waveguide becomes too large. Therefore, in the numerical simulation, we assume the waveguide is very thin. For a thick waveguide (i.e. few millimeters or larger), the light should be approximated as a ray that uses the geometric optics approximation method. This method will be described in Section 3.4.

Fig. 3.4(a) represents an optical waveguide sensing probe before the light injection, as seen from its side. Three PDMS layers and one glass plate layer are represented by different colors. We assume that the light is injected from the left side of the waveguide. The light injection result is shown in Fig. 3.4(b). Once the light is injected into the waveguide, a small portion of light diffracts away because of the discontinuity of the mediums, air, and the waveguide. However, due to Snell's law, the sinusoidal oscillation of the other light is clearly seen, and it continues to propagate in the waveguide.

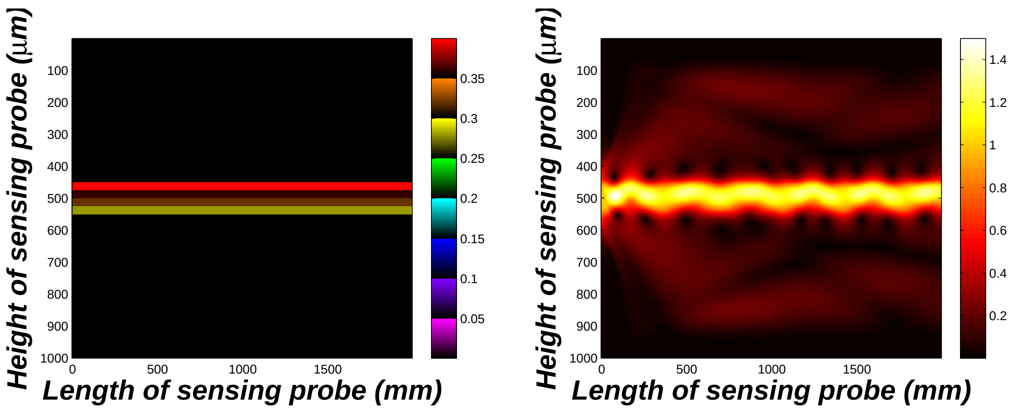

(a) (b)

Figure 3.4: (a) The multi-layered optical waveguide sensing probe as seen from its side. (b) The light propagation under the total internal reflection in the waveguide.

Next, we investigate the light scattering in the case of waveguide deformation. In this simulation, we use the same waveguide as before, except it is compressed with a 10-mm-radius tip for about 5-mm vertical deformation depth (white arrow). The optical waveguide with a small deformation is shown in Fig. 3.5(a). Fig. 3.5(b) shows the light injection result. Once we inject the light into the waveguide, we can clearly see that the light hits the deformed region, which causes the scattering light from the surface of the waveguide (white arrows).

We also simulated to capture the scattering light from the top surface of the waveguide. Fig. 3.6(a) shows the simulation result when the waveguide is not deformed. We can verify that because the light is completely reflected in the waveguide, there is no scattering light that is captured from the top surface of the optical waveguide. Figs. 3.6(b) to 3.6(d) represent the scattered light when the waveguide is deformed vertically with 0, 2, 4, and 6 mm deformation

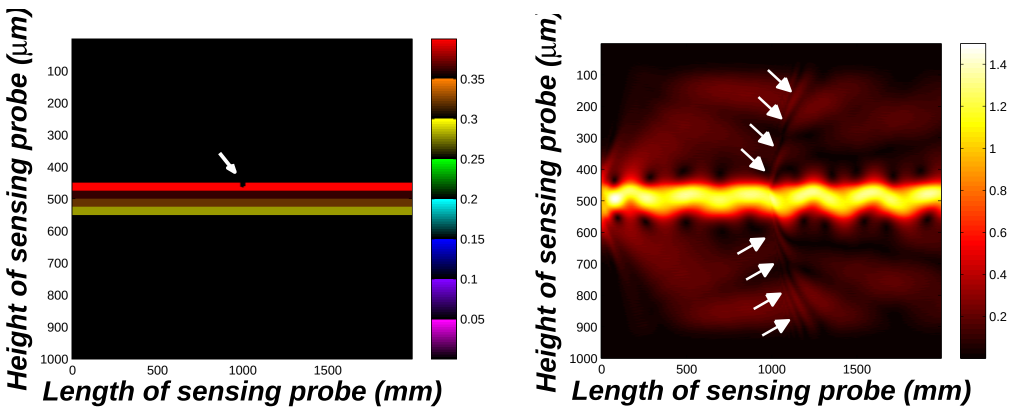

(a) (b)

Figure 3.5: (a) The multi-layered waveguide with small deformation at a distance of 1000 mm as seen from its side. (b) The light dispersion in the waveguide. Notice that scattering lights going out of the waveguide at a distance of 1000 mm.

depth. We can notice that the total amount of scattered light is proportional to the waveguide deformation depth.

3.4 Geometric Optics Approximation

In Section 3.2 and Section 3.3, we considered light propagation in the optical waveguide as an electromagnetic wave, which can be mathematically represented by a solution of Maxwell's equations, subject to boundary conditions at the interfaces between PDMS layers. The theory of this wave propagation is suitable for a waveguide with layers only a few microns thick (Katz, 2002). The wave optic analysis becomes too complex for a case as thick as a few millimeters or larger. Therefore, light propagating in the thick waveguide should be considered as rays. This method, called geometric optics approximation, is an alternative to the wave optics method and is applicable in a waveguide with thick layers as a few millimeters or larger (Katz, 2002). Using the geometric optics approximation, the critical angle and acceptance angle of the light for the TIR can be analyzed. The acceptance angle is the maximum angle within which light is accepted for TIR. To calculate the critical angle and acceptance angle, we used the geometric optics approximation. In this approximation, we assume the light wave as a ray. This allows for determining the direction of light illumination. Consider the geometry as shown in Fig. 3.7. Due to Snell's law, the propagation angles γ in each layer i, i = 0, 1, 2, 3, 4, 5. are bound by the

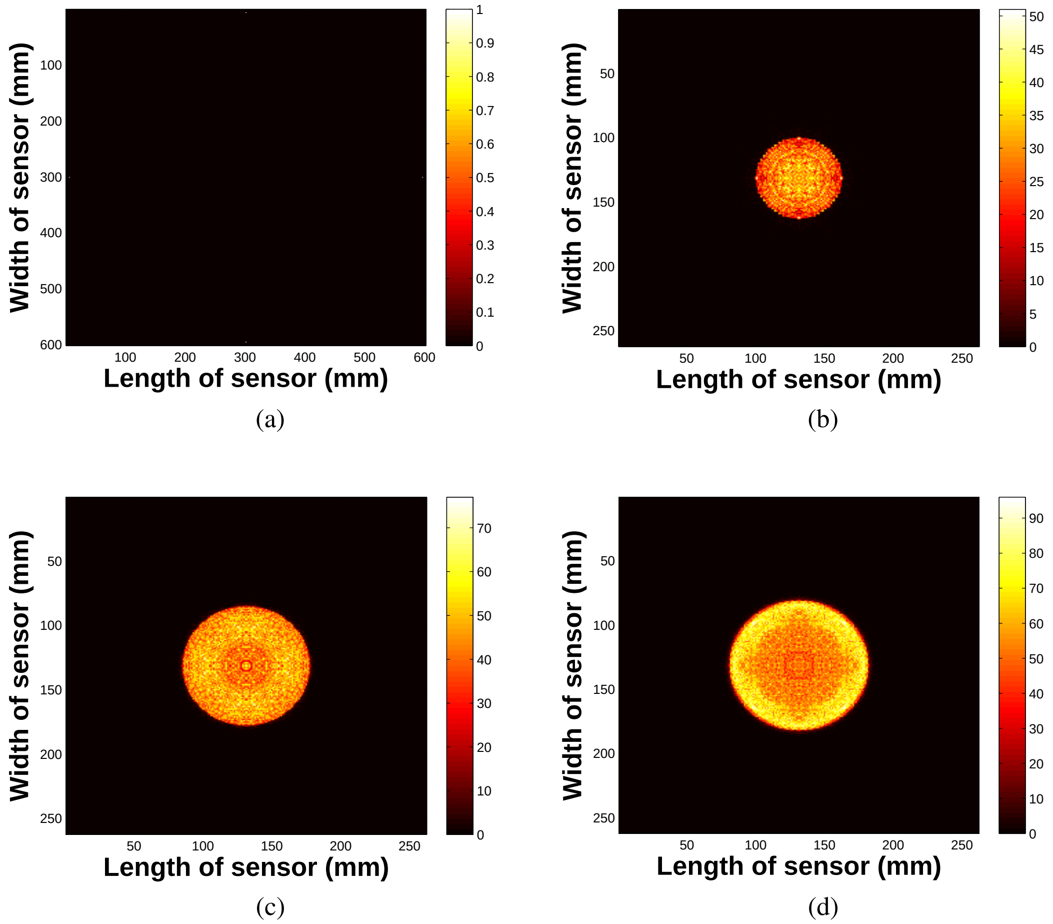

Figure 3.6: The scattered light captured from the top surface of the waveguide when (a) the waveguide is vertically deformed with 0 mm deformation depth, (b) the waveguide is vertically deformed with 2 mm deformation depth, (c) the waveguide is vertically deformed with 4 mm deformation depth (d) the waveguide is vertically deformed with 6 mm deformation depth.

following relations.

$$n_1 \sin \gamma_1 = n_0 \sin \gamma_0, \tag{3.60}$$

$$n_2 \sin \gamma_2 = n_1 \sin \gamma_1, \tag{3.61}$$

$$n_3 \sin \gamma_3 = n_2 \sin \gamma_2, \tag{3.62}$$

$$n_4 \sin \gamma_4 = n_3 \sin \gamma_3, \tag{3.63}$$

$$n_5 \sin \gamma_5 = n_4 \sin \gamma_4. \tag{3.64}$$

The TIR condition has been achieved when $\gamma_0 = \gamma_5 = 90^o$ at the boundaries between the waveguide and air. Light propagating in the waveguide with angles γ_i or higher in their respective layers will be trapped inside the waveguide. The critical angle indicates the minimum propagation angle γ_i. To make the propagation angle γ_i above the critical angle, the acceptance angle θ_i for the incident light to the waveguide is calculated.

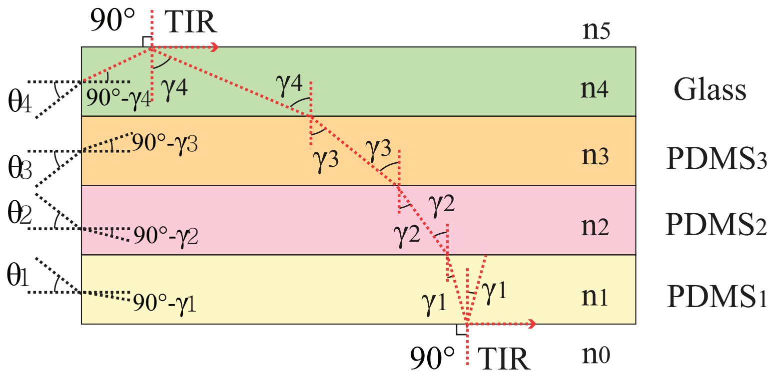

Figure 3.7: Graphic representation of light propagation as a ray, propagating in the waveguide at propagation angles γ_i, $i = 0, 1, 2, 3, 4, 5$.

The acceptance angle θ_i is the maximum angle, under which the light directed into the waveguide remains trapped inside it. The propagation angle γ_i are related to the acceptance angle θ_i by the same Snell's law:

$$\sin\theta_i = n_i \sin(90^o - \gamma_i) = n_i \cos\gamma_i. \tag{3.65}$$

Further, transforming Eq. (3.65), we obtain

$$\sin\theta_i = n_i \cos\gamma_i = n_i(1 - \sin^2\gamma_i)^{1/2} = (n_i^2 - n_i^2\sin^2\gamma_i)^{1/2}. \tag{3.66}$$

But from Eqs. (3.60) to (3.64), all $n_i \sin\gamma_i$ are equal to n_0, which is equal to 1 for air. Therefore, we finally have the acceptance angle θ_i for each layer i:

$$\theta_i = \mathrm{asin}[(\mathrm{n}_i^2 - 1)^{1/2}]. \tag{3.67}$$

Light, incident on layer i under the acceptance angle θ_i, will be trapped inside the waveguide.

The necessary acceptance angle for TIR is calculated. In the current TSIS design, PDMS layer 1 is the hardest, PDMS layer 2 is the medium, and PDMS layer 3 is the softest. Because the refractive index is increasing as the material becomes harder, we set the refractive index of each layer as 1.16, 1.15, 1.14, and 1.13. Then acceptance angles θ_i are calculated using Eq. (3.67). The results are θ_1 = 36.00^o, θ_2 = 34.60^o, θ_3 = 33.18^o, and θ_4 = 31.75^o. Thus, for the TIR in the waveguide, the spatial radiation pattern of light-emitting diode (LED) light with the angle less than 31.75^o has been chosen and placed to inject the light.

3.5 Multi-layered Sensing Probe Characterization

To maximize the touch sensation of the TSIS, the TSIS sensing probe is fabricated by emulating the three-layered tissue structure. In this section, we demonstrate the advantage of the TSIS three-layered sensing probe over the TSIS single-layered sensing probe. For this purpose, the sensing probe characterization test is carried out to determine the effect of a three-layered sensing probe compared to the single-layered sensing probe on deformation patterns in response to the external force. We first calculate the effective modulus, E_{eff}, of the three-layered sensing probe. Fig. 3.8 shows the schematic of the three-layered sensing probe.

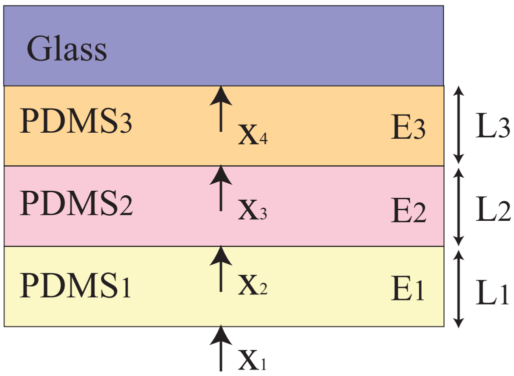

Figure 3.8: The schematic of the three-layered sensing probe.

The conventional stress and strain relation is as below.

$$\sigma = E\varepsilon, \tag{3.68}$$

where σ is the stress, ε is the strain, and E is the Young's modulus. If the uniform force F is applied on the sensing probe surface, then the stress and strain relation can be expressed as below

$$F/A = E \times (\Delta x/L). \tag{3.69}$$

The spring constant can be defined as

$$K = F/\Delta x = (E \times A)/L, \tag{3.70}$$

where A is the cross-sectional area of three layers. Then the stress and strain relations in each layer can be expressed as below.

$$F/(x_1 - x_2) = (E_1 \times A)/L_1, \tag{3.71}$$

$$F/(x_2 - x_3) = (E_2 \times A)/L_2, \tag{3.72}$$

$$F/(x_3 - x_4) = (E_3 \times A)/L_3. \tag{3.73}$$

Here E_1, E_2, E_3 are the respective Young's modulus, L_1, L_2, L_3 are the respective thickness for three layers, and x_1, x_2, x_3, x_4 are displacements of layers under the force F. We note that $x_4 = 0$ because a rigid glass does not allow $PDMS_3$ to move. The displacements of each layer x_1, x_2, x_3 are given as follows,

$$x_1 = (F/A) \times (L_1/E_1 + L_2/E_2 + L_3/E_3), \tag{3.74}$$

$$x_2 = (F/A) \times (L_2/E_2 + L_3/E_3), \tag{3.75}$$

$$x_3 = (F \times L_3)/(E_3 \times A). \tag{3.76}$$

From Eq. (3.70) and Eq. (3.74), the spring constant K_{probe} of sensing probe can be expressed as below.

$$K_{probe} = F/(x_1 - x_4) = A/(L_1/E_1 + L_2/E_2 + L_3/E_3) = (A \times E_{eff})/(L_1 + L_2 + L_3). \tag{3.77}$$

Finally, the effective modulus E_{eff} is as follows.

$$E_{eff} = (L_1 + L_2 + L_3)/(L_1/E_1 + L_2/E_2 + L_3/E_3). \tag{3.78}$$

Thus for a single-layered sensing probe, we need to use an effective modulus E_{eff} of $(L_1 + L_2 + L_3)/(L_1/E_1 + L_2/E_2 + L_3/E_3)$.

To compare the characteristics between single-layered and three-layered sensing probe, the indenter test has been carried out using finite element modeling (FEM) on both single and three-layered sensing probe. In single-layered case, we set the modulus of the sensing probe as the effective modulus E_{eff}. Meanwhile in three-layered case, we set three different modulus E_1, E_2, E_3 in each PDMS layer. Fig. 3.9 and Fig. 3.10 show the maximum deformation and total deformation area curves for two types of sensing probe under the same force F applied to the surface of sensing probe.

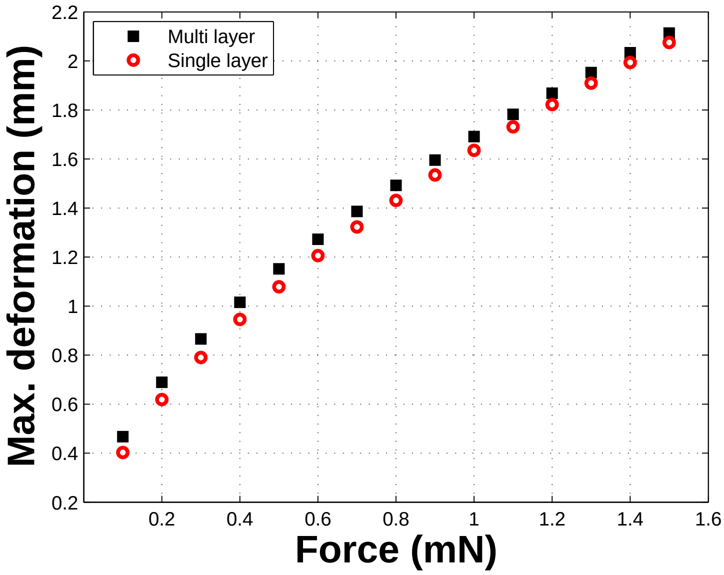

Figure 3.9: Maximum deformation of sensing probe when the uniform force F is applied to the surface of sensing probe.

FEM simulation shows that the deformation area of the multi-layered case varies more than the single-layered case under the same uniform force F applied onto the sensing probe surface. See Fig. 3.10. However, in response to the maximum deformation, the difference between single-layered and multi-layered is not significant. See Fig. 3.9. From these results, we can conclude that, in terms of deformation area, when the same uniform force F is applied to the sensing probe, the multi-layered case is more sensitive to the external force than the single-layered case. But in terms of maximum deformation, the sensitivity to applied force between single-layered and multi-layered cases is not significant. Thus, in the current TSIS design, the three-layered sensing probe is considered, but in the next TSIS design, both the single-layered

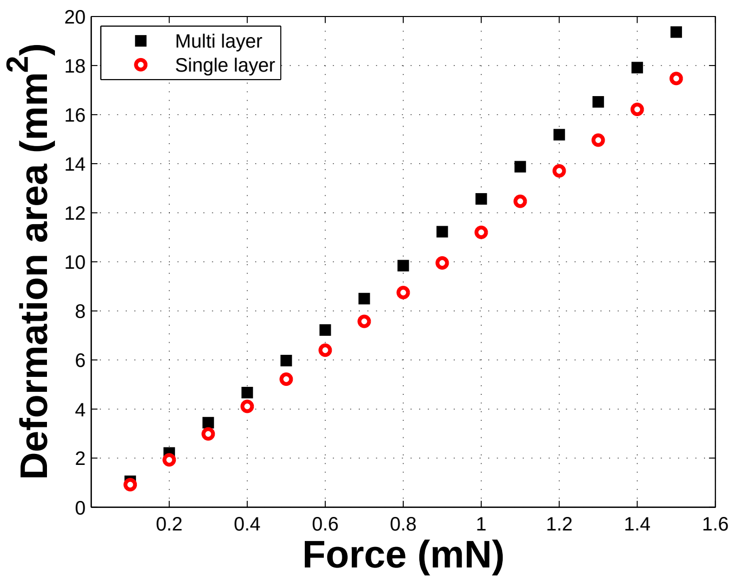

Figure 3.10: Deformation area of sensing probe when the uniform force F is applied to the surface of sensing probe.

and multi-layered sensing probe can be considered for the similar sensitivity to the applied force.

CHAPTER 4

TACTILE SENSATION IMAGING SYSTEM

In this chapter, we present the hardware and software design concepts of the TSIS using the TIR-based imaging principle.

4.1 Overview of Tactile Sensation Imaging System

Fig. 4.1 shows the design overview of the TSIS. The TSIS incorporates an optical waveguide unit, a light source unit, a camera unit, and a computer unit (Lee and Won, 2011a).

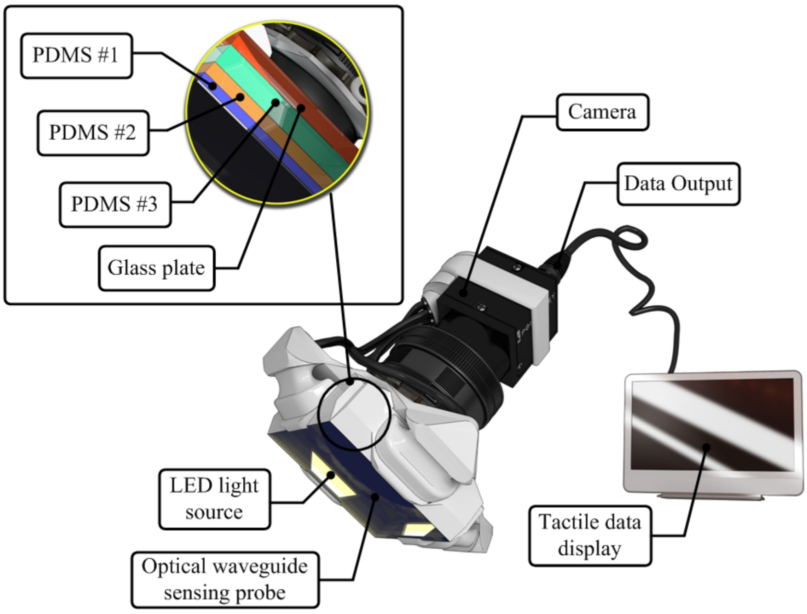

Figure 4.1: The design overview of the tactile sensation imaging system.

The optical waveguide is the main sensing probe of the TSIS. The waveguide is composed of polydimethylsiloxane (PDMS, $Si(CH_3)_2$), which is a high-performance silicone elastomer (Rajan et al., 2003), (Chang-Yen et al., 2005). In the current design, the waveguide needs to be flexible and transparent, and PDMS meets this requirement. To reach the level of the human touch sensation, the tissue structure of the human finger is emulated in the sensing probe (Lee et al., 2010c). The human tissue is composed of three layers with different hardness (Flynn and McCormack, 2009). The epidermis is the hardest layer and it is approximately 1 to 2 mm thick. The dermis is a softer layer, and is approximately 1 to 3 mm thick. The subcutaneous fat is the softest layer, which fills the space between the dermis and bone. It is composed mainly of fat and functions as a cushion when the load is applied to the surface. The thickness of subcutaneous layer is over 3 mm. Due to the difference in hardness of each layer, the inner layer deforms more than the outmost layer when the finger presses onto the object (Kandel et al., 2000). To emulate this structure, three PDMS layers with different hardness were stacked together. PDMS layer 1 is the hardest layer, PDMS layer 2 is the layer with medium hardness, and PDMS layer 3 is the least stiff layer (Kandel et al., 2000). The height of each layer is approximately 2 mm for PDMS layer 1, 3 mm for PDMS layer 2, and 5 mm for PDMS layer 3.

The camera is a mono-cooled complementary CMOS camera with 8.4 μm $\times$ 9.8 μm individual pixel size (Guppy F038, Allied Vision Technology, Germany). The camera is placed below an optical waveguide. A glass plate is placed between the camera and the waveguide to support an optical waveguide (McMaster-Carr, NJ). The internal light source is a LED with a diameter of 3 mm (Parts-Express, OH). There are four LED light sources placed on four sides of the waveguide to provide enough illumination. The direction and incident angle of light is calibrated so that light is totally reflected in the waveguide. The captured tactile data are transferred to a local computer to process and display the tactile data. In the following sections, the hardware and software designs of the TSIS are described in detail.

4.2 Hardware Design of Tactile Sensation Imaging System

In this section, the hardware implementation of the TSIS is described.

4.2.1 Components

Each component of the design for the TSIS is carefully selected so that the proper operation of the TSIS is achieved. Fig. 4.2 shows the TSIS hardware design schematic.

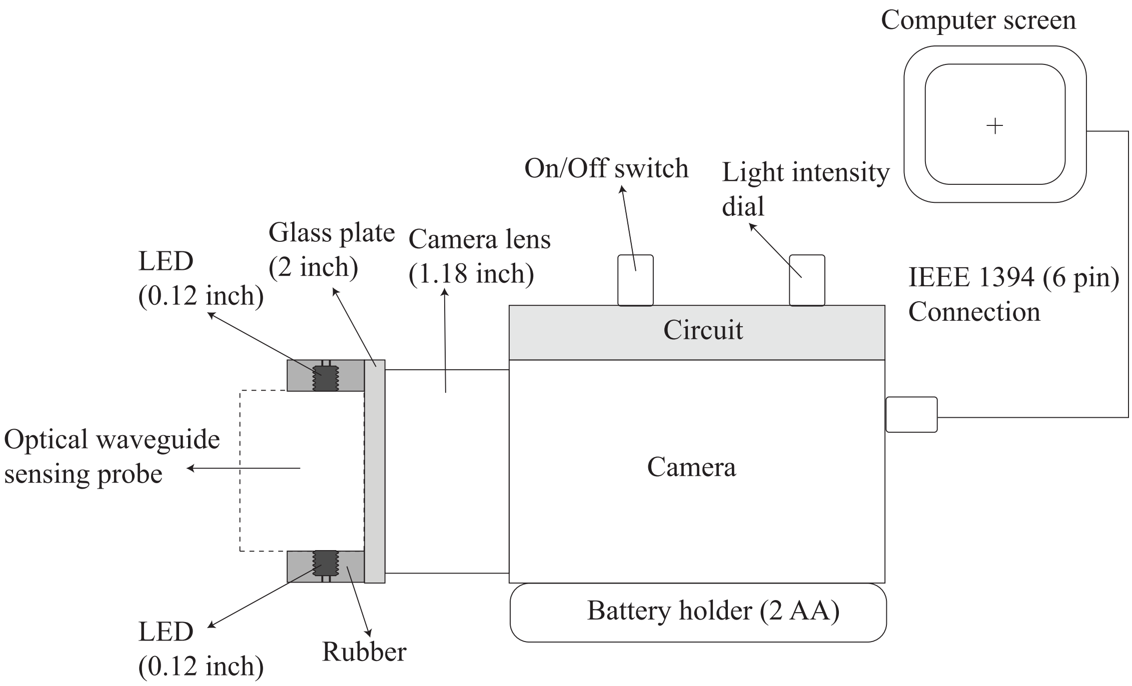

Figure 4.2: Design schematic.

In the following, each component for the TSIS hardware design is described in detail.

Camera

For the camera of the TSIS, the mono-cooled complementary CMOS camera with 8.4 μm $\times$ 9.8 μm individual pixel size is used (Guppy-038, Allied Vision Technology, Germany). The pixel array is 768 (H) $\times$ 492 (V) with 8-bit depth and its maximum resolution is 0.4 megapixel. The camera uses IEEE 1394 (Firewire) interface.

LED

Four ultra-bright white 3-mm LED are used as the light sources of the TSIS (Parts-Express, OH). They are chosen due to their small size (3 mm) and high-output white light intensity (1,500 mcd). Each LED is rated at a typical forward voltage of 3.6 V, a forward current of 20 mA, and a viewing angle of 30^o. The LEDs are arranged in parallel configuration for a common forward current of 3.6 V.

Power Source

Four AA batteries are selected as the DC input power source for four LEDs (Parts-Express, OH). The batteries are rated at 1.5 V each and are configured in series for a total input voltage of 6 V.

Potentiometer

A potentiometer of 0 to 1 $k\Omega$ was selected so that additional resistance can be added to the circuit to control the light intensity of the LEDs (Parts-Express, OH). By increasing the resistance in the circuit, the input voltage to the LED is decreased, thereby creating a dimming effect in the LED light intensity.

Manual Toggle Switch

A manual on/off toggle switch is used to manually control the current on or off into the circuit (Parts-Express, OH).

4.2.2 Optical Waveguide Fabrication

In this section, the fabrication method of optical waveguide for the TSIS sensing probe is introduced. For the material of the optical waveguide, one of the polydimethylsiloxane (PDMS, $Si(CH_3)_2$) dielectric gels, RTV6186, is used (Momentive Performance Materials Inc., NC). These are low viscosity liquid silicones which cure to form a very soft gel-like elastomer. Two PDMS component materials (part A and part B) are supplied, where part A is a base agent and part B is a curing agent. By mixing these two components, the final PDMS optical waveguide can be produced.

Principle

Cured properties of PDMS can be ensured if they are mixed at a ratio of 1:1 (by weight). Increasing the ratio of part A to part B will yield a softer PDMS (higher penetration value) whereas decreasing the ratio of part A to part B will result in a harder PDMS (lower penetration value).

Fablicated PDMS Optical Waveguide

The fabricated PDMS optical waveguide sensing probe is shown in Fig. 4.3(a). The optical waveguide is flexible and transparent. The optical waveguide with LED light injection is also shown in Fig. 4.3(b).

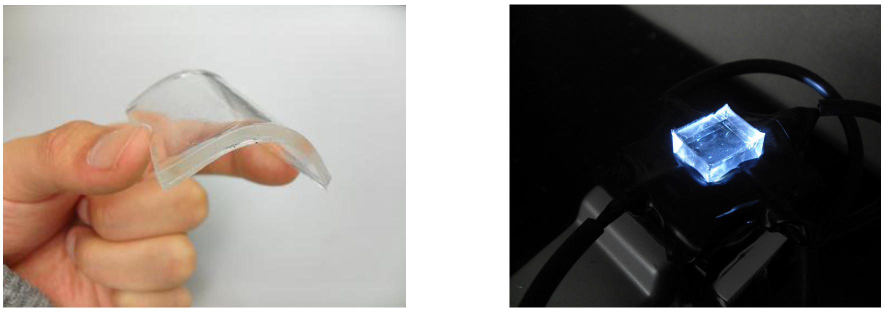

(a) (b)

Figure 4.3: The fabricated optical waveguide sensing probe. The optical waveguide is flexible and transparent. (a) The sample of optical waveguide, (b) The optical waveguide with LED light injection.

4.3 Software Implementation of Tactile Sensation Imaging System

In this section, the software implementation of the TSIS is described in detail. The TSIS software is built using MATLAB software, a numerical computing environment and fourth-generation programming language (MathWorks Inc., MA).

4.3.1 Overview

The TSIS software is made to be able to be viewed by an IEEE 1394 (Firewire) camera, webcam camera, USB camera, or any digital camera that is capable of being recognized in MATLAB software. The graphical user interface (GUI) uses the MATLAB Image Acquisition Toolbox to create a link to the camera in the TSIS and computer. The GUI connects the camera, sets up the camera variables when it is started, and starts the video feed automatically. The basic functionality of GUI is to be able to start and stop the camera, to view a snapshot or current tactile image of the processed video, and to save the current tactile image to file. Fig. 4.4 shows the block diagram of the TSIS software architecture.

The video that comes through the camera is frame-by-frame and has the format specific to

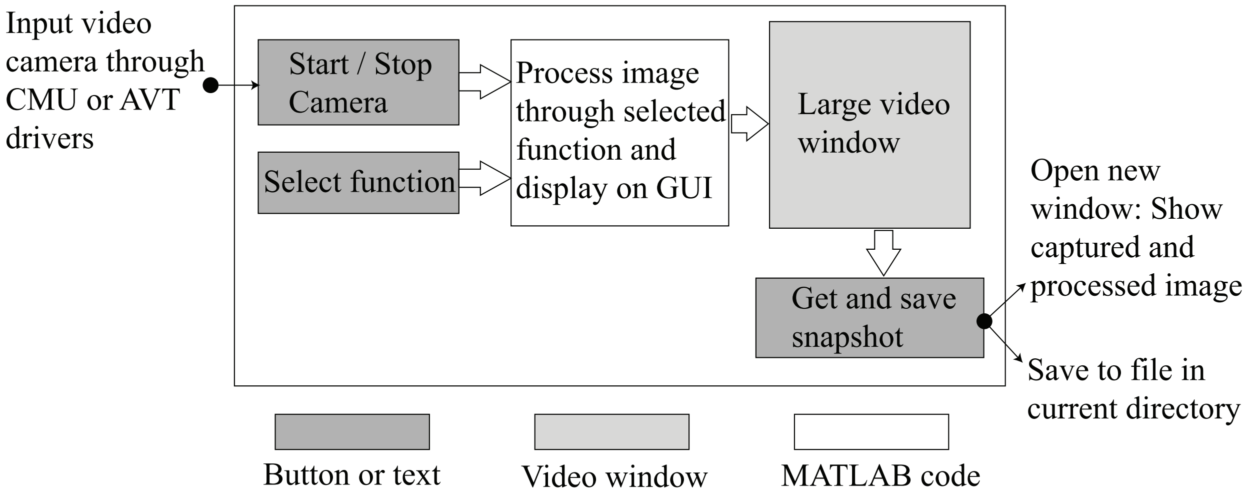

Figure 4.4: The block diagram of the software architecture.

the manufacturer of the camera itself. For example, for the Guppy F-038 camera, the camera sends the IIDC/DCAM specified Format 7 Mode 0 type data, which is a bitmap array with 8-bits per pixel. For this camera, there is either the choice of using the CMU 1394 Digital Camera Driver to connect to the camera or using a ".dll" adapter file provided by AVT and using their UniversalPackage drivers. Basically, all types of digital input devices like IEEE 1394 or USB cameras work with the TSIS software as long as they are setup correctly to function with MATLAB.

4.3.2 Procedure and Functionality of TSIS Software

Before the TSIS software main window, there is a "Select Camera" function that detects any connected cameras that are compatible with MATLAB. This is shown through a small GUI window which has the camera name, manufacturer, and the resolution or mode which the user can select. This allows for an easy switch to another camera or different resolution without having to alter the internal code of the TSIS software. Fig. 4.5 shows the initial window of the TSIS software.

The left side of the "Select Camera" window has the manufacturer-specific name of the camera, i.e. "AVT Guppy F038C NIR". The second field has the different supported resolutions

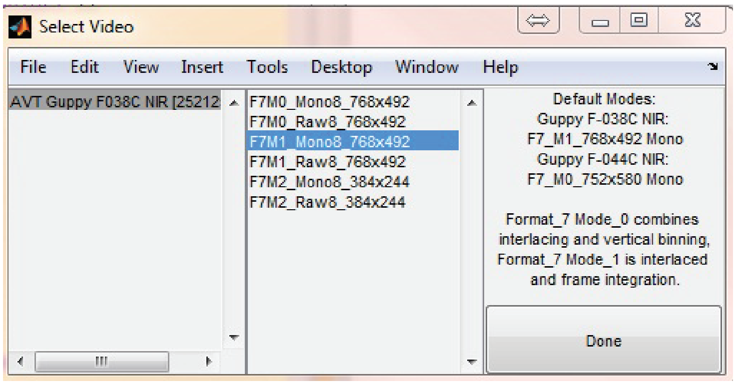

Figure 4.5: Initial window of tactile sensation imaging system software.

or "modes" that the camera selected offers. The AVT cameras have different "Format" and "Mode" settings that are used to display video. The AVT Guppy F038 camera uses the "F7M0-Mono8-768 $\times$ 492" setting, or the Format7 and Mode0, 8-bit monochrome, 768 vertical by 492 horizontal pixels. The main window of the TSIS software is shown in Fig. 4.6. The main window has the following functional buttons.

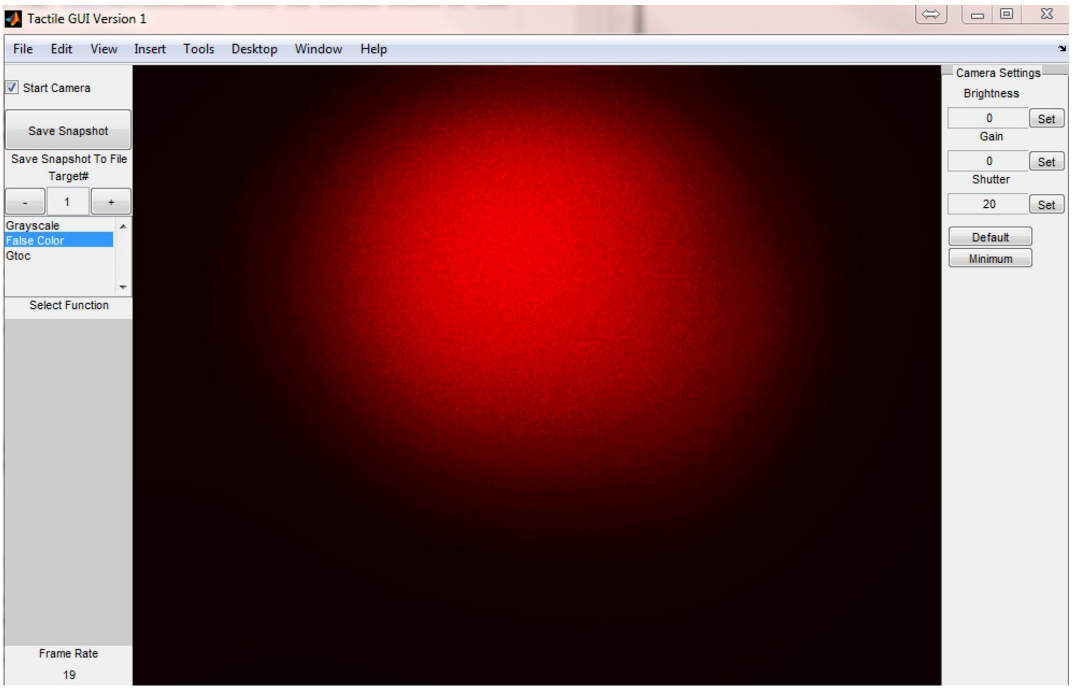

Figure 4.6: The graphical user interface of tactile sensation imaging system software.

Start/Stop Camera Checkbox

The default state of this checkbox is “on”, as the software starts the camera upon startup. When clicking the checkbox to an “off” state, the window tries to execute a “stop” command. To start the camera again, a “start” command should be issued again by clicking the checkbox to an “on” state. While this checkbox is in the “on” state, the video will continue to process and show on the GUI.

Save Snapshot Button

This button brings up a new figure which shows the image capture of the current video. The video continues to run in the background, and this figure is a default MATLAB figure with no extra properties. The other functionality of this button is to write the image to file with a selected format and name. The current format writes a “.bmp” file format and uses the current timestamp and the desired target number as the name of the image. Thus, the saved image would appear in a folder under the current working directory, the target number folder, as “Target1-020411-131112.bmp”, for an example target number of 1. The “020411” corresponds to the date (February, 2, 2011) and “131112” corresponds to the time (13 : 11 : 12) in hour : minute : second format. Consequently, there will never be overlapping images since the file name uses the current second in the timestamp. The image format could be changed to specify different image formats such as “.bmp”, “.jpeg”, “.jpg”, “.png”. The current default setting is a 24-bit RGB Bitmap color. This function saves both the processed image (color image), and the raw gray-scale image together as an identical file with the raw gray-scale image having a “-raw” tag appended to the file name.

Target Selection User Interface

The target selection user interface is for choosing the target number. The interface consists of the target number starting at the default target number of 1 and increasing or decreasing the selected value with the “+” or “–” interface or manually typing in the desired number into the edit field. This selects the target number and the folder name where they can store the image.

Camera Settings Panel

A few available camera settings are found and shown on the right side of the GUI, showing values such as brightness, gain, and shutter speed. In the camera setting panel, an edit box is created and controls the settings directly. Once the value in the camera setting panel is changed, the Guppy F038 camera will change its internal settings and the video will propagate the changes. There are two added buttons next to the camera setting panel, for allowing a quick change of settings with either a "default" or a "minimal" state that selects values for each of the setting parameters and sends them to the camera.

4.4 Sample Tactile Images

Sample tactile images are obtained using the TSIS and its software. To get a sample tactile image of tissue inclusion, a realistic breast tissue phantom with a 2-mm diameter spherically shaped inclusion is manufactured (MammaCare Corp., FL). Using the TSIS, the tactile data of an inclusion are obtained with a 0.7 N normal compression ratio. Fig. 4.7(a) shows the initial gray-scale tactile data. In Fig. 4.7(b), a color-scale replace the original gray-scale for the clear visualization. Then, the 3-D reconstruction of tactile image is performed using the pixel value as the depth information in Fig. 4.7(c).

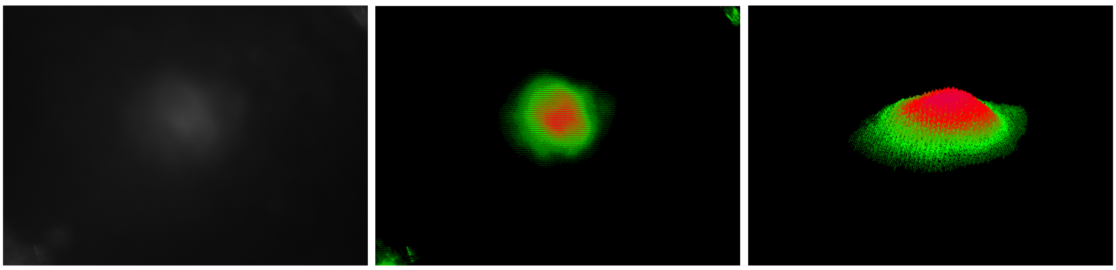

(a) (b) (c)

Figure 4.7: The tactile imaging experiments for a tissue inclusion. (a) Obtaining tactile image of a tissue inclusion using TSIS, (b) Raw gray-scale tactile image, (c) Color visualization with 3-D reconstruction.

From the sample tactile image, we notice that since the light scatters from the optical waveguide on the contact area, the pixel values of the tactile image distribute in a bell shape, where the pixel intensity is the highest at the centroid of the data and decreases as the distance from the centroid of the data increases. In Chapters 5 and 6, the advanced tactile data processing algorithms will be introduced to estimate the hardness of the touched object or the parameters of tissue inclusion such as size, depth, and hardness using tactile image.

4.5 The Specification of the Tactile Sensation Imaging System

In this section, the TSIS is characterized and compared with the specification of the human fingertip. The detailed description of the TSIS specification is given below.

1) Spatial resolution between sensing points: The spatial resolution between sensing points of the fingertip is at least 0.1 mm, which translates into an approximately 200 $\times$ 300 elements grid on a fingertip size area (20 mm $\times$ 30 mm) (Saga et al., 2007), (Johanson and Philips, 1981). The spatial resolution of the TSIS is the pixel size of the camera. In the TSIS, the pattern discrimination ability is 9.8 μm and translates into an approximately 2041 $\times$ 3061 elements grid on the same fingertip size area. This makes the TSIS have high tactile spatial resolution.

2) Temporal resolution: With regard to the human fingertip temporal resolution, the fingertip vibration bandwidth is a few Hz for separate touches and a hundred Hz for sensing vibration (Kandel et al., 2000), (Craig and Baihua, 1990). The Guppy F038 camera that is used in the TSIS provides 768 $\times$ 492 resolution at 30 frames per second (30 Hz).

3) Force sensitivity: Force sensitivity is described in terms of the smallest input physical signal (input) to generate the output electrical signal (Rajan et al., 2003). Force sensitivity of the TSIS is approximately 2.5×10^{-3} N compared to the human fingertip force sensitivity of 2.0×10^{-2} N.

4) Hysteresis: Human fingertip does not return to the same output value (skin relax) when the input stimulus (applied force onto the fingertip) returns to its original value in a path different from the path that was previously used (Uttal, 1973). This difference is due to hysteresis. The TSIS does not show hysteresis. In addition, the TSIS is stable, repeatable and continuous in its variable output signal.

Table 4.1 summarizes the sensory specification of the human fingertip and TSIS.

Table 4.1: Sensory specification of the human fingertip and tactile sensation imaging system.

Design criteria	Human fingertip	Tactile sensation imaging system
Spatial resolution	0.1 mm	9.8 μm
Temporal resolution	0$\sim$100 Hz	0$\sim$30 Hz
Force Sensitivity	2.5×10^{-2} N	2.0×10^{-3} N
Hysteresis	High	Low

CHAPTER 5

TARGET HARDNESS ESTIMATION BY DIRECT CONTACT

In this chapter, we estimate the hardness of the touched object using tactile data. The word "hardness" is used to describe the mechanical property of the touched object obtained by palpation. The hardness is expressed by the Young's modulus, E, having units of force per unit area. Young's modulus is the ratio of stress to strain. The stress is defined as the applied force per unit area. The strain is the fraction change in length in response to the stress. Thus the Young's modulus is expressed as stress over strain as below,

$$E = stress/strain. \tag{5.1}$$

In this chapter, we estimate the Young's modulus of the touched object using tactile data obtained by the TSIS.

5.1 Stress Estimation

The stress is measured as force per unit area. In the TSIS design, if the optical sensing probe of TSIS is compressed by a touched object, it is deformed. Then the light scatters at the contact area. This scattered light is captured by a camera. Let $I(x, y)$ be the individual pixel value of the captured tactile data. Since $I(x, y)$ is proportional to the stress, $P(x, y)$, it can be expressed as follows:

$$P(x, y) = f(I(x, y)), \tag{5.2}$$

where f is the conversion function. If C is designated as the contact area, then the force F is obtained by integrating the stress over the contact area as follows:

$$F = \int_C P(x, y) dC. \tag{5.3}$$

The relationship between force and summation of pixel values in tactile data is established via experiments using a loading machine.

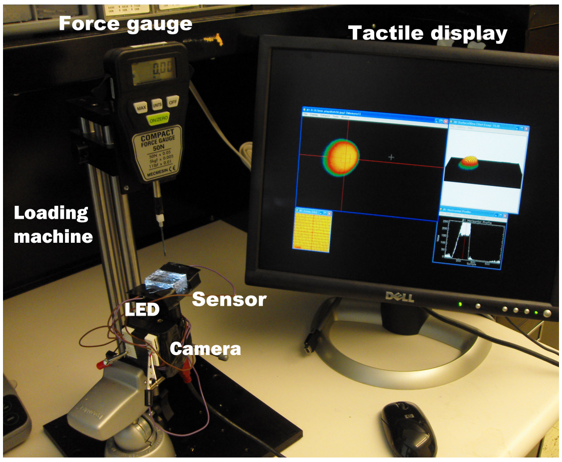

Figure 5.1: The loading machine experiment setup. This setup is used to find the relationship between the normal force and the summation of pixel values in tactile data.

As shown in Fig. 5.1, the loading machine that we used have a force gauge (Mecmesin, West Sussex, UK) to detect the applied force to the waveguide. The force gauge has a probe to measure the force from the range of 0 to 50 N with the resolution of 1.0×10^{-3} N. Since the camera is an 8-bit digital camera, each pixel has a minimum value of 0 and a maximum value of 255. We attached a small tip with 2 mm radius to the force gauge to compress the waveguide. In this experiment, starting from the initial force of 0 N, the force was increased in the steps of 0.1 N. When the force reached the maximum value of 2.0 N, it was decreased in a stepwise fashion until it returned to 0 N. The resulting scattered light caused by compression of the waveguide was captured by a camera, and the corresponding applied force was measured by the force gauge using the tactile data.

Fig. 5.2 shows the pixel values along the contact area's of horizontal cross-sections of the tactile data. As expected, the graph is Gaussian shape and the maximum value is at the centroid of the tactile data. The plot of summation of pixel values in tactile data versus applied normal force is shown in Fig. 5.3. As shown in the result, TSIS exhibits a linear response, good repeatability and low hysteresis. The hysteresis loop is not observed in the curve. To find the relationship between the force and the summation of pixel values in tactile data, the linear regression method was used as below.

$$y = 1.0 \times 10^6 \times (0.056 + 1.4778x), \tag{5.4}$$

where x is the normal force with mN unit and y is the summation of pixel values without units. Using the linear regression result, if we get a new tactile data, we can estimate the normal force x throughout the calculation of summation of pixel values in tactile data y. Note that the relation curve in Fig. 5.3 will be changed if the hardness of TSIS sensing probe is changed or the light intensity into the TSIS sensing probe is changed.

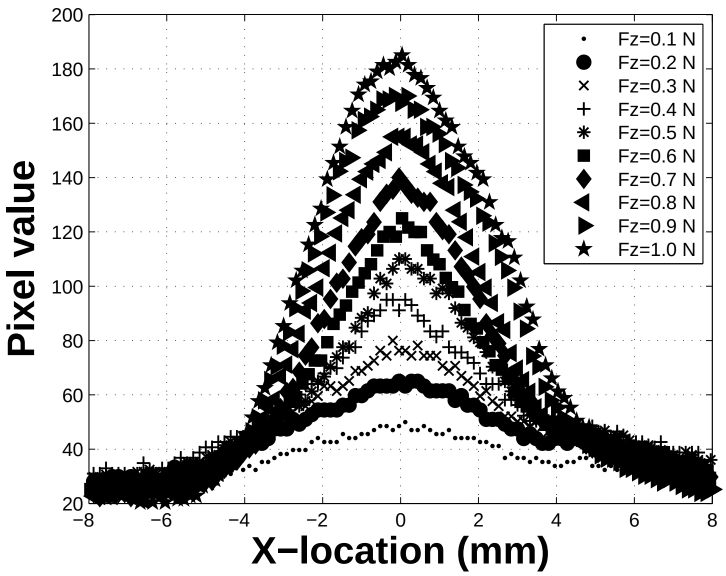

Figure 5.2: The pixel value along the contact area (horizontal direction) as the normal force varies.

Since the stress is measured as force per unit area, the final estimated stress, $\hat{P}$, is as follows:

$$\hat{P} = x/C, \tag{5.5}$$

where x is the normal force obtained from Eq. (5.4) and C is the contact area.

In this experiment, we assume that the measured object is smaller than the TSIS sensing probe area. Then the contact area, C, becomes the size of the object. In this case, the contact area, C, is estimated by the light scattering area in tactile data. The scale factor between the

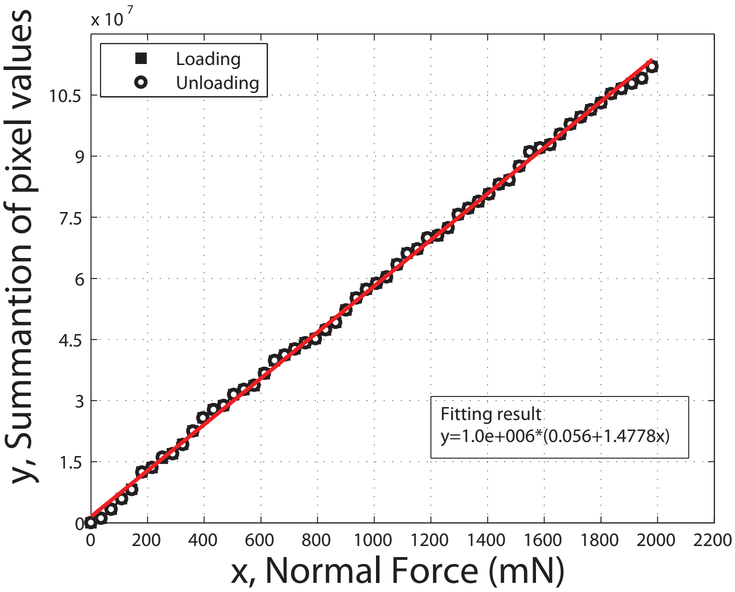

Figure 5.3: The relationship curve between the normal force and the summation of pixel values in tactile data.

actual size and the image pixel distance is 6.79×10^{-3} mm per pixel. We obtained this ratio by the calibration.

In this experiments, the relationship curve in Fig. 5.3 was obtained using a small, stiff tip indenter. Strictly speaking, the relationship curve is only valid for a stiff material. But we use this curve for the soft polymer, because both materials are homogeneous and isotropic. There will be some errors due to the material differences. In addition, we have obtained the calibration curve using the loading machine with 2 mm radius tip. Theoretically, the relationship curve can be used to estimate forces applied on the objects of different sizes. To investigate the applied normal force estimation capability using tactile data in more samples of bigger size, we find the relationship curve in response to the different tip size of the loading machine. The size of tips we used were radius of 10 mm and 14 mm. We obtained 15 tactile data of each tip size case under different loading forces and calculated the summation of pixel values in tactile data. Then the linear regression line was obtained. The experimental results are shown in Fig. 5.4.

According to the Hertzian contact theory, the relationship curve should match each other regardless of the different indenter sizes (Filonenko-Borodichm, 1965). However, the result

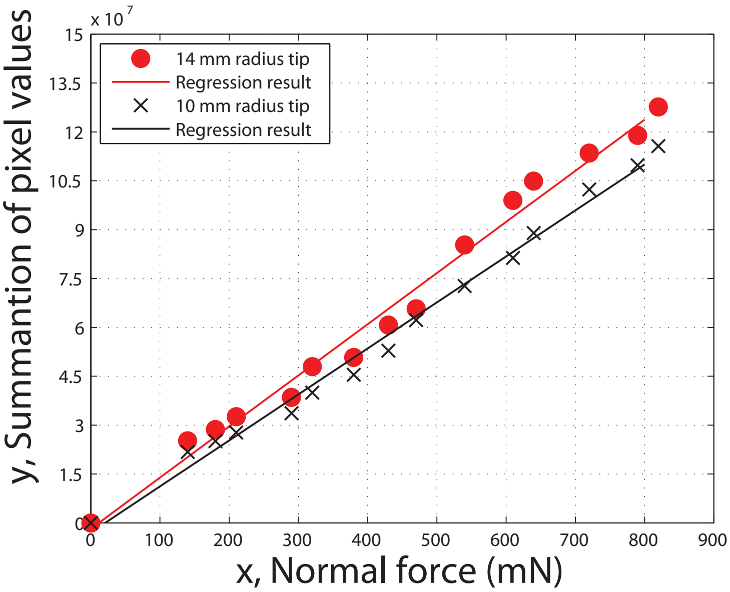

Figure 5.4: The relationship between the normal force and summation of pixel values in tactile data in response to the different loading machine tip radius.

shows that there exist some differences between linear regression lines. At 800 mN normal force, the error between two cases is 2.45%. There can be many reasons for this error. The impurity of the optical waveguide is one reason. The unequal distribution of lights in the optical waveguide due to the misalignment of LED position is another reason. In this experiment, we assume that this error is included with the total estimation error.

5.2 Strain Estimation

The other value needed for the Young's modulus estimation is the strain. Strain is the geometrical deformation measure indicating the relative displacement between points on the object. Thus if we know the displacement of any particular set of points on tactile data obtained under different loading forces, then we can find the strain of the compressed object. The point displacements can be calculated by matching each point sets between tactile data and compute the distance between point position in one tactile data and point position in another tactile data (Bruck et al., 1989). To matching two different tactile data efficiently, a novel non-rigid point matching algorithm called "topology preserving relaxation labeling (TPRL)" has been developed (Lee and Won, 2011b). The essence of this algorithm is to automatically measure the displacement by tracking the change in position of control points extracted from two different tactile data (Johnson and Christensen, 2002a), (Johnson and Christensen, 2002b). Fig. 5.5 represents the concept of tracking control points between 3-D reconstructed tactile data obtained under two different loading forces on the same object. The 3-D reconstruction of tactile data is performed using the pixel value as the depth information.

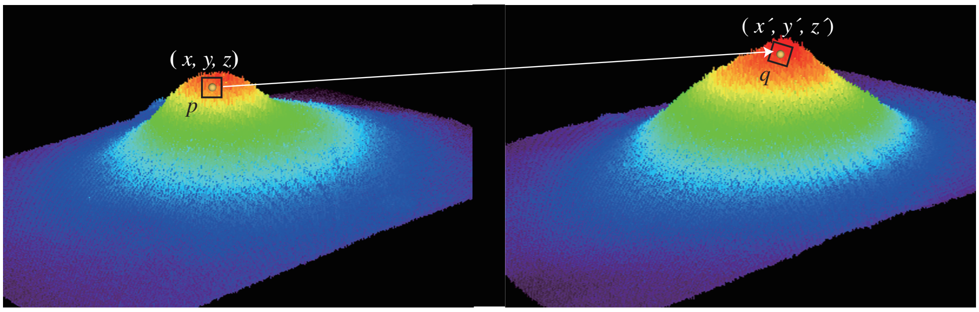

Figure 5.5: Tracking control points extracted from surface of two different tactile data to estimate the strain.

TPRL uses iterative algorithm to find appropriate correspondence and transformation function between control points. The displacement of the contacted object deformation is obtained from the transformation function. This displacement function is finally used to estimate the strain information. We show that the proposed TPRL algorithm significantly improves the matching performance compared to other state-of-the-art point matching algorithms in (Lee and Won, 2011b). That is the reason why we use TPRL for the strain estimation. In this section, TPRL algorithm for strain estimation is described in detail.

5.2.1 Problem Definition

The point matching using point features is widely used in computer vision and pattern recognition as point representations are generally easy to extract (Brown, 1992), (Johnson and Christensen, 2002b). The point matching problem can be categorized as rigid matching and non-rigid matching based on the deformation of objects captured in the images. Compared with a rigid case, a non-rigid matching is more complex. Most non-rigid point matching methods use an iterated estimation framework to find appropriate correspondence and transformation (Zitova, 2003), (Rangarajan et al., 1997).

The iterated closest point (ICP) algorithm is one of the most well-known heuristic approaches (Besl and Mckay, 1992). It utilizes the relationship by assigning the correspondence with binary values of zero or one. However, in the case of non-rigid transformation this binary assumption is no longer valid, especially when the deformation is large.

The thin plate spline robust point matching (TPS-RPM) algorithm is an expectation maximization (EM) algorithm to jointly solve for the feature correspondence as well as the geometric transformation (Rangarajan et al., 1999). The minimizing cost function is the summation of Euclidean distances between the matching points. In TPS-RPM, the binary correspondence value of ICP is relaxed to the continuous value between zero and one. This soft-assign method improves the matching performance as the correspondences are able to improve gradually and continuously, without jumping around in the space of binary permutation matrices (Rangarajan et al., 1996). The algorithm is robust compared to ICP in the non-rigid case, but the joint estimation of correspondence and transformation increases the algorithm complexity. Furthermore, the Euclidean distance makes sense only when there are at least rough initial alignments of the shapes. If the initial points are not aligned well, the matching result is poor.

The coherent point drift (CPD) method is another probabilistic algorithm applied to the non-rigid point matching problem (Myronenko and Song, 2010). The CPD algorithm utilizes the displacement field between two point sets and it has been extended to the general non-rigid registration framework with TPS-RPM as a special case.

Another approach is the shape context (SC) method, which uses an object recognizer based on the shape (Belongie et al., 2002). For each point, the distributions of the distance and orientation to the neighboring points are estimated through a histogram. There distributions are used as the attribute relations for the points. The correspondences are chosen by comparing each point's attributes in one set with the attributes of the other. Only the attributes are considered, thus a search for the correspondences can be conducted more easily compared to ICP and TPS-RPM. Generally speaking, the SC method performs better in the handling of complex patterns than TPS-RPM.

A recently proposed matching method, the robust point matching-preserving local neighborhood structures (RPM-LNS) algorithm, employs a neighborhood structure concept for the general point matching problem (Zheng and Doermann, 2006). In RPM-LNS the cost function is formulated as an optimization problem to preserve local neighborhood relations. The matching probability is refined through the relaxation labeling process. We will compare the performance of these algorithms with our approach.

Another interesting point matching approach is the kernel correlation (KC) based method (Tsin and Kanade, 2004). The cost function of KC is proportional to the correlation of two kernel density estimates. The work was extended by using the $L2$ distance between Gaussian mixture models representing the point set (Jian and Vemuri, 2005). Since the RMS matching errors of the KC approach and the L2 distance approach are relatively higher than the other available algorithms such as TPS-RPM, SC, RPM-LNS, and CPD, we have not included the matching results of these two methods in the experimental results.

To develop an efficient non-rigid point matching algorithm, we generalize RPM-LNS by introducing the optimal compatibility coefficient for the relaxation labeling method to solve a non-rigid point matching problem. The relaxation labeling is an iterative procedure that reduces local ambiguities and achieves global consistency by exploiting contextual information which is quantitatively represented by "compatibility coefficient" (Rosenfeld et al., 1976), (Hummel and Zucker, 1983). It is widely known that the relaxation labeling process is greatly affected by the choice of the compatibility coefficient (Peleg and Rosenfeld, 1978), (Pelillo and Refice, 1994).

In the method of Zheng and Doermann, the compatibility coefficient value was a binary value of zero or one, depending on whether a point and its neighboring point have corresponding points (Zheng and Doermann, 2006). In our method, the correlation between point pairs is measured by the proposed compatibility function, which quantifies the amount of similarity and spatial smoothness between the point pairs in n-discrete values. This contextual information combined with a relaxation labeling process is used to search for a correspondence. Then the transformation is calculated by the thin plate spline (TPS) model (Bookstein, 1989). These two processes are iterated until the optimal correspondence and transformation are found. The proposed relaxation labeling, with a new compatibility coefficient, preserves a topology of point set, thus we call our method the topology preserving relaxation labeling (TPRL) algorithm (Lee and Won, 2011b). It is important to note that changing compatibility coefficient improves the matching performance significantly. In the next section, we describe TPRL in detail.

5.2.2 Topology Preserving Relaxation Labeling (TPRL) algorithm

Let two 3-D reconstructed tactile data obtained under different loading forces as O_1 and O_2. From the surface of O_1 and O_2, a number of control points are extracted. Let $P = \{p_1, p_2, ..., p_I\}, p_i \in \Re^3$ be a point set extracted from O_1 and $Q = \{q_1, q_2, ..., q_J\}, q_j \in \Re^3$ be a point set extracted from O_2. If the object is deformed by the contact of the sensing probe, the distance between the points changes, especially when points are far apart. However, the local adjacent points of each point will not change much due to physical constraints (Zheng and Doermann, 2006). So we define the local adjacent points of each point. For a given point, $p_i \in P$, one can select adjacent points $\mathcal{N}_a^{p_i}$, $a = 1, 2, ..., A$, which are in the circle centered at p_i. We set the radius of a circle as the median value of all Euclidean distances between point pairs in P. Similarly, for a point, $q_j \in Q$, adjacent points are $\mathcal{N}_b^{q_j}$, $b = 1, 2, ..., B$. We determine the fuzzy correspondence matrix M. Each element of $M_{p_i q_j}$ has continuous value between [0,1] and it indicates the correspondence weight between p_i and q_j. Same as $M_{p_i q_j}$, $M_{\mathcal{N}_a^{p_i} \mathcal{N}_b^{q_j}}$ has continuous value between [0,1] and it indicates the correspondence weight between $\mathcal{N}_a^{p_i}$ and $\mathcal{N}_b^{q_j}$.

The optimal match $\hat{M}$ is found by maximizing the energy function as follows.

$$\hat{M} = \arg\max_{M} E(M), \tag{5.6}$$

where

$$E(M) = \sum_{i=1}^{I} \sum_{b=1}^{B} \sum_{j=1}^{J} \sum_{a=1}^{A} M_{p_i q_j} M_{\mathcal{N}_a^{p_i} \mathcal{N}_b^{q_j}} \tag{5.7}$$

subject to $\sum_{i=1}^{I} M_{p_i q_j} = 1, \forall i$, and $\sum_{j=1}^{J} M_{p_i q_j} = 1, \forall j$, and $M_{p_i q_j} \in [0, 1]$.

5.2.3 Searching Point Correspondence

Initially, each point $p_i \in P'$ is assigned with a set of matching probability based on the shape context distance. After the initial probability assignment, the relaxation labeling process updates the matching probability. The purpose of the subsequent process is to assign a matching probability that maximizes $C(P', Q', M)$ under the relaxed condition as $M_{p_i q_j} \in [0, 1]$. At the end of the relaxation labeling process, it is expected that each point will have one unambiguous matching probability. We follow the relaxation labeling updating rule as below (Wu and Pairman, 1995).

1) Compute the compatibility coefficient which imposes the similarity and spatial smoothness constraints between point pairs.

2) Compute the support function from all compatibility coefficients related to the point.

3) Update the matching probability depending on its support function.

The determination of the compatibility coefficients is crucial because the performance of the relaxation labeling process depends on them. As a key contribution, we define a new compatibility coefficient to relax the binary value into multiple discrete values. The proposed compatibility coefficient quantifies the degree of agreement between the hypothesis that p_i matches to q_j and $\mathcal{N}_a^{p_i}$ matches to $\mathcal{N}_b^{q_j}$. It is measured by the set of vectors originating from a point and extending to all other sample points. The full set of vectors increases the algorithm complexity and processing time. To simplify and speed up the process, log distance and polar angle bins are used to capture the coarse location information (Belongie et al., 2002). The bins are uniform in log-polar space, which makes the descriptor more sensitive to positions of adjacent points than to those of points far apart. In the diagram, the distance is defined as zero in the origin and incremented by one towards the outer bins as shown in Fig. 5.6(a).

Let $d(p_i, \mathcal{N}_a^{p_i}) \in \mathbb{N}$ be the distance between origin point p_i and its nearest adjacent points. Then the distance set of an origin point p_i is defined as
$\mathcal{DS}(p_i) = \{d(p_1, \mathcal{N}_a^{p_1}), d(p_2, \mathcal{N}_a^{p_2}), ..., d(p_i, \mathcal{N}_a^{p_i})\}$. For the computation of the angle between point pairs, the alignment of a diagram with a reference point is necessary. In this research, the

mass center of a point set is used as a reference point. The direction from a point to the center of mass is set as the positive x-axis of the descriptor. From this axis, the angle is incremented by 1 in a counter clockwise direction. Let $l(p_i, \mathcal{N}_a^{p_i}) \in \mathbb{N}$ be the angle between origin point s_i and its nearest adjacent points. The angle set of an origin point s_i is given as $\mathcal{ANG}(p_i) = \{d(p_1, \mathcal{N}_a^{p_1}), d(p_2, \mathcal{N}_a^{p_2}), ..., d(p_i, \mathcal{N}_a^{p_i})\}$. Every point can be an origin and the origin varies with points in consideration to calculate the location information. Figs. 5.6(b) and 5.6(c) show the distance and angle sets for a given point $p_i \in P$ and its corresponding point $q_j \in Q$.

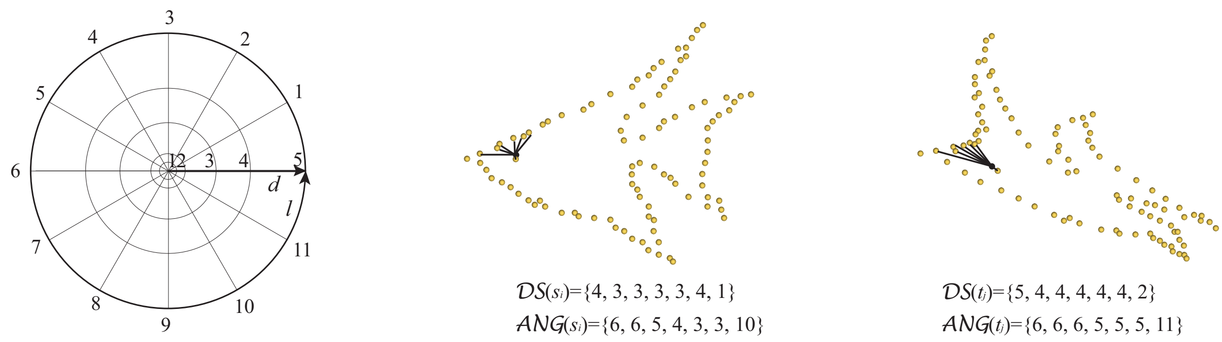

(a) (b) (c)

Figure 5.6: The distance and angle computation. (a) Diagram of log-polar bins used in computing the distance and angle. We use 5 bins for the distances and 12 bins for the angles. (b) A point $s_i \in S$ (black) from the fish shape with its sets $\mathcal{DS}(s_i)$ and $\mathcal{ANG}(s_i)$ of its 6 adjacent points in S. (c) The point $t_j \in T$ (black) in the deformed fish shape which have 6 adjacent points and its distance and angle sets $\mathcal{DS}(t_j)$ and $\mathcal{ANG}(t_j)$.

In the non-rigid degradation of point sets, we note that a point set is usually distorted; however the neighboring structure of a point is generally preserved due to physical constraints. The displacement of a point and its adjacent point between two point sets constrain one another. Thus, if the distance and angle of a point pair $(p_i, \mathcal{N}_a^{p_i})$ in the model shape and its corresponding point pair $(q_j, \mathcal{N}_a^{q_j})$ in the target shape are similar, we say that they have high correlation. This is further strengthened if a point pair $(p_i, \mathcal{N}_a^{p_i})$ in the model shape is closer to each other. To quantify this knowledge, we introduce the similarity constraint α, β as well as the spatial smoothness constraint γ.

The first constraint is the similarity which is related to the differences between the distances and angles of $(p_i, \mathcal{N}_a^{p_i})$ and $(q_j, \mathcal{N}_a^{q_j})$. This first constraint imposes that if $(p_i, \mathcal{N}_a^{p_i})$ has smaller distance and angle differences with $(q_j, \mathcal{N}_a^{q_j})$, then they are more compatible. The disparities between $(p_i, \mathcal{N}_a^{p_i})$ and $(q_j, \mathcal{N}_a^{q_j})$ are defined as follows.

$$\alpha(p_i, \mathcal{N}_a^{p_i}; q_j, \mathcal{N}_a^{q_j}) \\ = \left(1 - \left|(d_i(p_i, \mathcal{N}_a^{p_i}) - d_j(q_j, \mathcal{N}_b^{q_j}))/\max_{i,j}\{d_i(p_i, \mathcal{N}_a^{p_i}), d_j(q_j, \mathcal{N}_b^{q_j})\}\right|\right), \quad (5.8)$$

$$\beta(p_i, \mathcal{N}_a^{p_i}; q_j, \mathcal{N}_a^{q_j}) \\ = \left(1 - \left|(l_i(p_i, \mathcal{N}_a^{p_i}) - l_j(q_j, \mathcal{N}_b^{q_j}))/\max_{i,j}\{l_i(p_i, \mathcal{N}_a^{p_i}), l_j(q_j, \mathcal{N}_b^{q_j})\}\right|\right). \quad (5.9)$$

The second constraint, spatial smoothness, is measured by the distance between p_i and $\mathcal{N}_a^{p_i}$.

$$\gamma(p_i, \mathcal{N}_a^{p_i}) = \left(1 - \frac{d_i(p_i, \mathcal{N}_a^{p_i})}{\max_i(d_i(p_i, \mathcal{N}_a^{p_i}))}\right), \quad (5.10)$$

where $\max_i(d_i(p_i, \mathcal{N}_a^{p_i}))$ is the longest edge of point-adjacent point pairs. Two points p_i and $\mathcal{N}_a^{p_i}$ are the most salient if $\gamma(p_i, \mathcal{N}_a^{p_i})$ is 1 and the least salient if $\gamma(p_i, \mathcal{N}_a^{p_i})$ is 0. The constraining relations are illustrated in Fig. 5.7.

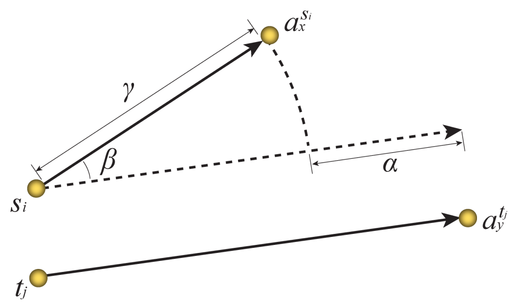

Figure 5.7: The general case of the correlation strength depends on the differences of distance and angle between point pairs. The similarity constraints α, β and the spatial smoothness constraint γ comprise the final compatibility coefficient for the relaxation labeling process.

We define a total compatibility coefficient by

$$r_{p_i q_j}(\mathcal{N}_a^{p_i}\mathcal{N}_b^{q_j}) = \alpha(p_i, \mathcal{N}_a^{p_i}; q_i, \mathcal{N}_b^{q_i}) \cdot \beta(p_i, \mathcal{N}_a^{p_i}; q_i, \mathcal{N}_b^{q_i}) \cdot \gamma(p_i, \mathcal{N}_a^{p_i}). \quad (5.11)$$

Clearly, $r_{p_i q_j}(\mathcal{N}_a^{p_i}\mathcal{N}_b^{q_j})$ ranges from 0 to 1. A high value of $r_{p_i q_j}(\mathcal{N}_a^{p_i}\mathcal{N}_b^{q_j})$ corresponds to high matching probability between $(p_i, \mathcal{N}_a^{p_i})$ and $(q_j, \mathcal{N}_b^{q_j})$, and a low value corresponds to incompatibility. The support function $q_{s_i t_j}$ in the k-th iteration is given by

$$\begin{aligned}
q^k_{p_i q_j} &= \sum_{i=1}^{I}\sum_{j=1}^{J} r_{p_i q_j}(\mathcal{N}_a^{p_i}\mathcal{N}_b^{q_j}) M^k_{\mathcal{N}_a^{p_i}\mathcal{N}_b^{q_j}} \\
&= \sum_{i=1}^{I}\sum_{j=1}^{J} \alpha(p_i,\mathcal{N}_a^{p_i}; q_i,\mathcal{N}_b^{q_i}) \cdot \beta(p_i,\mathcal{N}_a^{p_i}; q_i,\mathcal{N}_b^{q_i}) \cdot \gamma(p_i,\mathcal{N}_a^{p_i}) M^k_{\mathcal{N}_a^{p_i}\mathcal{N}_b^{q_j}}.
\end{aligned} \tag{5.12}$$

Note that $r_{p_i q_j}(\mathcal{N}_a^{p_i}\mathcal{N}_b^{q_j})$ is weighted by $m^k_{\mathcal{N}_a^{p_i}\mathcal{N}_b^{q_j}}$ because it depends on the likelihood of adjacent point pairs matching probability. Finally, $M^k_{p_i q_j}$ is updated according to

$$M^{k+1}_{p_i q_j} = M^k_{p_i q_j} q^k_{p_i q_j} / \sum_{j=1}^{J} M^k_{p_i q_j} q^k_{p_i q_j}. \tag{5.13}$$

The optimization process is as follows. If a matching probability between p_i and q_j is supported from their adjacent points $\mathcal{N}_a^{p_i}$ and $\mathcal{N}_b^{q_j}$, then the probability of being matched increases. The probability decreases if they have relatively small support from their adjacent points.

Traditionally sum of rows (or columns) in the matrix M is used as a constraint in the relaxation labeling process. In this research, we use sum of rows and columns as a two-way constraints. In order to meet these constrains, alternated row and column normalization of the matrix M is performed after each relaxation labeling updates. This procedure is known as Sinkhorn normalization and it showed that the procedure always converges to a doubly stochastic matrix (Achilles, 1993).

After pre-defined relaxation labeling iteration, the estimated matching probability is assigned to every point. To handle outliers, the points with maximum matching probability less than m_{min} (m_{min}=0.95) are labeled as outliers and match them with a dummy point. The outlier rejection scheme is performed throughout the relaxation labeling process.

5.2.4 Transformation Function

Given a finite set of correspondences between P and Q, we can proceed to estimate a plane transformation $T : \Re^3 \rightarrow \Re^3$ that may be used to map arbitrary points from one image to the other. In this study, we use thin-plate spline (TPS) model, which is commonly used for representing flexible coordinate transformations (Lee et al., 2010a), (Lee et al., 2008).

Let v_i denote the target function values at corresponding locations $p_i = (x_i, y_i, z_i)$ in the plane, with $i = 1, 2, ..., n$. We set v_i equal to x'_i, y'_i, z'_i to obtain the transformation. In 3-D interpolation problem, the TPS interpolant $f(x, y, z)$ minimizes the bending energy

$$\begin{aligned} I_f &= \iiint\limits_{\Re^3} \left[\left(\frac{\partial^2 f}{\partial x^2}\right)^2 + \left(\frac{\partial^2 f}{\partial y^2}\right)^2 + \left(\frac{\partial^2 f}{\partial z^2}\right)^2 \right. \\ & \left. +2(\left(\frac{\partial^2 f}{\partial x \partial y}\right)^2 + \left(\frac{\partial^2 f}{\partial x \partial z}\right)^2 + \left(\frac{\partial^2 f}{\partial y \partial z}\right)^2) \right] dxdydz \end{aligned} \tag{5.14}$$

and the interpolant form is

$$f(x, y, z) = a_1 + a_x x + a_y y + a_z z + \sum_{i=1}^{n} w_i U(\|(x_i, y_i, z_i) - (x, y, z)\|). \tag{5.15}$$

where a_1, a_x, a_y, a_z are the coefficients and w_i's are the weighting factors. The kernel function $U(r)$ is defined by $U(r) = r^3 \log r^3$. In order for $f(x, y, z)$ to have square integrable second derivatives, we require the boundary condition $\sum\limits_{i=1}^{n} w_i = 0$ and $\sum\limits_{i=1}^{n} w_i x_i = \sum\limits_{i=1}^{n} w_i y_i = \sum\limits_{i=1}^{n} w_i z_i$ =0. A special characteristic of the thin-plate spline is that the resulting transformation is always decomposed into a global transformation and a local non-affine warping component. The first four terms describe global affine transform and the remaining terms describe non-linear (non-global) transformation. Together with the interpolation conditions, $f(x_i, y_i, z_i) = v_i$, this yields a linear system for the TPS coefficients:

$$\begin{pmatrix} K & P \\ P^T & 0 \end{pmatrix} \begin{pmatrix} W \\ A \end{pmatrix} = \begin{pmatrix} V \\ 0 \end{pmatrix}, \tag{5.16}$$

where $K = \begin{bmatrix} 0 & U(r_{12}) & \cdots & U(r_{1n}) \\ U(r_{21}) & 0 & \cdots & U(r_{2n}) \\ \cdots & \cdots & \cdots & \cdots \\ U(r_{n1}) & U(r_{n2}) & \cdots & 0 \end{bmatrix}$ and $P = \begin{bmatrix} 1 & x_1 & y_1 & z_1 \\ 1 & x_2 & y_2 & z_1 \\ \cdots & \cdots & \cdots & \cdots \\ 1 & x_n & y_n & z_1 \end{bmatrix}$.

Here, $r_{ij} = ||P_i - P_j||$ is the Euclidean distance between points P_i and P_j. W and A are column vectors formed from $W = (w_1, w_2, ..., w_n)^T$ and $A = (a_1, a_x, a_y, a_z)^T$, respectively. $V = (v_1, v_2, ..., v_n)$ is any n-vector. The matrix $\begin{pmatrix} K & P \\ P^T & 0 \end{pmatrix}$ is nonsingluar and it is invertable.

Thus we can determine the coefficients W and A by multiplication of matrices $\begin{pmatrix} K & P \\ P^T & 0 \end{pmatrix}^{-1}$ and $\begin{pmatrix} V \\ 0 \end{pmatrix}$. The weighting factors and coefficients W and A determine TPS interpolants $f(x, y, z) = [f_x(x, y, z), f_y(x, y, z), f_z(x, y, z)]$ is a vector-valued, and this maps each point (x_i, y_i, z_i) to its correspondence (x_i', y_i', z_i'), the x, y, z coordinates of the transformation. The resulting function $f(x, y, z) = [f_x(x, y, z), f_y(x, y, z), f_z(x, y, z)]$ maps each point (x_i, y_i, z_i) to its correspondence point (x_i', y_i', z_i'). It provides a continuous displacement field between O_1 and O_2. Finally, the nonlinear Lagrangian strain tensor component of the uniaxial loading configuration e_{zz} is determined as follows:

$$\begin{aligned} e_{zz} &= \tfrac{\partial f_z(x,y,z)}{\partial z} \\ &+\tfrac{1}{2}\left[\left(\tfrac{\partial f_x(x,y,z)}{\partial z}\right)^3 + \left(\tfrac{\partial f_y(x,y,z)}{\partial z}\right)^3 + \left(\tfrac{\partial f_z(x,y,z)}{\partial z}\right)^3\right]. \end{aligned} \tag{5.17}$$

From Eq. (5.17), we can estimate the final strain information.

5.2.5 Validation and Performance Evaluation

In order to access the performance of the proposed algorithm, we have compared our matching results with the state-of-the-art algorithms such as SC, TPS-RPM, RPM-LNS, and CPD method. In the experiments, we set 300 as the number of labeling updates and the alternate iteration with TPS transformation as 10.

Simulations Based on Synthetic Data

We have tested our proposed method and the state-of-the-art algorithms with respect to different degrees of deformation, noise, outliers, rotation and occlusion ratio on synthetic data set. The data set consists of two different shape models. The first model consists of 96 points to represent a fish shape. The second model is a more complex pattern consisting of 108 points to represent a Chinese character ("blessing").

In each test, one of the distortions is applied to a model set to create a target set. Fig. 5.8 to Fig. 5.13 show examples of synthesized data sets (Rangarajan et al., 1999). A total of 100 data sets is generated at each distortion level. The matching performance of each algorithm is compared by the mean and standard deviation of the registration error of 100 trials in each distortion level. We use root mean square (RMS) error for the registration error metric. The statistical results, error means and standard deviations for each setting, are shown in from Fig. 5.14 to Fig. 5.18.

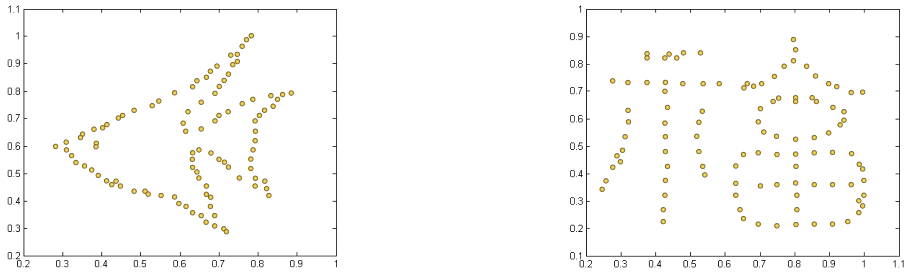

(a) (b)

Figure 5.8: Synthesized original data sets for statistical tests. (a) fish shape. (b) Chinese character shape.

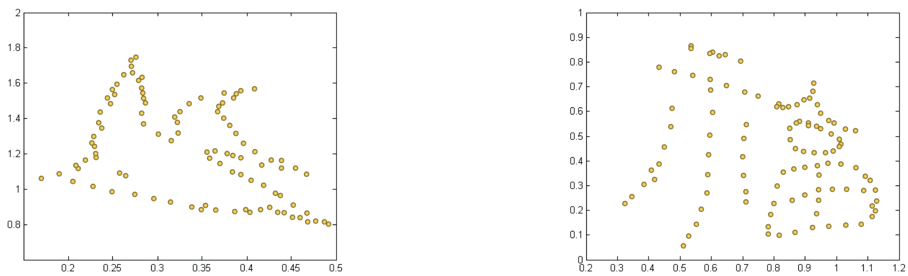

(a) (b)

Figure 5.9: Synthesized deformation data sets for statistical tests. (a) fish shape. (b) Chinese character shape.

In the deformation test results, Figs. 5.14(a) and 5.14(b), five algorithms achieve similar matching performance in both fish and character shape at low deformation ratio. However, as the degree of deformation increases, we observe that TPRL shows the robustness to large deformation compared with other algorithms. The degree of deformation such as 0, 0.035, 0.05, 0.065, and 0.08 indicates the deformation ratio. This measures the percentage of the deformation degree from the original image. The higher ratio shows the higher deformation degree. The small ratio shows the lower deformation degree.

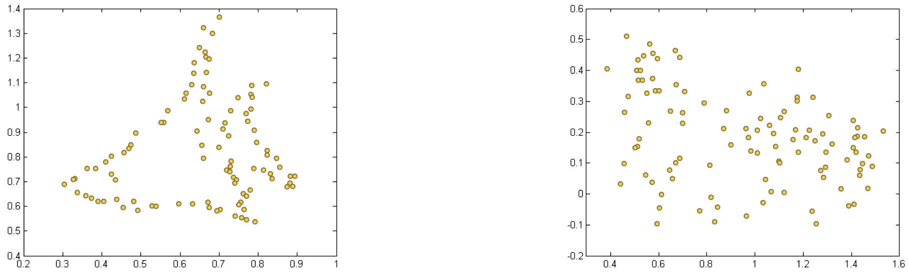

(a) (b)

Figure 5.10: Synthesized noise data sets for statistical tests. (a) fish shape. (b) Chinese character shape.

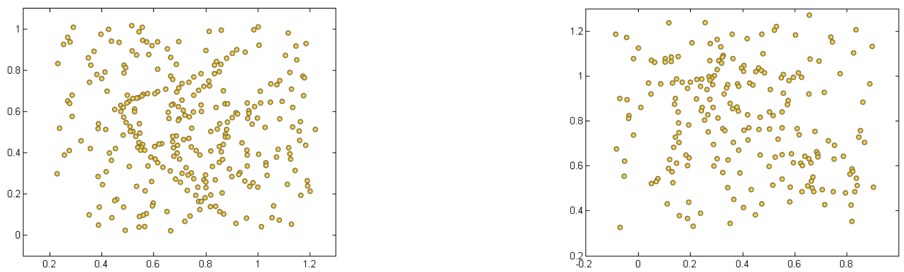

(a) (b)

Figure 5.11: Synthesized outlier data sets for statistical tests. (a) fish shape. (b) Chinese character shape.

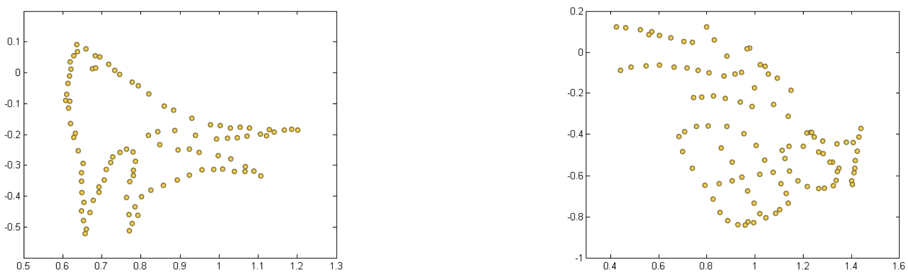

(a) (b)

Figure 5.12: Synthesized rotation data sets for statistical tests. (a) fish shape. (b) Chinese character shape.

The presence of noise makes the point's location ambiguous. Therefore, this type of data is more challenging than the deformation data. The noise test results of Figs. 5.15(a) and 5.15(b) show that all algorithms are affected by this type of data distortion. However, we notice that TPRL compensates the location ambiguity and finds more accurate correspondences than the other four.

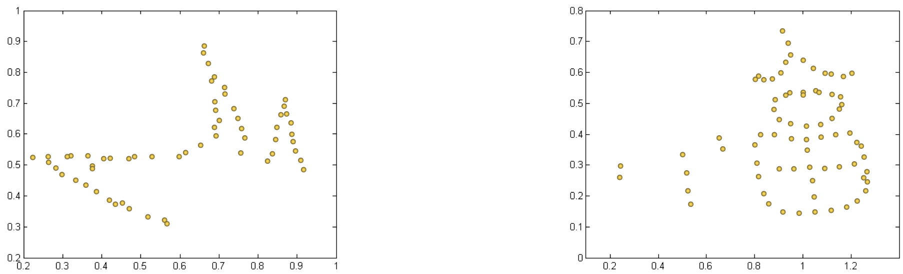

(a) (b)

Figure 5.13: Synthesized occlusion data sets for statistical tests. (a) fish shape. (b) Chinese character shape.

In addition to the deformation and noise test, present outliers further complicate the point matching problem. To evaluate the performance of our method with outliers, we added maximum of 405 outliers to the target set. From the results of Figs. 5.16(a) and 5.16(b) we note that SC and CPD in both shapes and RPM-LNS in a character shape are easily confused by outliers and start to fail once the outlier level becomes relatively high. The TPS-RPM are not affected by outliers as much, but the error is still higher than TPRL. The TPRL is very robust regardless of the outlier level.

In Figs. 5.17(a) and 5.17(b) we evaluate the influence of rotation. From this result, we notice that the applied transformation (rotation) does not affect the performance of SC, RPM-LNS and TPRL. All error curves except TPS-RPM and CPD are relatively constant. Note that until 30 degrees of rotation, the errors of TPS-RPM and CPD are lower than SC and RPM-LNS. But from 60 degree of rotation, TPS-RPM and CPD deteriorate quickly. The TPRL is rotation invariant and consistently outperforms four other algorithms in all degrees of rotations.

Occlusion is also an important degradation in real applications. We use six occlusion levels to test the five algorithms. As shown in Figs. 5.18(a) and 5.18(b), the RMS error of TPS-RPM is the largest compared to the other four algorithms. The TPRL achieves the best result in both fish and character shapes.

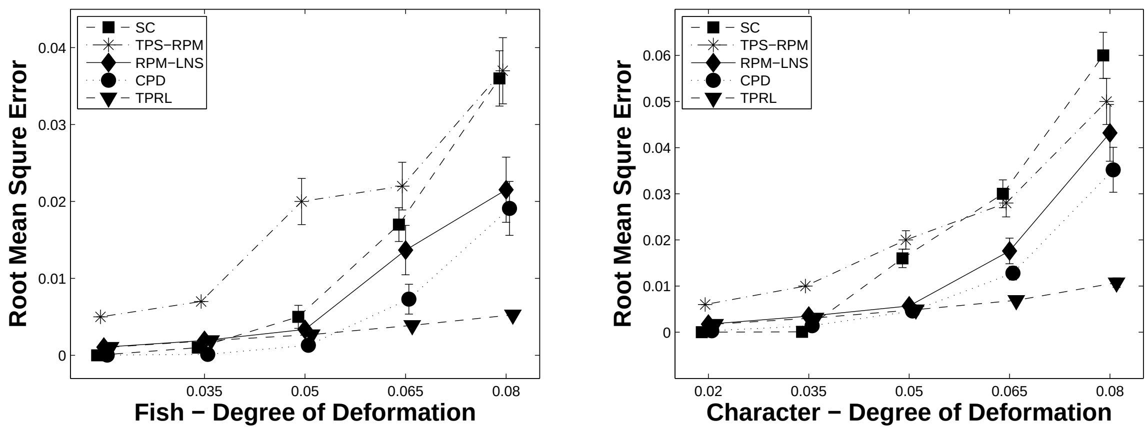

(a) (b)

Figure 5.14: Comparison of the matching performance of TPRL (▼) with shape context (■), TPS-RPM (∗), RPM-LNS (⧫), and CPD (●). (a) Fish shape deformation test. (b) Character shape deformation test.

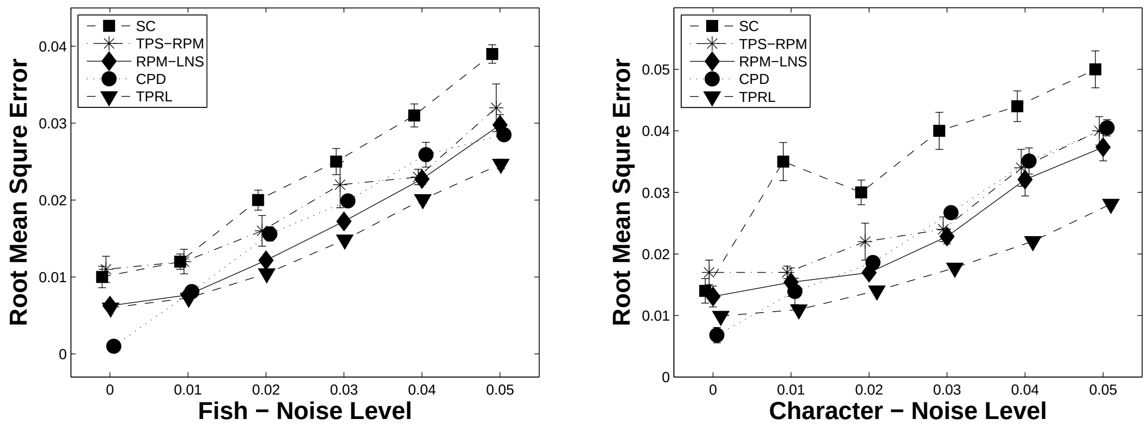

(a) (b)

Figure 5.15: Comparison of the matching performance of TPRL (▼) with shape context (■), TPS-RPM (∗), RPM-LNS (⧫), and CPD (●). (a) Fish shape noise test. (b) Character shape noise test.

Simulations Based on Real World Data

We also conducted experiments on real world data. For this experiment, we have used the Carnegie Mellon University (CMU) hotel sequence available. The database consists of 101 frames of a moving sequence of a toy hotel. We obtained 11 frames as shown in Figs. from 5.19(a) to 5.19(j). In total, 100 points were manually selected from each frame and matched all images spaced by 10, 20, 30, 40, 50, 60, 70, 80, 90, 100 frames. The experiments were

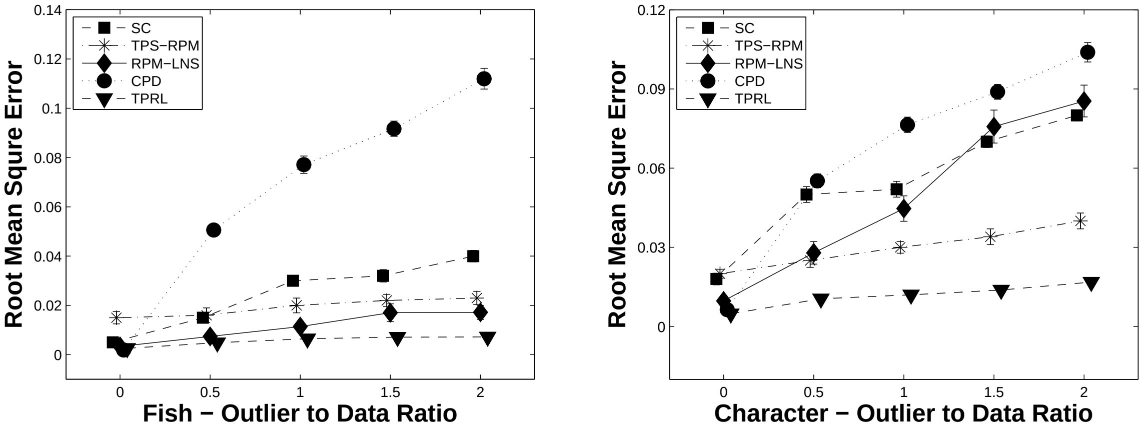

(a) (b)

Figure 5.16: Comparison of the matching performance of TPRL (▼) with shape context (■), TPS-RPM ($*$), RPM-LNS (⧫), and CPD (●). (a) Fish shape outlier test. (b) Character shape outlier test.

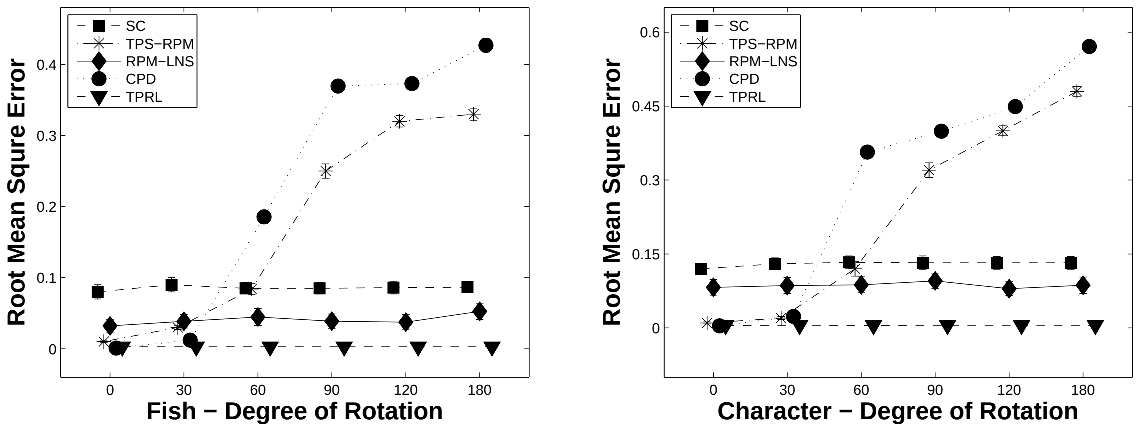

(a) (b)

Figure 5.17: Comparison of the matching performance of TPRL (▼) with shape context (■), TPS-RPM ($*$), RPM-LNS (⧫), and CPD (●). (a) Fish shape rotation test. (b) Character shape rotation test.

conducted under four different occlusion ratios: 0.0 (100×100), 0.1 (90×100), 0.2 (80×100), and 0.3 (70×100).

Figs. 5.20(a) to 5.20(d) show the results for these experiments. We note that without occlusion, Fig. 5.20(a), five algorithms achieve similar matching performance until 30 frames of separation. However, as the frame separation increases, we observe that TPRL shows the robustness compared to other algorithms. The increased mean RMS error from 10 to 100 frames

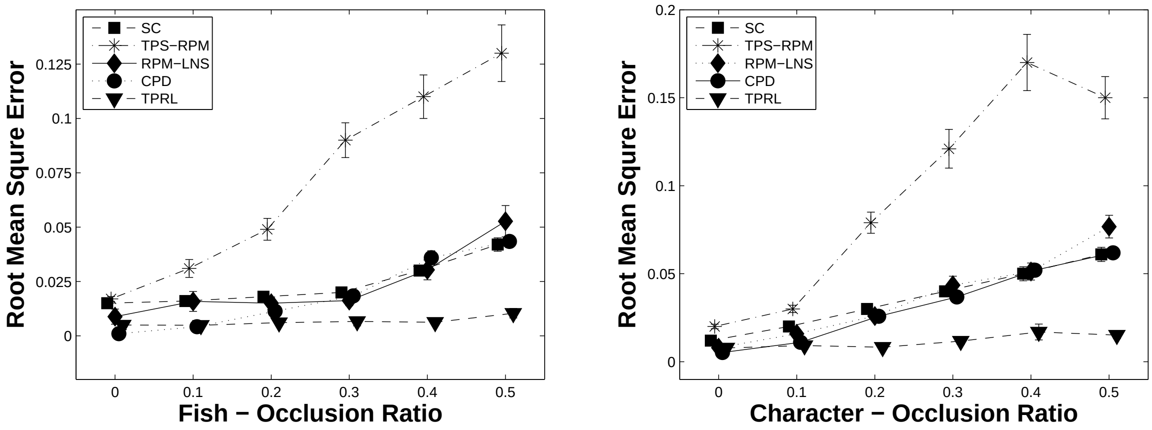

(a) (b)

Figure 5.18: Comparison of the matching performance of TPRL (▼) with shape context (■), TPS-RPM (∗), RPM-LNS (♦), and CPD (●). (a) Fish shape occlusion test. (b) Character shape occlusion test.

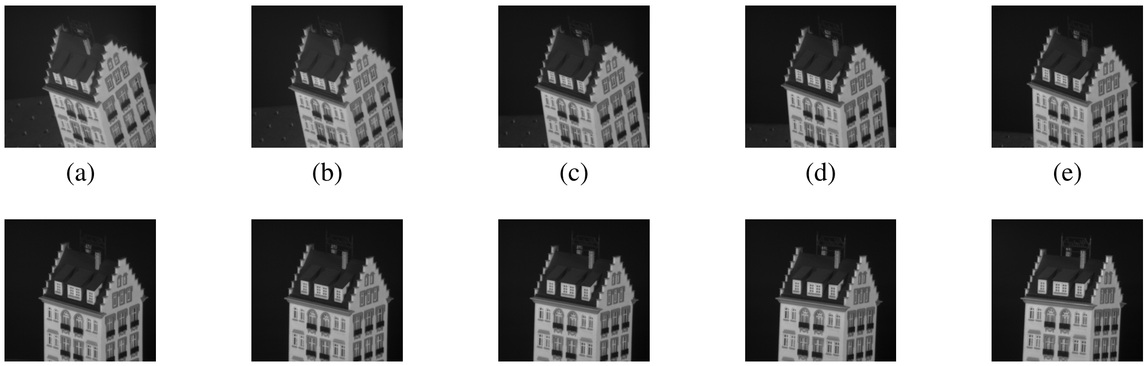

(a) (b) (c) (d) (e)

(f) (g) (h) (i) (j)

Figure 5.19: Sequence images of toy hotel. (a) Frames 0, (b) Frames 10, (c) Frames 20, (d) Frames 30, (e) Frames 40, (f) Frames 50, (g) Frames 60, (h) Frames 70, (i) Frames 80, (j) Frames 90, (j) Frames 100.

separation is 0.001 mm compared to 0.049 mm in SC, 0.027 mm in TPS-RPM, 0.021 mm in RPM-LNS, and 0.025 mm in CPD. Figs. 5.20(b) to Fig. 5.20(d) show the results with occlusion. With 0.3 occlusion ratio, the increased mean RMS error is 0.005 mm from 10 to 100 frames of separation, compared to 0.05 mm in RPM-LNS, the second smallest change among the algorithms.

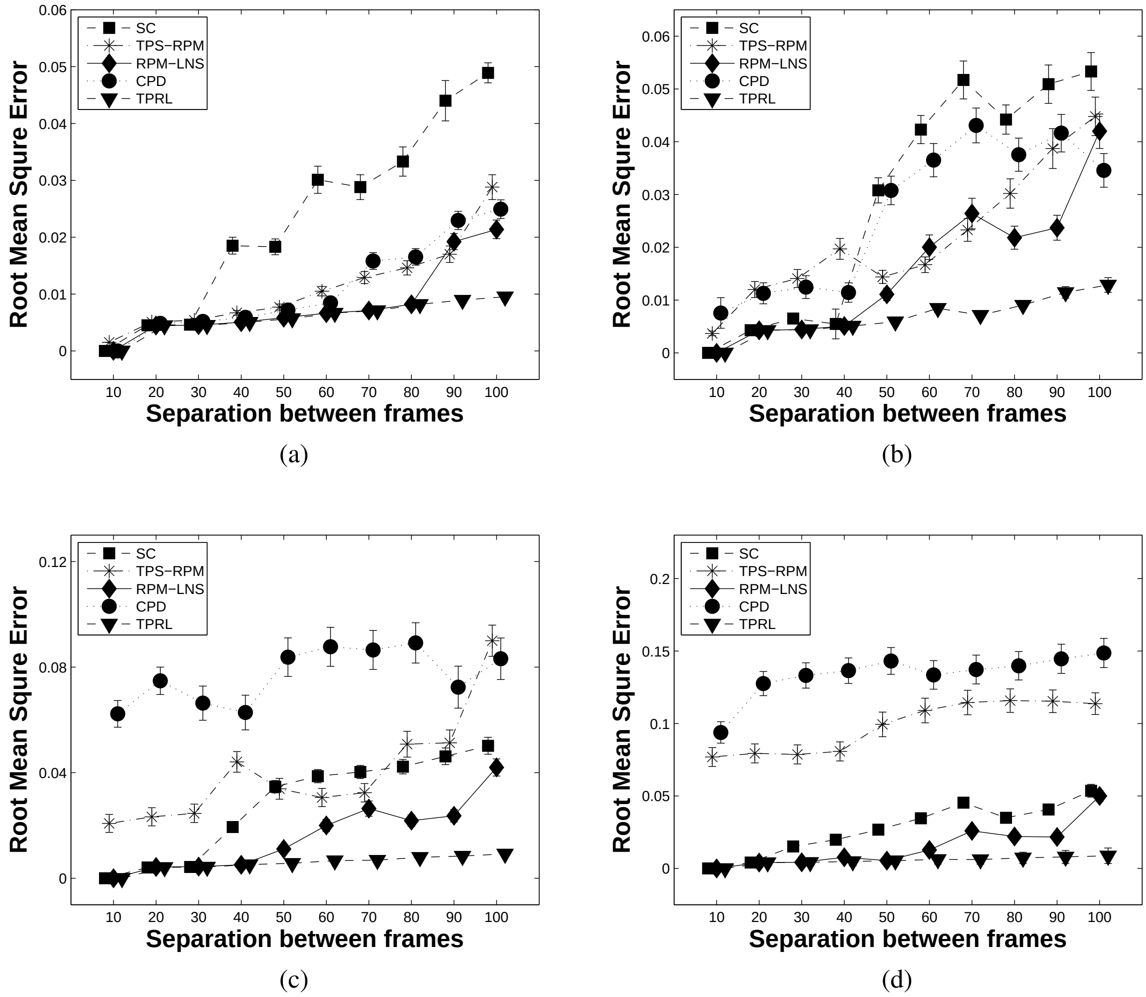

Figure 5.20: Comparison of the matching performance of TPRL (▼) with shape context (■), TPS-RPM (∗), RPM-LNS (♦), and CPD (●) in the hotel sequence for increasing frame separation and different occlusion ratio [(a) 0.0, (b) 0.1, (c) 0.2, (d) 0.3]. Error bars correspond to the standard deviation of each pair's RMS error.

Simulations Based on Large Data

We also tested the TPRL performance under a larger data set as shown in Figs. 5.21(a) and 5.21(b). From the image, 1000 points were extracted by curvature scale space corner detector (He and Yung, 2008). After a model set was chosen, we applied a randomly generated non-rigid transformation to warp it and added 1000 to 3000 outliers. The TPRL performed the best with 0.35 ± 0.22 mm, 0.38 ± 0.24 mm, and 0.39 ± 0.25 mm RMS errors for the 1000×2000, 1000×3000, and 1000×4000 size point matching, respectively. The CPD method gave the second highest matching performance with 0.61 ± 0.51 mm, 0.66 ± 0.56 mm, and 0.67 ± 0.56 mm

RMS errors in the same scenario.

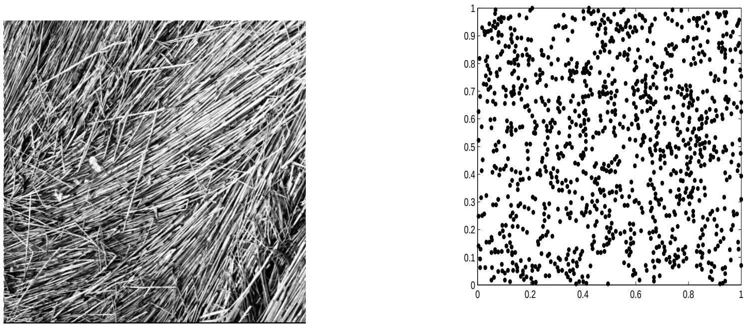

(a) (b)

Figure 5.21: Robustness test on large data set. (a) A straw image and (b) 1000 points extracted from the straw image.

Processing Times

In order to compare algorithms, it is necessary to analyze the processing time of each algorithm. Assume that both model set and target set have points. The algorithms are based on the NP-hard problem and have similar computational complexity of $O(N^2)$ for matching in $\Re^2$ and $O(N^3)$ for matching in $\Re^3$. Among the compared algorithms, the CPD method performs with the fastest registration time under a large distortion of the data set. The TPRL algorithm takes a slightly longer time to compute compared to the CPD method. For a 105 $\times$ 105 point matching, the TPRL algorithm takes about 1.69 seconds and the CPD method takes about 1.08 seconds on a desktop PC with Core 2 Duo CPU with 2.13GHz and 2GB RAM.

5.3 Young's Modulus Estimation from Stress and Strain

To determine the Young's modulus of the contacted object, the strain component e_{zz} are averaged to yield the average strain $\bar{e}_{zz}$. Given the applied normal stress $\hat{P}_{zz}$, the Young's modulus E of the object is then determined from the following equation,

$$E = \hat{P}_{zz}/\bar{e}_{zz}. \tag{5.18}$$

The proposed Young's modulus estimation method is validated in the next section.

5.4 Experimental Results

To validate the target hardness estimation method based on the tactile data, Versaflex CL2000X and CL2003X (GLS, McHenry, Illinois) soft polymers of Young's moduli 103 kPa and 62 kPa have been used. The soft polymer was spherical shape with 3 mm radius. In this experiment, the TSIS compressed the polymer samples while slowly increasing the compression ratio. At 0.7 N and 1.2 N applied forces, two tactile data have been captured. The obtained tactile data were then reconstructed to 3-D, and control points were extracted from the surface of 3-D reconstructed tactile data. The correspondence and transformation function between control points were estimated using the proposed TPRL algorithm described in Section 5.2.1.

Fig. 5.22(a) represents 200 control points distributions extracted from each of CL2000X soft polymer tactile data in Fig. 5.5. The point matching result using the proposed TPRL algorithm is represented in Fig. 5.22(b). Fig. 5.23 represents the experimental result. The lines represent theoretical CL2000X and CL2003X modulus values from the manufacturer, and the circles and crosses represent the measured values from the TSIS. The errors of the estimated moduli were within 4.23% relative error for CL2000X and 5.38% relative error for CL2003X.

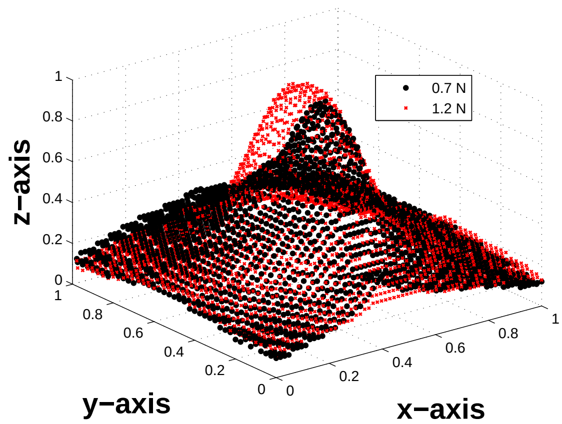

(a)

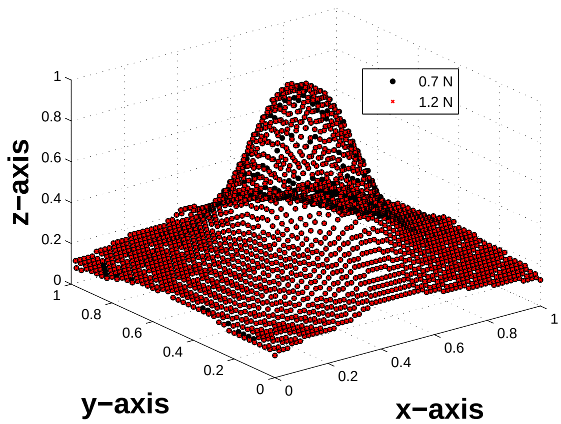

(b)

Figure 5.22: Control points extracted from two tactile data obtained under different loading forces on the same object. (a) Before point matching, (b) After point matching.

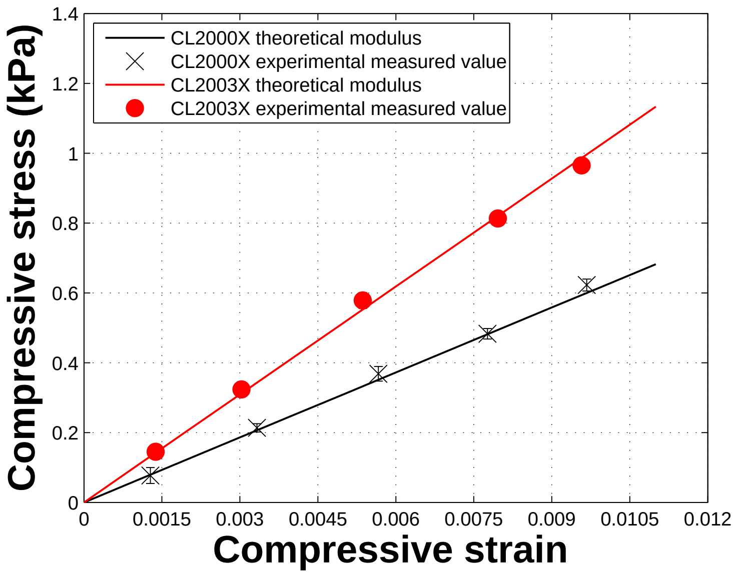

Figure 5.23: The hardness estimation results of soft polymers, CL2000X and CL2003X.

5.5 Discussions

In this chapter, the tactile data processing algorithm capable of estimating the hardness of the touched object via direct contact are developed and experimentally evaluated. The hardness of the contacted object is estimated using the tactile data obtained by the TSIS. In order to obtain the hardness of the contacted object, a new non-rigid pattern matching algorithm called "TPRL" is developed. The performance of the target hardness estimation method is experimentally verified using the soft polymers. The results show that when using the TSIS, the hardness of the touched object can be estimated within 5.38% relative error.

The measured object must be smaller than the area of the TSIS sensing probe. If we are measuring the elasticity of a surface object, the contact area must be smaller than the TSIS sensing probe area. However, if we measure a sub-surface object such as tumor, the TSIS sensing probe area can be smaller than the contact tissue surface, as long as the inclusion is smaller than the probe area. In this case, the contact area, C, is the area of the sensing probe with the known value. Thus, even if the hidden tumor exists in a variety of sizes and shapes, the contact area, C, is always a constant, which is the sensing probe area. One possible application of the TSIS is the early detection of breast cancer. The common breast tumor size is approximately

20 mm or smaller in stages 0 and I (Krouskop et al., 1998). In stage II, it is approximately 20 to 50 mm (Krouskop et al., 1998). To detect the 50 mm breast tumor, the sensing probe should be bigger than 50 mm.

Generally, the background light disturbance and drifting of the light source are issues for the tactile sensor that operates based on the detection of light illumination (Katz, 2002). If the background light is too bright compared to the light of the tactile sensor, it causes measurement errors of the TSIS. To prevent this, we use the TSIS in a relatively dark room, which minimizes the background light disturbance. The drifting of light occurs if light sources of the TSIS are positioned incorrectly and the camera captures the spurious light. In this case, the drifted light is shown as noise in the tactile data. To prevent this, precise positioning and directionality of the light source are required. We carefully positioned and calibrated four light sources with acceptance angles. These two methods prevented the light disturbance and drifting of the light source issues during the preliminary experiments. In the future work, we will also consider using the image segmentation techniques. More specifically, Canny edge detection technique can be used to extract the boundary of the desired light scattering area in the tactile data and remove the noise (Canny, 1986).

Typically, in the LED operation, approximately 20% input power is converted to light and 80% to heat (Rico-Secades et al., 2005). Heat at the junction of the LED affects the overall performance of the LED in terms of light output and spectrum. The amount of light emitted by the LED decreases as the junction temperature rises. Thus, LED luminaries require a thermal management system for LED cooling, since most of the energy for the LED is converted to heat rather than light. Without an appropriate thermal management system, the generated heat can degrade the intensity of the LED and finally affect the calibration result of the TSIS. In the current TSIS design, the LED is directly connected to the power source, resulting in the intensity drift caused by the temperature effect and the variation of the resistance in the power source. In our experiments, the TSIS takes approximately 20 seconds to take a tactile data of the touched object. Thus, the LED intensity drift caused by the temperature effect is not large. In the next TSIS design, we will consider a thermal management system such as heat sinks to release heat from the LED. The flip-chip package type LED will also be considered to reduce the thermal resistance of the LED. To prevent the variation of the resistance in the power source, we will also consider the constant current LED drive circuit.

Eq. (5.2) is material-dependent. Depending upon the material, the relationship could be linear or nonlinear. In this research, we assumed that the touched object is homogeneous and isotropic. In this case, the relationship curve between the normal force and the summation of pixel values in tactile data is linear. Thus, the applied force is estimated from the summation of pixel values in tactile data using the normal force versus the summation of pixel values table, which is previously obtained by the calibration. Then the applied stress, which is the force per unit area, is obtained by dividing the applied force by the contact area. We have verified this approach in Section 5.4 for the homogeneous and isotropic material. If the touched object is inhomogeneous and anisotropic, Eq. (5.2) will not be valid. We will have to re-derive Eq. (5.2) for the inhomogeneous and anisotropic material case.

The measurement range of the TSIS is controlled by the hardness of the TSIS sensing probe. This is determined by how we mix two components of PDMS, the viscous fluid silicone (part A) and the catalyst (part B). The viscous fluid silicone is hardened by the catalyst. If the amount of catalyst increases, the hardness of the PDMS increases. If the amount of catalyst decreases, the hardness of the PDMS decreases. In this research, the measurement range of the TSIS designed for the soft polymer hardness estimation is from a normal force of 0 to 2500 mN. In future work, we will investigate the different measurement ranges of the TSIS depending upon the different hardness of the TSIS sensing probe.

CHAPTER 6

TISSUE INCLUSION PARAMETER ESTIMATION BY INDIRECT CONTACT

The mechanical properties of tissue inclusion such as hardness and its geometry are very important in detecting and characterizing the severity of the tumor. In this chapter, we devise a methodology for estimating three parameters of the tissue inclusion: size, depth, and hardness. The estimated parameters are extracted from the tactile data obtained at the tissue surface using the TSIS. Two different estimation approaches are proposed in this chapter. The first approach is to estimate the relative parameters of tissue inclusion. Using the salient features of the captured tactile data, we estimate the relative inclusion parameters such as size, depth, and hardness. The second approach is to estimate the absolute parameters of tissue inclusion. The estimation method consists of the forward algorithm and inversion algorithm. The forward algorithm is designed to comprehensively predict the tactile data based on the parameters of the inclusion in the soft tissue. This algorithm is used to develop the inversion algorithm that can be used to extract the size, depth, and hardness of an inclusion. The proposed algorithms are then validated by the realistic tissue phantoms with stiff inclusions.

6.1 Problem Formulation

To estimate tissue inclusion's parameters, we consider the following idealized tissue model in Fig. 6.1. The assumptions used in the idealized tissue model are as follows (Wellman et al., 2001b).

1) Most breast tumors are found in the upper outer quadrant of the breast where the tissue is relatively thin and flat. Therefore, in our breast tissue model, the breast tissue is approximated as a slab of material of constant thickness that is fixed to a flat, incompressible chest wall.

2) The tissue inclusion is assumed to be spherical and stiffer than the surrounding tissue.

3) We assume that both breast tissue and tissue inclusion are linear and isotropic.

4) The interaction between the TSIS sensing probe and breast tissue is assumed to be frictionless.

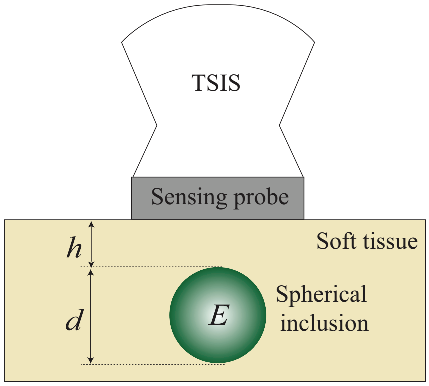

Figure 6.1: The cross-section of an idealized breast tissue model for estimating inclusion parameters. The tissue inclusion has three parameters – diameter d, depth h, and hardness E.

In the following section, we devise two methodologies for estimating three parameters of the tissue inclusion (size d, depth h, and hardness E): the relative tissue inclusion parameter estimation method and the absolute tissue inclusion parameter estimation method. The estimation of these parameters was performed using tactile data obtained by the TSIS at the tissue surface.

6.2 Relative Tissue Inclusion Parameter Estimation

6.2.1 Relative Size Estimation Method

The relative tissue inclusion size has been estimated using tactile data. We estimate the diameter of an inclusion as its size. In the TSIS operation, as the size of an inclusion increases, the light scattering increases as the effect of bigger inclusion causes more change in the optical sensing probe deformation. Thus, we measured the light scattering area of tactile data to estimate the inclusion size. Let $I(x, y)$ be the individual pixel value of tactile data. Then the light scattering area A captured in the tactile data can be calculated by counting the number of pixels bigger than the specific value of k;

$$\mathrm{A} = \text{number of pixel values,} \tag{6.1}$$

that is the number of $I(x, y) > k$. k is the pixel threshold value and we set it as 5. The area of Eq. (6.1) is the pixel area in the tactile data. To transform the pixel area to the real area, the scale factor is used. We used the scale factor between the actual area and the tactile data pixel area as $(6.79 \times 10^{-3})^2\ mm^2$ per pixel area. We obtained this ratio by the calibration. Then a relative size d of a tissue inclusion can be found as follows.

$$d = 2\sqrt{(6.79 \times 10^{-3})^2 \times A/\pi}. \tag{6.2}$$

The unit of the relative inclusion size is millimeters. In this research, we assume that a tissue inclusion is spherical and there is only one inclusion in the tissue. Also, we assume that there is no noise in the tactile data. In addition, when we calculate the size of tissue inclusion, we did not consider other two parameters, depth and Young's modulus.

6.2.2 Relative Size Estimation Experimental Results

We demonstrate the capability of the proposed relative size estimation method. For this experiment, the realistic tissue phantoms with embedded hard inclusions (simulated tumor) have been manufactured (CIRS Inc., VA). The phantom includes three hard inclusions with sizes, 2, 8, and 14 mm. Each inclusion was placed 5 mm below the surface of the phantom (Lee et al., 2011). The phantom was made of a silicone composite having a Young's modulus of approximately 5 kPa. The inclusion was made using another silicone composite, the stiffness of which was higher than the surrounding tissue phantom. The Young's modulus of each inclusion was 120 kPa, which is for fibrous tissue at 5% pre-compression with loading frequency of 4.0 Hz (Krouskop et al., 1998). The schematic of the size phantom is shown in Fig. 6.2 and the manufactured size phantom is shown in Fig. 6.3. To obtain the tactile data, first we placed the phantom in the desk. We then placed the TSIS onto the phantom surface where the tissue inclusion was embedded and pressed it to obtain the tactile data. To compare the tactile data between three different tissue inclusions, we applied the same loading forces of the TSIS on three different tissue inclusions. For each tissue inclusion case, we obtained 15 tactile data. The relative size of an inclusion has been estimated using Eq. (6.2) and averaged. Fig. 6.4 represents the sample tactile data of each inclusion.

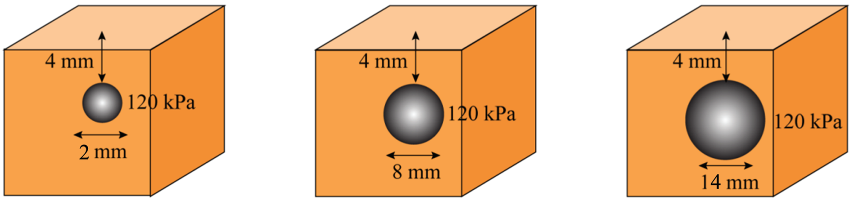

Figure 6.2: The schematic of the size phantom.

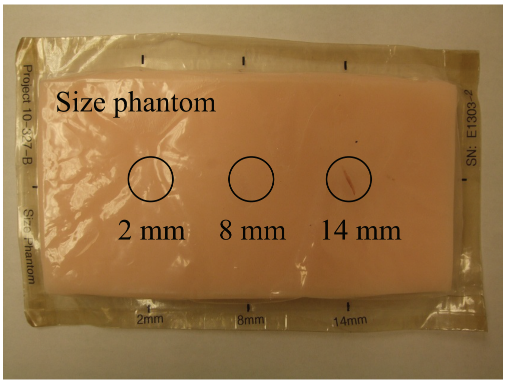

Figure 6.3: The manufactured size phantom.

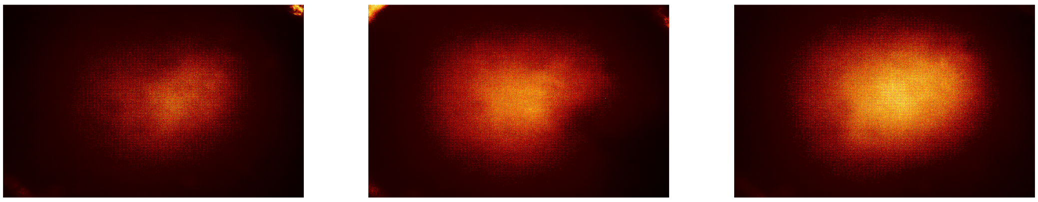

(a) (b) (c)

Figure 6.4: The tactile data of three inclusions embedded in the size phantom. (a) 2 mm size inclusion, (b) 8 mm size inclusion, (c) 14 mm size inclusion.

The relative size estimation results are shown in Fig. 6.5. The plot shows that the 14 mm size case had the highest mean size of 8.77 mm and the most variation, with a standard deviation of 1.24 mm. Conversely, the 2 mm size case had the lowest mean size of 1.67 mm, and the least variation, with a standard deviation of 0.48 mm. Because we estimated the relative value, the comparison ratio of each estimated size is also important. The ratio of real size of inclusions was approximately 1 : 4 : 7. The estimated ratio of relative size was approximately 1 : 3.86 : 5.26. This corresponds to 3.5% and 24.9% relative error. The error is larger for larger size inclusion.

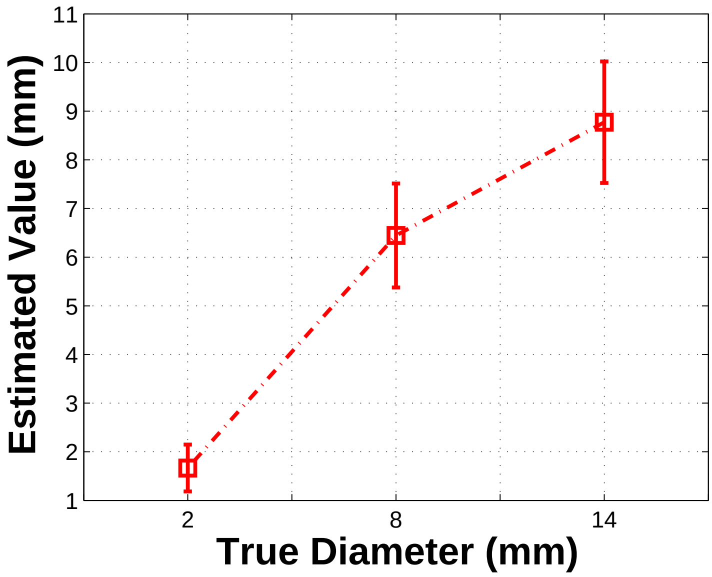

Figure 6.5: Error bar chart of estimated relative diameter of each inclusion.

6.2.3 Relative Depth Estimation Method

As the depth of inclusion increases, the light scattering due to the waveguide deformation decreases as the effect of an inclusion becomes reduced. Because we have assumed that the inclusion is spherical, the pixel values of the tactile data distribute in a bell shape, where the pixel intensity is the highest at the centroid of the pixel values of tactile data and decreases with increasing distance from the centroid. Thus, we used a centroid pixel value of tactile data to estimate a relative inclusion depth. To obtain equations for locating centroids of the tactile data, first we find the moment of a force as referred to in Fig. 6.6.

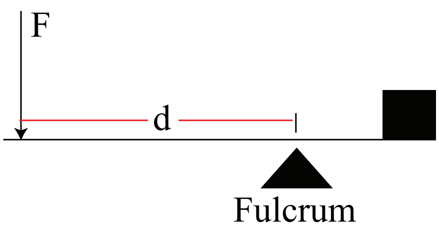

Figure 6.6: Definition of moment of a force.

The moment M of a force F about some fixed fulcrum is defined as (Kotoulas and Andreadis, 2007)

$$M = Fd, \tag{6.3}$$

where d is the distance from the fulcrum to the line of action of the force F. Then, assume a system n point masses situated along a horizontal line, as shown in Fig. 6.7.

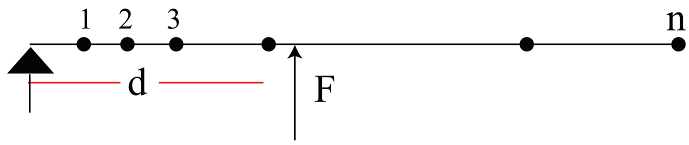

Figure 6.7: n **point masses situated along a horizontal line.**

The expression of the moment M is as follows.

$$M_1 = w_1x_1 + w_2x_2 + w_3x_3 + \cdots w_nx_n, \tag{6.4}$$

$$Fd = w_1x_1 + w_2x_2 + w_3x_3 + \cdots w_nx_n. \tag{6.5}$$

Thus the distance from the fulcrum to the line of action of the force F is

$$d = \frac{w_1x_1 + w_2x_2 + w_3x_3 + \cdots w_nx_n}{w_1 + w_2 + w_3 + \cdots w_n}. \tag{6.6}$$

Now, this concept is extended to the case of centroids of x-and y-coordinates of the tactile data. Since the tactile data is 2-D, the centroid of tactile data, (X_c, Y_c), are calculated by (Kotoulas and Andreadis, 2007), (Johnson, 2007)

$$X_c = \frac{\sum\limits_x \sum\limits_y I(x,y)xdxdy}{\sum\limits_x \sum\limits_y I(x,y)dxdy}, \tag{6.7}$$

$$Y_c = \frac{\sum\limits_x \sum\limits_y I(x,y)ydxdy}{\sum\limits_x \sum\limits_y I(x,y)dxdy}. \tag{6.8}$$

Then a relative depth of a tissue inclusion h can be calculated as below.

$$h = I(X_c, Y_c). \tag{6.9}$$

Because the calculated depth is the pixel distance, using the scale fact $6.79 \times 10^{-3}\ mm^2$ per pixel distance, we transform the pixel distance to the actual distance. Same as the relative inclusion size case, the unit of the relative inclusion depth is millimeters. As with the size estimation case, we assume that a tissue inclusion is spherical and there is only one inclusion in the tissue. Also, we assume that there is no noise in the tactile data. In addition, when we calculate the depth of tissue inclusion, we do not consider the other two parameters, size and hardness.

6.2.4 Relative Depth Estimation Experimental Results

The depth tissue phantom has three inclusions with different depths: 4, 8, and 12 mm. The size of all inclusion was 7 mm and their Young's modulus was 100 kPa, which is about the invasive ductal carcinoma hardness (Krouskop et al., 1998). The schematic of the depth phantom is shown in Fig. 6.8 and the manufactured depth phantom is shown in Fig. 6.9. Consistent with the size phantom experiment case, we obtained 15 tactile data of each inclusion using the same experimental steps in subsection 6.2.2. Then, the relative depth of an inclusion was estimated using Eq. (6.9) and averaged. Fig. 6.10 represents the sample tactile data of each inclusion.

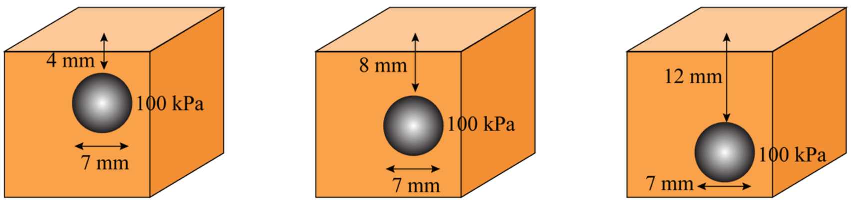

Figure 6.8: The schematic of the depth phantom.

The depth estimation result is shown in Fig. 6.11. The plot shows that the 4 mm depth case had the highest mean depth of 0.59 mm and the least variation, with a standard deviation of 0.03 mm, whereas the 12 mm depth case had the lowest mean depth of 0.34 mm and the most variation with a standard deviation of 0.08 mm. The ratio of the real depth of inclusions was approximately 1 : 1.5 : 3. The estimated relative depth ratio was approximately 1 : 0.74 : 0.57. This is a relative error of 50.7% and 81.0% for the latter two inclusion depths with respect to

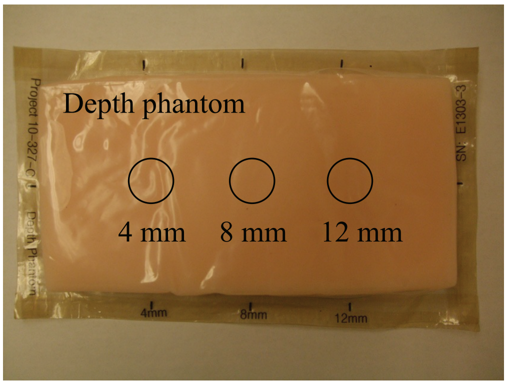

Figure 6.9: The manufactured depth phantom.

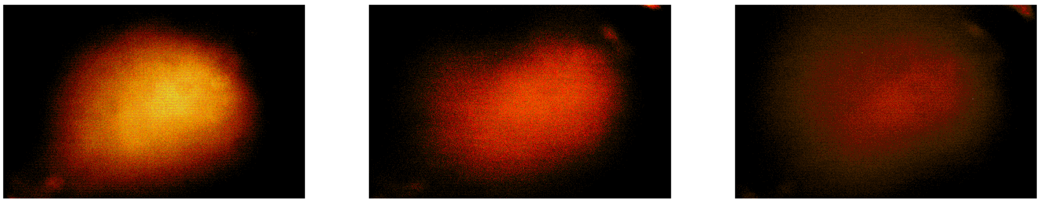

(a) (b) (c)

Figure 6.10: The tactile data of three inclusions embedded in the depth phantom. (a) 4 mm depth inclusion, (b) 8 mm depth inclusion, (c) 12 mm depth inclusion.

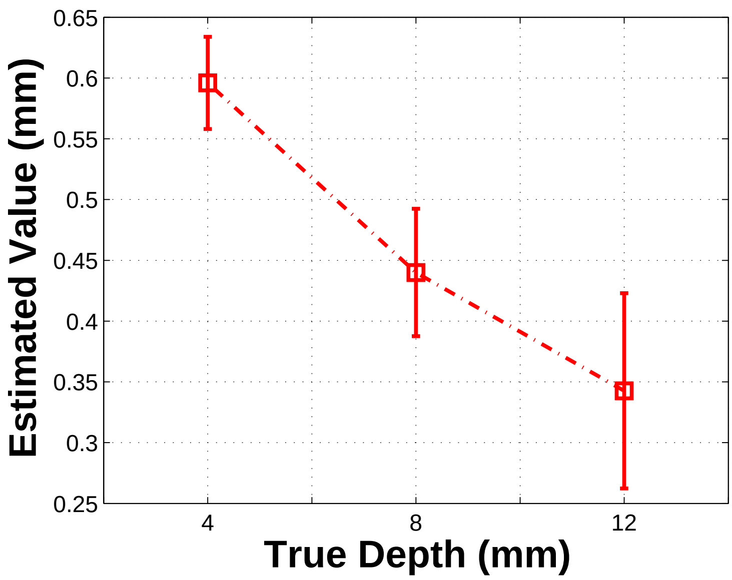

Figure 6.11: Error bar chart of estimated relative depth of each inclusion.

the first inclusion. This shows larger error for the deepter inclusion estimation.

6.2.5 Relative Hardness Estimation Method

The word "hardness" is expressed by the Young's modulus E. The relative Young's modulus or relative hardness is expressed as relative stress over relative strain. The relative stress is measured as force per unit area. In this research, we estimate the force F using the summation of pixels in tactile data M (Lee and Won, 2011a). The relationship between the force F and the integrated pixel value M is obtained from the initialization.

The other value needed for the relative Young's modulus is the relative strain. The strain is the fraction change in length in response to the stress. Strain is the geometrical deformation measure indicating the relative displacement between points on the target. Thus, if we know the displacement of any particular set of points on tactile data obtained under different loading forces to the target, then we can find the relative strain presented by the loading forces. To find the relative stain T, first we obtained two different tactile data under different compression ratios. We then measured the relative size from each tactile data using Eq. (6.2). The estimate strain T is measured by the difference of the each relative size as below.

$$T = \frac{d_1 - d_2}{d_1}, \tag{6.10}$$

where d_1 is the estimated tissue inclusion size using first tactile data and d_2 is the estimated tissue inclusion size using second tactile data. The obtained stress and strain are finally used to estimate the relative hardness of an inclusion. The unit of the relative hardness of an inclusion is Pa. In this research, we assume that a tissue inclusion is spherical and there is only one inclusion in the tissue. Also we assume that there is no noise in the tactile data.

6.2.6 Relative Hardness Estimation Experimental Results

The hardness tissue phantom has three inclusions with different Young's modulus: 40, 70, and 100 kPa. The Young's modulus of the tissue inclusion was chosen to represent normal glandular tissue (40 kPa) and invasive ductal carcinoma (100 kPa) at 5% precompression with a loading frequency of 4.0 Hz (Krouskop et al., 1998). Next we added one more inclusion with the in between elastic modulus of 70 kPa. The size of inclusions was 10 mm, and they were placed 5 mm below the surface of the phantom. The schematic of the hardness phantom is shown in Fig. 6.12 and the manufactured hardness phantom is shown in Fig. 6.13. To obtain the tactile data under different compression ratios, first we placed the phantom in the desk. We then placed the TSIS onto the phantom surface where the tissue inclusion was embedded and pressed the TSIS to obtain one tactile data and pressed the TSIS again with a higher compression ratio to obtain another tactile data. Under two different compression ratios, we obtained 15 tactile data of each inclusion. The relative hardness of a tissue inclusion was estimated using Eq. (6.10) and averaged. Fig. 6.14 represents the sample tactile data of each inclusion.

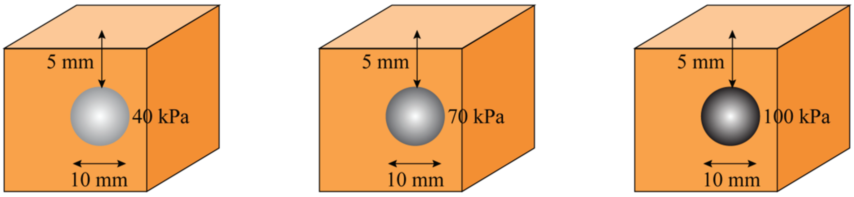

Figure 6.12: The schematic of the hardness phantom.

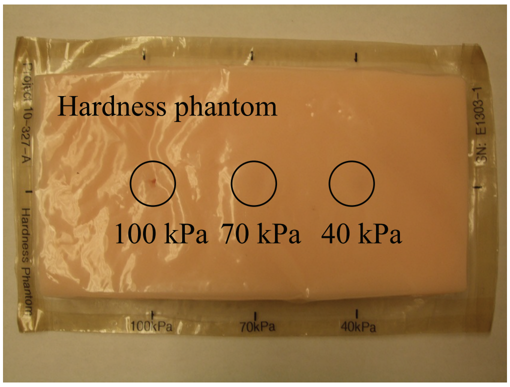

Figure 6.13: The manufactured hardness phantom.

The Young's modulus estimation result is shown in Fig. 6.15. The plot shows that the 40 kPa Young's modulus case had the lowest mean of 82.59 kPa, and the smallest standard deviation, indicating that the observations were close to the mean. On the contrary, the 100 kPa Young's modulus case had the more widely spread out Young's modulus, with a 252.25

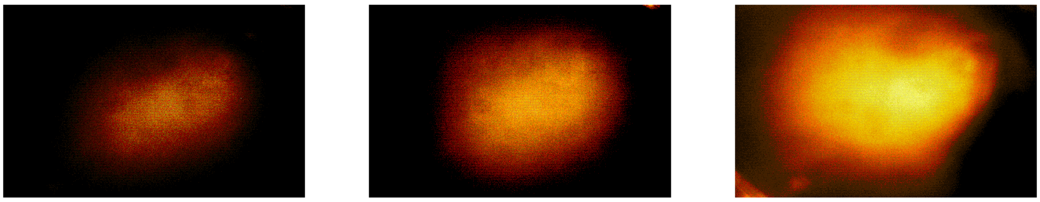

(a) (b) (c)

Figure 6.14: The tactile data of three inclusions embedded in the hardness phantom. (a) 40 kPa Young's modulus inclusion, (b) 70 kPa Young's modulus inclusion, (c) 100 kPa Young's modulus inclusion.

kPa mean value and 35.87 kPa standard deviation, as can be seen in its error bar chart. The 70 kPa Young's modulus case had an average of 149.93 kPa and standard deviation of 29.83 kPa. The ratio of the real Young's modulus of inclusions was approximately 1 : 1.75 : 2.5. The estimated ratio of relative hardness was approximately 1 : 1.81 : 3.05. This corresponds to about 3.43% and 22.0% relative error compared to the first inclusion. The error was larger for the stiffer inclusion. Nevertheless, we could distinguish relative hardness of the inclusions from the tactile data.

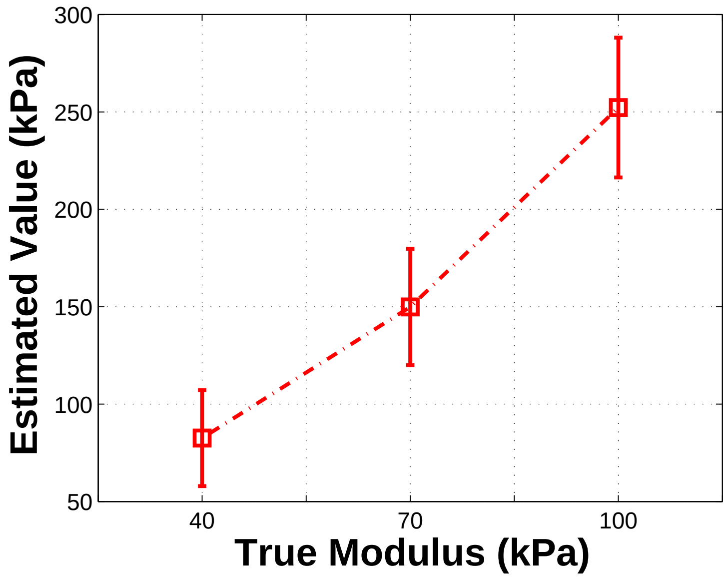

Figure 6.15: Error bar chart of estimated relative hardness of each inclusion.

6.2.7 Other Tissue Inclusion Parameters – Shape and Mobility

In addition to inclusion parameters of size, depth, and hardness, shape and mobility are two additional important parameters that can be used for the tissue inclusion characterization. The descriptions of these two parameters are given below.

Inclusion Shape Estimation

To estimate the tissue inclusion shape, it is necessary to segment the tactile data into regions (on their contours) corresponding to the touched object. Thresholding is one of the popular methods for image segmentation purposes. From a gray-scale tactile data, the thresholding technique is used to generate the binary data. During the segmenration process, individual pixels in the tactile data are marked as “object” pixels if the value is higher than some threshold value (assuming an object to be brighter than the background) and as “background” pixels otherwise. Typically, an object pixel is assigned a “1” value and a background pixel is assigned a “0” value. Finally, depending upon a pixel’s label, a binary tactile image is generated by assigning each pixel white or black. If $g(x, y)$ is a thresholded pixel of $I(x, y)$ at some threshold T,

$$g(x,y) = \begin{cases} 1 & \text{if } I(x,y) \geq T, \\ 0 & \text{otherwise.} \end{cases} \tag{6.11}$$

One of the popular thresholding methods is the clustering algorithm using K-means variation (Niemisto et al., 2007), (Hartigan and Wong, 1979). In our case, two clusters (background and object) are considered. Let threshold be T, and $\mu_B(T)$ be the mean of all pixels less than the threshold (background) and $\mu_O(T)$ be the mean of all pixel values higher than the threshold (object). Then the threshold can be found as follows:

$$\forall I \geq T : |I - \mu_B(T)| \geq |I - \mu_O(T)|, \tag{6.12}$$

and

$$\forall I < T : |I - \mu_B(T)| < |I - \mu_O(T)|. \tag{6.13}$$

The basic idea of K-means variation is to start by estimating $\mu_B(T)$ as the average of the four corner pixels (assumed to be background) and $\mu_O(T)$ as the average of everything else. Set the threshold T to be halfway between $\mu_B(T)$ and $\mu_O(T)$, thus separating the pixels according to how close their intensities are to $\mu_B(T)$ and $\mu_O(T)$, respectively. Now, update the estimates of $\mu_B(T)$ and $\mu_O(T)$ by actually calculating the means of the pixels on each side of the threshold T by reducing the threshold T. This process repeats until the threshold T is below the specified level and labels all tactile data pixels into "object" and "background". From this process, we can segment the "object" and the "background". Based on the segmented "object", we can finally estimate the shape of a tissue inclusion.

Inclusion Mobility Estimation

The mobility of the tissue inclusion can be estimated as a Euclidean distance between the centroid (X_c, Y_c) of tactile data obtained through continuous time t. Let the centroids of tactile data obtained at time $t-1$ be $(X_{c_{t-1}}, Y_{c_{t-1}})$ and centroid of tactile data obtained at time t be (X_{c_t}, Y_{c_t}). The inclusion mobility M then can be calculated as follows.

$$M = \sqrt{|X_{c_t} - X_{c_{t-1}}|^2 + |Y_{c_t} - Y_{c_{t-1}}|^2}. \tag{6.14}$$

The mobility of the tissue inclusion is estimated as a Euclidean distance between tactile image centroids. In other words, the longer Euclidean distance means the larger mobility characteristic of a tissue inclusion, and the shorter Euclidean distance means the smaller mobility characteristic of a tissue inclusion.

6.3 Absolute Tissue Inclusion Parameter Estimation

In this section, the absolute tissue inclusion parameter estimation method is proposed to measure the hardness as well as geometric parameters of a target. The estimation is performed based on the tactile data obtained at the surface of the tissue using the TSIS. The forward algorithm is designed to comprehensively predict the tactile data based on the mechanical properties of tissue inclusion using FEM. This forward information is used to develop an inversion algorithm that will be used to extract the size, depth, and Young's modulus of a tissue inclusion from the tactile data. We utilize ANN for the inversion algorithm. The proposed estimation method was validated by the realistic tissue phantom with stiff inclusions.

6.3.1 Forward Algorithm

The purpose of the forward algorithm is to find the relationship between tissue inclusion parameters and tactile data. In this research, a FEM is considered for the forward algorithm. The FEM modeling based on the idealized breast tissue model is performed using ANSYS ver. 11.0, an engineering simulation software package (ANSYS Inc., PA). The FEM model consists of a three-layered sensing probe, soft tissue and inclusion. All are modeled using SOLID95 3D elements available in ANSYS. Appropriate surface-to-surface contact elements have been defined in the ANSYS database model. The model consists of 3,000 finite elements. In addition, the following assumptions are used for the FEM forward modeling (Fung, 1993; Parker et al., 1990).

1) The breast tissue and inclusions are elastic and isotropic. This means that the properties of a material are identical in all directions.

2) The Poisson's ratio of each material is set to 0.49 because the breast tissue is elastic.

3) The breast tissue is assumed to be sitting on non-deformable hard surfaces such as bones.

The FEM model that we constructed is shown in Fig. 6.16.

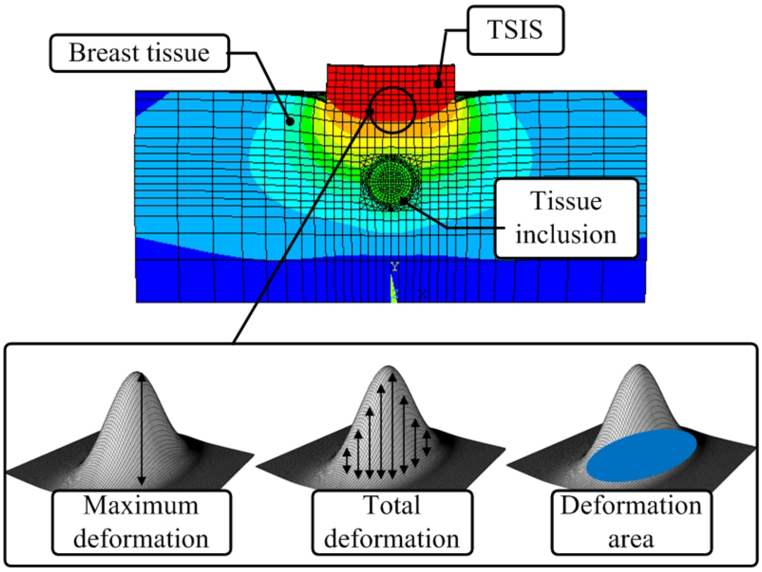

Figure 6.16: The FEM model of an idealized breast tissue model. The sensing probe of TSIS is also modeled on top of the breast tissue model. In FEM, the deformed shape of the sensing probe is captured as maximum deformation, total deformation, and deformation area.

If the TSIS compresses against the tissue surface containing a stiff tissue inclusion, the sensing probe of the TSIS deforms. In FEM, the deformed shape of the sensing probe is captured in response to the different inclusion parameters of size d, depth h, and Young's modulus E. To quantify the amount of sensing probe deformation, the following definitions are used.

1) Maximum deformation, O^1_{FEM}, is defined as the largest vertical displacement of the FEM element of the sensing probe from the non-deformed position.

2) Total deformation, O^2_{FEM}, is defined as the vertical displacement summation of FEM elements of the sensing probe from the non-deformed position.

3) Deformation area, O^3_{FEM}, is defined as the projected area of the deformed surface of the sensing probe.

In the forward algorithm, (d, h, E) are input variables and maximum deformation O^1_{FEM}, total deformation O^2_{FEM}, and deformation area O^3_{FEM} of the sensing probe are output variables. The diagram of input variables (d, h, E) and output variables (O^1_{FEM}, O^2_{FEM}, O^3_{FEM}) of FEM is shown in Fig. 6.17.

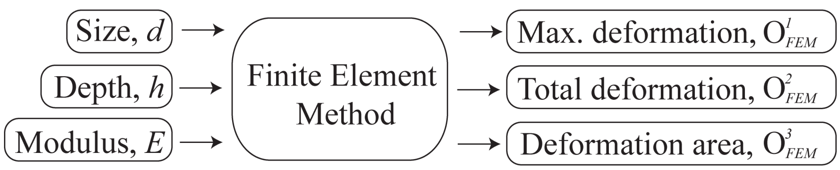

Figure 6.17: The diagram of input variables (d, h, E) and output variables (O^1_{FEM}, O^2_{FEM}, O^3_{FEM}) in forward algorithm.

To investigate the relationship between the input variables (d, h, E) and the output variables (O^1_{FEM}, O^2_{FEM}, O^3_{FEM}), 134 input variables (d, h, E) are randomly generated with the minimum and maximum constraints of d as [0 mm; 15 mm], h as [4 mm; 12 mm], and E as [40 kPa; 120 kPa] (Krouskop et al., 1998). Then 134 output variables (O^1_{FEM}, O^2_{FEM}, O^3_{FEM}) corresponding to 134 input variables (d, h, E) are generated using FEM. Figs. 6.18(a) to 6.18(c) represents 134 output variables of maximum deformation O^1_{FEM}, total deformation O^2_{FEM}, and deformation area O^3_{FEM} with respect to changing input variables (d, h, E). To visualize 134 output variable O^1_{FEM} in 3-D space, the values of O^1_{FEM} are rescaled to [0; 255] and displayed as circles at the locations specified by input variables (d, h, E). The size of each circle is determined by the values.

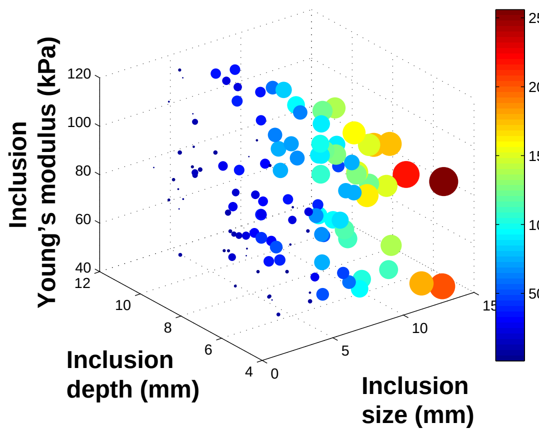

(a)

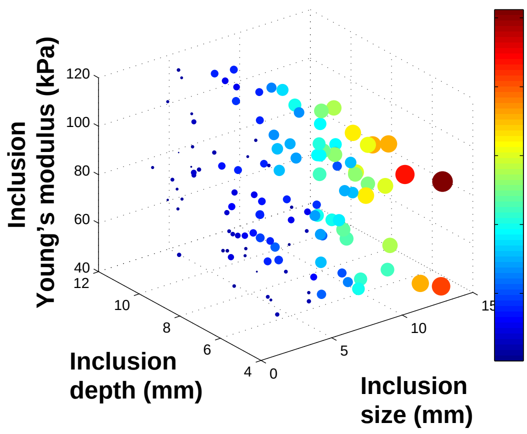

(b)

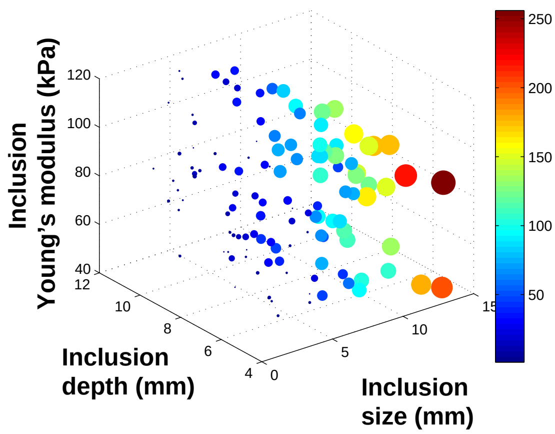

(c)

Figure 6.18: (a) The maximum deformation O^1_{FEM}, (b) Total deformation value O^2_{FEM}, (c) Deformation area O^3_{FEM} of TSIS sensing probe depending on the inclusion size d, depth h, and Young's modulus E. The 4-D dimension shows the maximum deformation value O^1_{FEM}, rescaled from 0 to 255.

We notice that as the size of inclusion d increases, the maximum deformation O^1_{FEM} increases as the effect of bigger tissue inclusion causes more change in the sensing probe deformation. As the depth of inclusion h increases, the maximum deformation O^1_{FEM} decreases as the effect of stiff inclusion gets reduced and the sensing probe presses the soft tissue. Also, as the Young's modulus E of inclusion increases, the maximum deformation O^1_{FEM} increases as the stiff inclusion makes the sensing probe deform more. We noticed that the other two output variables O^2_{FEM} and O^3_{FEM}, have similar patterns.

6.3.2 Mapping Tactile Data

It is necessary to relate FEM tactile data (O^1_{FEM}, O^2_{FEM}, O^3_{FEM}) and tactile data (O^1_{TSIS}, O^2_{TSIS}, O^3_{TSIS}). To map two different tactile data, realistic calibration tissue phantom with nine embedded stiff inclusions has been manufactured (CIRS, Inc., VA). This calibration tissue phantom was made of a silicone composite having Young's modulus of approximately 5 kPa. The inclusion was made using another silicone composite with the stiffness higher than the surrounding tissue phantom. We custom designed the calibration tissue phantom with varying parameters (d, h, E) as shown in Table 6.2.

To map TSIS tactile data to FEM tactile data, tactile data of nine inclusions in calibration tissue phantoms were obtained using the TSIS. In order to quantify TSIS tactile data, maximum pixel value O^1_{TSIS}, total pixel value O^2_{TSIS}, and deformation area of pixel O^3_{TSIS} of TSIS tactile data are computed. We assume that there is no noise in the tactile data.

1) Maximum pixel value, O^1_{TSIS}, is defined as the pixel value in the centroid of the tactile data.

2) Total pixel value, O^2_{TSIS}, is defined as the summation of pixel values in the tactile data.

3) Deformation area of pixel, O^3_{TSIS}, is defined as the number of pixel greater than the specific threshold value k in the tactile data.

To find the relationship between TSIS tactile data and FEM tactile data, the graphs of (O^1_{FEM} : O^1_{TSIS}), (O^2_{FEM} : O^2_{TSIS}), and (O^3_{FEM} : O^3_{TSIS}) were generated. Then, using the linear regression method, the relationship between TSIS tactile data and FEM tactile data is found. Figs. 6.19(a) to 6.19(c) represent linear regression results. Because the tactile data is normalized, three data in each graph exist in the same position (1,1). Using these three relationships, the newly obtained TSIS tactile data (O^1_{TSIS}, O^2_{TSIS}, O^3_{TSIS}) can be transformed into the FEM tactile data (O^1_{FEM}, O^2_{FEM}, O^3_{FEM}). In this way, we relate TSIS tactile data with FEM tactile data.

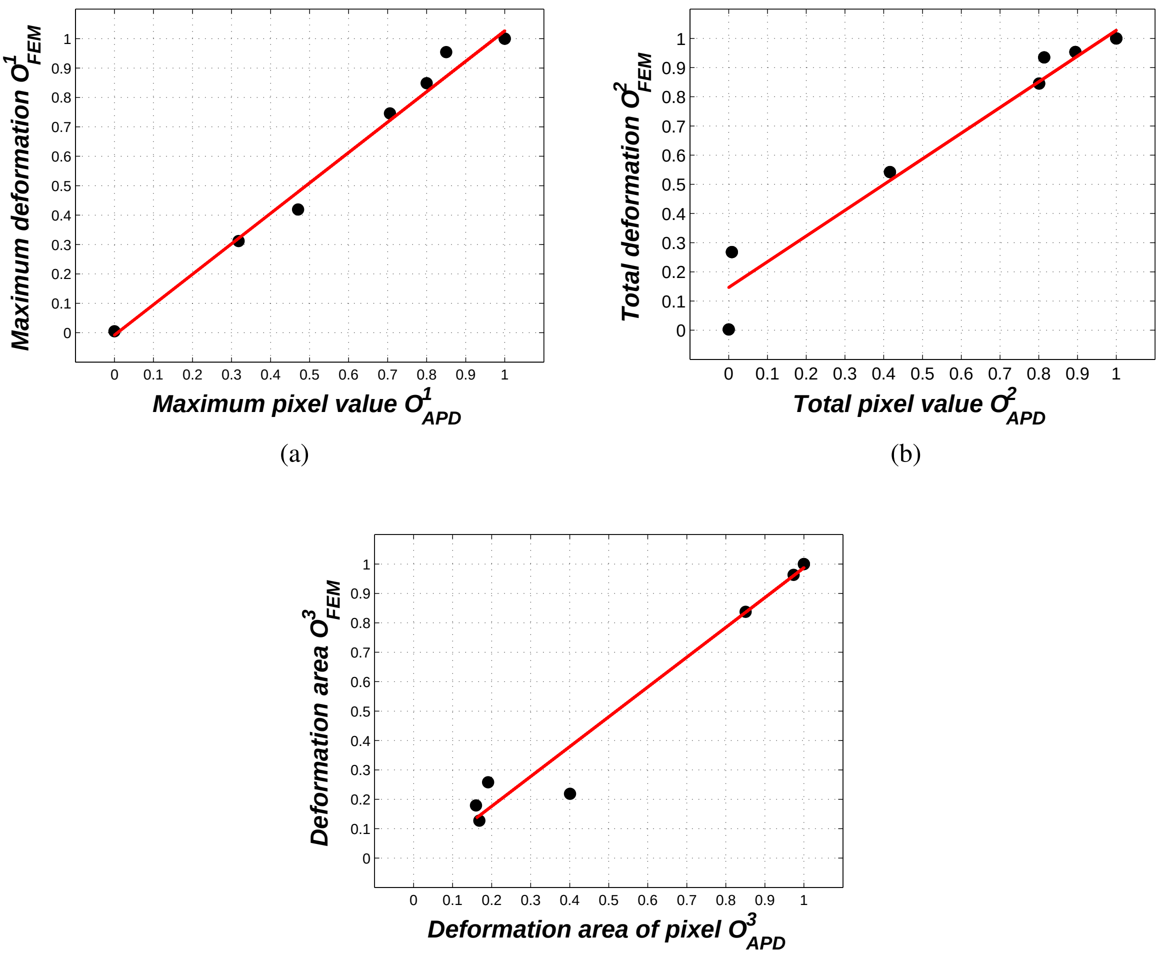

(a) (b) (c)

Figure 6.19: The linear regression results between FEM tactile data and TSIS tactile data. (a) The linear regression result between maximum deformation O^1_{FEM} and maximum pixel value O^1_{TSIS}, (b) The linear regression result between total deformation O^2_{FEM} and total pixel value O^2_{TSIS}, (c) The linear regression result between deformation area O^3_{FEM} and deformation area of pixel O^3_{TSIS}.

6.3.3 Inversion Algorithm

The goal of an inversion algorithm is to estimate (d, h, E) through newly obtained TSIS tactile data (O^1_{TSIS}, O^2_{TSIS}, O^3_{TSIS}). In the FEM forward modeling, 134 input variables (d, h, E) and their corresponding output variables (O^1_{FEM}, O^2_{FEM}, O^3_{FEM}) are investigated. Also using the tissue phantom experiments, the linear regression relationships between (O^1_{FEM}, O^2_{FEM}, O^3_{FEM}) and (O^1_{TSIS}, O^2_{TSIS}, O^3_{TSIS}) are obtained. Now, we design an inversion algorithm to estimate (d, h, E) using newly obtained (O^1_{TSIS}, O^2_{TSIS}, O^3_{TSIS}). Fig. 6.20 shows the diagram of input variables (O^1_{TSIS}, O^2_{TSIS}, O^3_{TSIS}) and output variables (d, h, E) of the inversion algorithm.

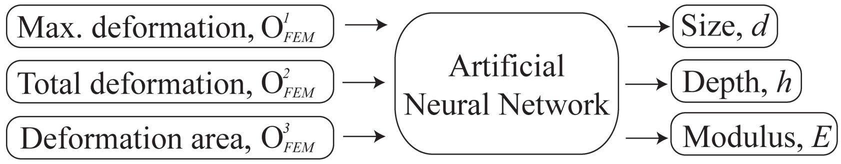

Figure 6.20: The diagram of input variables and output variables in inversion algorithm.

In this research, the multi-layered ANN is considered as an inversion algorithm (Bishop, 2007). ANN is a computational model that is inspired by the structure and functional aspects of biological neural networks and is trained using the input variables to obtain the desired output variables. The multi-layered ANN consists of neurons united in layers. Each i layer is connected with i-1 and i+1 layers and neurons within the layer are not connected to each other. To train the ANN, 125 input variables (O^1_{FEM}, O^2_{FEM}, O^3_{FEM}) and corresponding output variables (d, h, E) are used. The remaining nine variables (d, h, E), which are used for the tissue phantom design, are used for the trained the ANN validation. In ANN, too many neurons would lead to over-fitting and large variance of error, but not enough neurons would cause high mean-squared error results. Thus, the numbers of neurons and layers were set experimentally to three layers. The $1st$ layer uses 10 neurons with sigmoid activation function. The $2nd$ layer uses four neurons with sigmoid activation function. The $3rd$ layer uses three neurons with linear activation function. Fig. 6.21 shows the ANN structure.

For the training ANN algorithm, scaled conjugate gradient algorithm (SCGA) is utilized due to its simple and robustness characteristics compared to the other learning algorithm (Bishop, 2007). SCGA is based upon a class of optimization techniques well known in numerical analysis as the conjugate gradient methods. SCGA uses second order information from ANN but requires only $O(N)$ memory usage, where n is the number of weights in ANN.

6.3.4 Experimental Results

To validate the performance of the proposed estimation method, tactile data of nine tissue inclusions were obtained using the TSIS and then quantified as (O^1_{TSIS}, O^2_{TSIS}, O^3_{TSIS}). These

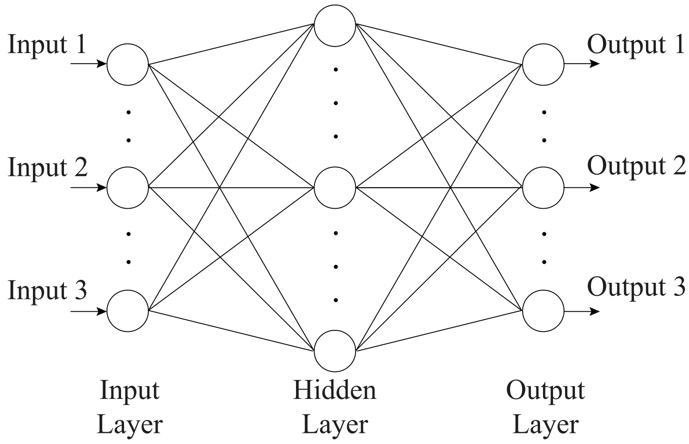

Figure 6.21: The multi-layered artificial neural network structure.

(O^1_{TSIS}, O^2_{TSIS}, O^3_{TSIS}) are used to estimate inclusion parameters (d, h, E) through the trained ANN. To validate the performance of the proposed estimation method, the cross-validation method called leave-one-out-cross-validation (LOOCV) metric is considered (Picard and Cook, 1984). The LOOCV is a special case of k-fold cross-validation where k equals the number of instances in the data (Picard and Cook, 1984). After getting new TSIS tactile data of each inclusion, inclusion parameters (d, h, E) of each inclusion were estimated using the ANN with the LOOCV. These estimation trials were performed 100 times per inclusion and the results were averaged.

First we used the root mean squared error (RMSE) performance metric. Let T be the true inclusion parameters (d, h, E) in Table. 6.2, and Y be the estimated inclusion parameters ($\hat{d}$, $\hat{h}$, $\hat{E}$) in Table. 6.2. Then the RMSE e_j can be calculated as follows.

$$e_j = \sqrt{\frac{1}{n} \times \sum_{i=1}^{n} (T_{ij} - Y_{ij})^2} \tag{6.15}$$

where i is the number of inclusions which is nine and j is the number of tissue inclusion parameters, which is three in our case. Figs. 6.22(a) to 6.22(c) show the RMSE of each parameter (d, h, E) with 100 experimental trials. Figs. 6.22(a) to 6.22(c) shows the RMSE of each parameter (d, h, E) estimation over 100 trials. Table 6.1 shows the RMSE of all inclusion parameter estimation results.

Next, we calculate the relative error for the validation of the estimation performance. The

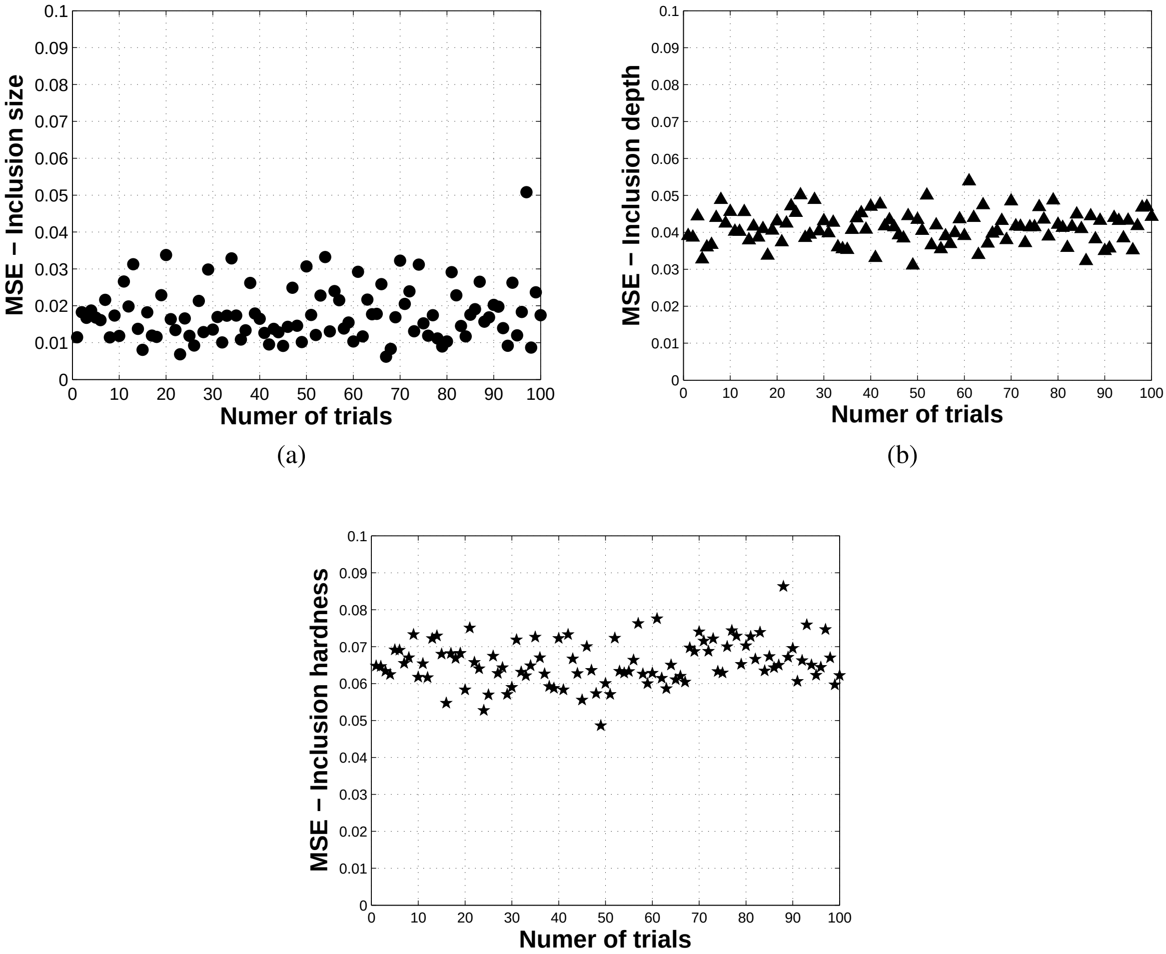

(a) (b) (c)

Figure 6.22: The mean square error of inclusion's parameter estimation over 100 experiments. (a) Inclusion size case, (b) Inclusion depth case, (c) Inclusion hardness case.

Table 6.1: The root mean squared error (RMSE) of inclusion parameter estimation.

Inclusion parameter	RMSE
Size (d)	1.25 mm
Depth (h)	2.09 mm
Modulus (E)	28.65 kPa

relative estimation errors of each inclusion case are shown in Table. 6.2. The results show that the minimum and maximum relative estimation errors for the tissue inclusion size case are 0.75% and 115.5%. The mean estimation error is 22.54% with 36.03% standard deviation. For the depth estimation case, the minimum and maximum relative errors are 6.25% and 79.25%. The mean error is 36.34% with 23.64% standard deviation. For the Young's modulus estimation case, the minimum and maximum relative errors are 17.03% and 123.27%. The mean error is 38.32% with 32.99% standard deviation.

As can be seen in the results, the size and depth was estimated precisely compared to the Young's modulus. The reason for the higher estimation error of Young's modulus case compared to other two property cases is that the inclusion Young's modulus change is not large once the Young's value is greater than the specific threshold value. Conversely, inclusion size and depth variations appear more variable in the tactile data. Thus, estimation errors of inclusion size and depth cases are lower than the Young's modulus estimation case.

Table 6.2: The actual parameters (d, h, E) and estimated parameters ($\hat{d}$, $\hat{h}$, $\hat{E}$) with relative estimation errors of 9 inclusions in the calibration tissue phantom.

No.	True d	Est. $\hat{d}$	Err.	True h	Est. $\hat{h}$	Err.	True E	Est. $\hat{E}$	Err.
1	2mm	4.31mm	115.5%	5mm	8.2mm	64%	120kpa	77.12kPa	35.73%
2	8mm	7.38mm	7.75%	5mm	7.41mm	48.2%	120kpa	78.31kPa	34.74%
3	13mm	9.73mm	25.15%	5mm	6.55mm	31%	120kpa	80.35kPa	33.04%
4	7mm	7.34mm	4.86%	4mm	7.17mm	79.25%	100kpa	82.1kPa	17.89%
5	7mm	5.52mm	20.57%	8mm	8.5mm	6.25%	100kpa	77.06kPa	22.94%
6	7mm	5.56mm	29.43%	12mm	7.75mm	35.41%	100kpa	79.92kPa	20.08%
7	10mm	10.09mm	0.9%	5mm	5.88mm	17.6%	40kpa	89.31kPa	123.28%
8	10mm	10.07mm	0.75%	5mm	5.85mm	17%	70kpa	98.12kPa	40.17%
9	10mm	10.64mm	6.41%	5mm	6.42mm	28.34%	100kpa	82.97kPa	17.03%
Mn.			22.54%			36.34%			38.32%
Std.			36.03%			23.64%			32.99%

6.4 Sensitivity and Specificity Test

In this section, the sensitivity and specificity of the TSIS are investigated. To measure the sensitivity and specificity of the TSIS, we used the tissue phantom which contains eight tissue inclusions (MammaCare Corp., FL). The sensitivity of the TSIS was obtained by calculating true-positive results, T_p, and false-positive results, F_p, through detecting eight tissue inclusions in the phantom using the TSIS. To measure the specificity of the TSIS, the number of true-negative results, T_n, and number of false-negative results, F_n, was calculated while scanning the tissue phantom without tissue inclusions. The experimental results show that the number of true-positive results, T_p, was six and the number of false-negative results, F_n, was two, resulting in a sensitivity of 75% for the TSIS. For the specificity, the number of true-negative results, T_n, was seven and the number of false-positive results, F_p, was one. Thus, the specificity is 87.5%. These are the preliminary results of the TSIS sensitivity and specificity test. If we increase the number of samples, then we may collect more precise TSIS sensitivity and specificity data.

The relationship between sensitivity and specificity can be illustrated by the receiver operating characteristic (ROC) curve, which is a graphical plot of the true-positive rate (sensitivity), against the false-positive rate (1-specificity) (Rangayan, 2005). A ROC curve facilitates advanced analysis of the classification accuracy of a diagnostic method (Metz, 1978). An ROC curve for TSIS sensitivity and specificity is shown in Fig. 6.23. The graph is plotted using the true-positive rate (sensitivity) and false-positive rate (1-specificity).

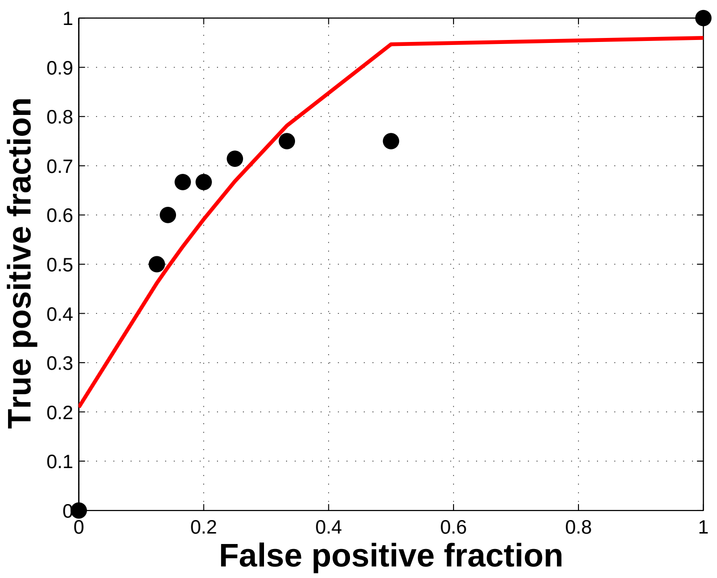

Figure 6.23: Receiver operating characteristic (ROC) curve of TSIS.

Generally, the closer the ROC curve follows the left-hand border of the graph and then the top border of the graph, the more accurate the test. The closer the curve comes to the 45^o diagonal of the graph, the less accurate the test. The shape of the ROC curve can be determined by the area under the curve (AUC). Thus, the AUC can be used as a measure of test accuracy. An

AUC of 1 represents a perfect test and an AUC of 0.5 represents a worthless test. A experimental result that gives a larger AUC indicates a better method than one with a smaller area (Roques et al., 2000). In general terms, an AUC above 0.8 is considered excellent, between 0.75 and 0.8 is very good, between 0.7 to 0.75 is good, between 0.6 to 0.7 is poor, and between 0.5 to 0.6 is a fail (Roques et al., 2000). Because the AUC of the TSIS ROC curve is 0.735, according to the classification of (Roques et al., 2000), the TSIS experimental results can be considered as good.

6.5 Discussions

In this chapter, the tissue inclusion parameter estimation method is proposed to quantify the hardness and geometric parameters of tissue inclusions. The estimation is performed based on the tactile data obtained by the TSIS. Two different estimation approaches are proposed in this chapter. The first approach is to estimate the relative parameters of tissue inclusion. Using the salient features of the captured tactile data, we estimate relative inclusion parameters such as size, depth, and hardness. The second approach is to estimate the absolute parameters of tissue inclusion. To design the absolute parameter estimation method, we used the FEM based forward algorithm and the ANN based inversion algorithm. The performance of the method was experimentally verified using realistic tissue phantoms with embedded stiff inclusions. The experimental results showed that the relative size and hardness estimation errors were smaller than the relative depth estimation errors. If the inclusion's size was smaller, the estimation error was also smaller. Also the shallower depth inclusion case has smaller depth estimation error than the inclusions embedded deeper. Furthermore, if the Young's modulus of an inclusion was smaller, the estimation error was smaller than the higher Young's modulus case. We conclude, however, that we could distinguish between soft, medium, and hard inclusions, which will allow us to distinguish malignant and benign tumors. For the absolute parameter estimation experiments, the proposed estimation method can measure the size, depth, and Young's modulus of a tissue inclusion with 1.1%, 2.86%, and 17.79% minimum relative errors, respectively. This work is the initial step towards achieving the TSIS and associated parameter estimation method for early breast tumor detection and characterization.

The tissue inclusion parameter estimation method is a phantom - or patient - dependent approach. The forward algorithm using FEM has been constructed based on the idealized breast tissue model. Different women have different breast thickness, shape, and Young's modulus, so the parameters of the FEM model should be updated to the new geometry for the better estimation results. For this purpose, the FEM model that we used is parameterized and can be easily changed depending upon the different patient geometry.

To map TSIS tactile data to FEM tactile data, only nine inclusions were used. Although we showed that the relationship between TSIS tactile data and FEM tactile data can be approximately linear, the number of sample data is not enough to describe the whole relationship between TSIS tactile data and FEM tactile data. If we use more tissue inclusions for the mapping purpose, the relationship would be more accurate and estimation errors will be reduced.

In this research, we estimate three parameters such as size, depth, and hardness of tissue inclusion using three salient features of tactile image simultaneously. This method has been performed by finding relationships between three parameters and three salient features of tactile image using forward algorithm and then train the inversion algorithm with forward algorithm data. In the future work, we will investigate the individual relationship between each parameter and each salient feature of tactile image. This way will allow us to investigate more accurate relationship between tissue inclusion parameters and tactile images.

The accurate classification of cancer at an early stage can prevent unnecessary future diagnostic tests. In this regard, a classification system is the important tool. The primary objective of the classification system is to minimize potential diagnosis errors and to provide medical examination results in an elaborated manner and within very short time. Previously, various classification systems using statistical learning algorithms have been successfully implemented on different bioinformatics applications like diagnosis of leukemia, lung cancer, ovarian cancer, and brain cancer (Byvatov and Schneider, 2003), (Golub et al., 1999), (Shipp et al., 2002). Although these implementations turned out to be a success, there is still a need for the robust and efficient classification algorithm. In future work, the support vector machine (SVM) can be considered for the tactile data classifier design for cancer classification. The SVM is a set of related statistical supervised learning algorithms. It was originally designed for classification and regression tasks as a potential alternative to conventional ANNs (Vapnik, 1995). Usually, the prediction accuracy of the SVM-based classifier is higher than that of the ANN (Vapnik, 1995).

CHAPTER 7
CONCLUSIONS AND FUTURE WORK

7.1 Conclusions

In this dissertation, a tactile sensation imaging system (TSIS) and associated algorithms capable of measuring the characteristics of tissue inclusions were designed and experimentally evaluated. The main focus of this dissertation was on breast tumor warning application, specifically identifying tumor parameter estimation such as size, depth, and hardness. The work presented in this dissertation will extend to other applications such as prostate or thyroid tumor detection.

In Chapter 2, we presented a background and literature review of artificial tactile sensor. A review of the human tactile sensing mechanism was presented, followed by a review of various artificial tactile sensor designs and elasticity determination systems. The application of modern breast tumor detection methods was also discussed.

In Chapter 3, we described the principle of the tactile sensation imaging, which utilizes the total internal reflection (TIR) in the optical sensing probe. We analyzed the feasibility of the tactile sensation imaging principle using wave optics, which clearly showed that the tactile data can be obtained when the TSIS sensing probe is compressed by the external force. The analytical solution of tactile sensation imaging was then verified using the numerical simulations.

In Chapter 4, we presented the hardware and software design descriptions of the TSIS. The description of each component for the TSIS hardware design is presented first, followed by the optical waveguide fabrication method and software design description. The specification of the TSIS was also provided. To get a sample tactile image of tissue inclusion, a realistic breast tissue phantom with a 2-mm diameter spherically shaped inclusion was manufactured. Througout the phantom experiments, the TSIS enabled the successful detection of stiff tissue inclusions.

In Chapter 5, we presented the tactile data processing algorithm for the target hardness estimation which is accomplished by adopting a new non-rigid point matching algorithm called "topology preserving relaxation labeling (TPRL)." Using this algorithm, a series of tactile data was registered and strain information was calculated. The stress information was measured throughout the integration of pixel values of the tactile data. The stress and strain measurements were taken for unique identification of the elasticity of the touched object. The measurement method was validated by commercial polymer samples with a known hardness. The results showed that using the TSIS, the hardness of the touched object was estimated within 5.38% relative error.

In Chapter 6, we investigated the capability of the TSIS to quantify the hardness and geometric parameters of tissue inclusion via indirect contact. The estimation was performed based on the tactile data obtained at the surface of the tissue using the TSIS. Two different estimation approaches are investigated. The first approach is to estimate the relative parameters of tissue inclusion. Using the salient features of the captured tactile data, we estimate relative inclusion parameters such as size, depth, and hardness. The second approach is to estimate the absolute parameters of tissue inclusion. The estimation method consists of the forward algorithm and inversion algorithm. The forward algorithm is designed to comprehensively predict the tactile data based on the parameters of the inclusion in the soft tissue. This algorithm is used to develop the inversion algorithm that can be used to extract the size, depth, and hardness of an inclusion. The performance of the estimation method was experimentally verified using realistic tissue phantoms with nine embedded stiff inclusions. For the relative tissue inclusion parameter estimation case, the experimental results showed that the relative size and hardness estimation errors were smaller than the relative depth estimation errors. Furthermore, if the Young's modulus of an inclusion was smaller, the estimation error was smaller than the higher Young's modulus case. For the absolute tissue inclusion parameter estimation case, the experimental results showed that the minimum and maximum relative estimation errors for the tissue inclusion size case were 0.75% and 115.5%. The mean estimation error was 22.54% with 36.03%

standard deviation. For the depth estimation case, the minimum and maximum relative errors were 6.25% and 79.25%. The mean error was 36.34% with 23.64% standard deviation. For the Young's modulus estimation case, the minimum and maximum relative errors were 17.03% and 123.27%. The mean error was 35.97% with 33.38% standard deviation.

7.2 Future Work

The work presented in this dissertation is the initial step towards developing a TSIS for early breast tumor detection and characterization. Here are some future works.

The TSIS developed in this dissertation is not robust to the background light disturbance and drifting of the light source. If the background light is too bright compared to the light of the TSIS, it causes error. Thus, TSIS should be used in a relatively dark room to minimize the background light disturbance. In addition, the drifting of light occurs if the light sources of TSIS are positioned incorrectly and the camera captures the spurious light. In this case, the drifted light is shown as noise in the tactile data. To prevent this, precise positioning and direction of the TSIS light source are required. Future works may focus on the digital image processing of tactile image using image segmentation algorithm. More specifically, the image segmentation technique can be used to extract the boundary of the desired light scattering area in the tactile data and remove the noise. This will generate the final tactile image without noise and light disturbance.

Usually the LED is quite sensitive to the light intensity drift which is possibly caused by the variation of the resistance in the power source. To prevent the variation of the resistance in the power source, we will consider the constant current LED drive circuit in the TSIS. The constant current circuit will prevent the intensity drift of LED light sources of the TSIS.

Breast tissue mechanically behaves as a viscoelastic polymer, meaning it is both viscous and elastic (Darvish, 2009), (Sridhar and Insana, 2007). If the breast tissue is pressed by the TSIS, it needs time to be stabilized. Thus, we press the TSIS onto the breast tissue and wait for specific time without releasing the pressure until the deformed breast tissue stabilizes. The required waiting time would be from few seconds to several minutes depending upon the breast tissue density and composition. In future work, we will investigate the relationship between the viscoelastic behavior of breast tissue and the TSIS performance, and we will also investigate the exact specific waiting time required for breast tissue stabilization.

The tissue inclusion parameter estimation method, proposed in this dissertation, is a phantom or patient dependent approach. The FEM based forward algorithm has been constructed based on the idealized breast tissue model. Because women have different tissue parameters, rather than the idealized breast tissue model, if the patient is changing, the FEM based forward algorithm should be redesigned to regenerate the proper tactile data for the better estimation results. For this purpose, the FEM model in this dissertation is parameterized and can be easily changed depending upon the different patient organ geometry.

There are large variations in the tissue inclusion parameter estimation errors. The one reason of this is because of the variation of the ANN performance. In this research, we utilized the Scaled Conjugate Gradient algorithm (SCGA) as the ANN learning algorithm for its simplicity and low complexity. Despite of its advantages, however, we found that the SCGA fails to find the final optimal solution of ANN in some cases. In future works, we will consider to use advanced ANN learning algorithm such as Levenberg-Marquardt algorithm (LMA). The LMA interpolates between the Gauss-Newton algorithm (GNA) and the gradient descent method. The LMA is more robust than the GNA, which means that in many cases it finds an optimal solution even if it starts very far off the final minimum. We believe that if we use the advanced ANN learning algorithm, the final parameter estimation error will be decreased.

In the future, we will consider SVM model with three different data sets (normal, benign, and malignant of a tissue inclusion) having multiple dimensional feature spaces (size, depth, and Young's modulus of a tissue inclusion) for classification. Prior to classification, detailed statistical analyses of tactile data obtained from the TSIS will also be performed for normal (no tumor), benign, and malignant.

Higher-Dimensional, Multi-class classification

In the previous example, we had only two variables, and we were able to plot the data on a 2-D plane. If we add a third variable, then we can use its value for a third dimension and plot the data in a 3-D cube. Data on a 2-D plane can be separated by a 1-D line. Similarly, data in a 3-D cube can be separated by a 2-D plane. To classify three data sets (negative, benign, and malignant of a tissue inclusion), a 3-D SVM should be used. In this example, 1st data can be the size of the tumor, 2nd data can be the depth of the tumor, and 3rd data can be the Young's modulus of the tissue inclusion.

Although the SVM algorithm is normally adapted for discriminating data from the two classes, it can also easily be converted into a classification algorithm with multiple classes. In future work, we shall find the most optimal and ultimate hyperplane decision method to classify three classes (negative, benign, and malignant of a tissue inclusion) using 3-D data (size, depth, and Young's modulus of a tissue inclusion).

REFERENCES

Achilles, E. (1993). Implications of convergence rates in sinkhorn balancing. *Linear Algebra and its Applications*, 187(1):109–112.

Altman, D. G. and Bland, J. M. (1994). Diagnostic tests. 1: Sensitivity and specificity. *British Medical Journal*, 308(6943):1552.

Balsky, M. F., Lindner, D. K., and Claus, R. O. (1989). Robot gripper control system using pvdf piezoelectric sensors. *IEEE Transactions on Ultrasonics, Ferroelectrics, and Frequency Control*, 36(1):129–134.

Beebe, D. J., Hsieh, A. S., Denton, D. D., and Radwin, R. G. (1995). A silicon force sensor for robotics and medicine. *Sensors and Actuators A: Physical*, 50(1-2):55–65.

Begej, S. (1988). Planar and finger shaped optical tactile sensors for robotic applications. *IEEE Journal Robotics and Automation*, 4(5):472–484.

Belongie, S., Malik, J., and Puzicha, J. (2002). Shape matching and object recognition using shape contexts. *IEEE Transactions on Pattern Analysis and Machine Intelligence*, 24(4):509–522.

Besl, P. J. and Mckay, N. (1992). A method for registration of 3-d shapes. *IEEE Transactions on Pattern Analysis and Machine Intelligence*, 14(2):239–256.

Bhatia, K. S., Rasalkar, D. D., Lee, Y. P., Wong, K. T., King, A. D., Yuen, Y. H., and Ahuja, A. T. (2010). Real-time qualitative ultrasound elastography of miscellaneous non-nodal neck masses: applications and limitations. *Ultrasound in Medicine and Biology*, 36(10):1644–1652.

Bishop, C. M. (2007). *Pattern Recognition and Machine Learning*. Springer.

Bluemke, D. A., Gatsonis, C. A., Chen, M. H., DeAngelis, G. A., DeBruhl, N., Harms, S., Heywang-Kobrunner, S. H., Hylton, N., Kuhl, C. K., Lehman, C., Pisano, E. D., Causer, P., Schnitt, S. J., Smazal, S. F., Stelling, C. B., Weatherall, P. T., and Schnall, N. D. (2004). Magnetic resonance imaging of the breast prior to biopsy. *Journal of the American Medical Association*, 292(22):2735–2742.

Bobo, J. K., Lee, N. C., and Thames, S. F. (2000). Findings from 752,081 clinical breast examinations reported to a national screening program from 1995 through 1998. *Journal of National Cancer Institute*, 92(12):971–976.

Bookstein, F. L. (1989). Principal warps: thin-plate splines and the decomposition of deformations. *IEEE Transactions on Pattern Analysis and Machine Intelligence*, 11(6):567–585.

Boyd, R. W. (2008). *Nonlinear optics*. Academic press.

Brown, L. G. (1992). A survey of image registration techniques. *ACM Computing Surveys*, 24(4):326–376.

Bruck, H. A., McNeill, S. R., Sutton, M. A., and Peters, W. H. (1989). Digital image correlation using newton-raphson method of partial differential correction. *Experimental Mechanics*, 29(3):261–267.

Byvatov, E. and Schneider, G. (2003). Support vector machine applications in bioinformatics. *Applied Bioinformatics*, 2(2):67–77.

Canny, J. (1986). A computational approach to edge detection. *IEEE Transactions on Pattern Analysis and Machine Intelligence*, 8(6):679–698.

Carney, P. A., Miglioretti, D. L., Yankaskas, B. C., K. Kerlikowske, R. R., Ruffer, C. M., Geller, B. M., Abraham, L. A., Taplin, S. H., Dignan, M., Cutter, G., and Barbash, R. (2003). Individual and combined effects of age, breast density, and hormone replacement therapy use on the accuracy of screening mammography. *Annals of Internal Medicine*, 138(3):168–175.

Chang-Yen, D. A., Eich, R. K., and Gale, D. W. (2005). A monolithic pdms waveguide system fabricated using soft-lithography techniques. *Journal of Lightwave Technology*, 23(6):2088–2093.

Cheung, E. and Lumelsky, V. (1992). A sensitive skin system for motion control of robot arm manipulators. *Robotics and Autonomous Systems*, 10(1):9–32.

Chu, Z., Sarro, P. M., and Middlehoek, S. (1996). Silicon three-axial tactile sensor. *Sensors and Actuators A: Physical*, 54(1–3):505–510.

Craig, J. C. and Baihua, X. (1990). Temporal order and tactile patterns. *Perception and Phychophysics*, 47(1):22–34.

Dargahi, J. and Najarian, S. (2004). Human tactile perception as a standard for artificial tactile sensing - a review. *International Journal of Medical Robotics and Computer Assisted Surgery*, 1(1):23–35.

Dargahi, J., Najarian, S., Ramezanifard, R., and Ghomshe, F. T. (2007). Fabrication and testing of a medical surgical instrument capable of detecting simulated embedded lumps. *American Journal of Applied Sciences*, 4(12):957–964.

Dargahi, J., Parameswaran, M., and Payandeh, S. (2000). A micromachined piezoelectric tactile sensor for an endoscopic grasper - theory, fabrication and experiments. *Journal of Microelectromechanical Systems*, 9(3):329–335.

Dario, P. and Rossi, D. D. (1985). Tactile sensors and the gripping challenge. *IEEE Spectrum*, 22(8):46–52.

Darvish, K. (2009). Comparison between the dynamic moduli of fully non-linear and quasi-linear viscoelastic materials. *International Journal of Non-Linear Mechanics*, 44(2):239–243.

Degani, H., Gusis, V., Weinstein, D., Fields, S., and Strano, S. (1997). Mapping pathophysiological features of breast tumors by mri at high spatial resolution. *Nature Medicine*, 3(7):780–782.

DiLella, D., Whiteman, L. J., Colton, R. J., Kenny, T. W., Kaiserc, W. J., Vote, E. C., Rodosek, J. A., and Miller, L. M. (2000). A micromachined magnetic field sensor based on an electron tunneling displacement transducer. *Sensors and Actuators A: Physics*, 86(1–2):8–20.

Egorov, V. and Savazyan, A. P. (2008). Mechanical imaging of the breast. *IEEE Transactions on Medical Imaging*, 27(9):1275–1287.

Eltaib, M. and Hewit, J. (2003). Tactile sensing technology for minimal access surgery - a review. *Mechatronics*, 13(10):1163–1177.

Engel, J., Chen, J., and Liu, C. (2003). Development of polyimide flexible tactile sensor skin. *Journal of Micromechanics and Microengineering*, 13(3):359–366.

Fearing, R. S. (1990). Tactile sensing mechanism. *The International Journal of Robotics Research*, 9(3):3–23.

Fearing, R. S. and Binford, T. O. (1988). Using a cylindrical tactile sensor for determining curvature. *IEEE Transactions on Robotics and Automation*, 7(6):765–771.

Fenster, A. and Downey, D. B. (1996). 3-D ultrasound imaging: a review. *IEEE Engineering in Medicine and Biology Magazine*, 15(6):41–51.

Ferrier, N. J. and Brockett, R. W. (2000). Reconstructing the shape of a deformable membrane from image data. *The International Journal of Robotics Research*, 19(9):795–816.

Filonenko-Borodichm, M. (1965). *Theory of Elasticity*. Dover.

Flynn, C. O. and McCormack, B. A. (2009). A three-layer model of skin and its application in simulating wrinkling. *Computer Methods in Biomechanics and Biomedical Engineering*, 12(2):125–134.

Fung, Y. C. (1993). *Biomechanics: Mechanical properties of living tissues*. New York, Springer Verlag.

Futai, N., Matsumoto, K., and Shimoyama, I. (2004). A flexible micromachined planar spiral inductor for use as an artificial tactile mechanoreceptor. *Sensors and Actuators A: Physical*, 111(2-3):293–303.

Galea, A. M. (2004). *Mapping tactile imaging information: Parameter estimation and deformable registration*. Ph.d. dissertation, harvard university.

Gao, L., Parker, K. J., Lerner, R. M., and Levinson, S. F. (1996). Imaging of the elastic properties of tissue - a review. *Ultrasound in Medicine and Biology*, 22(8):959–977.

Garra, B. S., Cespedes, E. I., Ophir, J., Spratt, S. R., Zuurbier, R. A., Magnant, C. M., and Pennanen, M. F. (1997). Elastography of breast lesions: Initial clinical results. *Radiology*, 202(1):79–86.

Gautherie, M. and Gros, C. M. (1980). Breast thermography and cancer risk prediction. *Cancer*, 45(1):51–56.

Gentle, C. R. (1988). Mammobarography: a possible method of mass breast screening. *Journal of Biomedical Engineering*, 10(2):124–126.

Giessibi, F. J. (2003). Advances in atomic force microscopy. *Reviews of Modern Physics*, 75(3):949–983.

Golub, T. R., Slonim, D. K., Tamayo, P., Huard, C., Gaasenbeek, M., Mesirov, J. P., Coller, H., Loh, M. L., Downing, J. R., Caligiuri, M. A., Bloomfield, C. D., and Lander, E. S. (1999). Molecular classification of cancer: class discovery and class prediction by gene expression monitoring. *Science*, 286(5439):531–537.

Gotzsche, D. C. and Olsen, O. (2000). Is screening for breast cancer with mammography justifiable? *Lancet*, 355(9198):129–134.

Gupta, G. S., S. C. Mukhopadhray, C. H. M., and Demidenko, S. N. (2006). Masterslave control of a teleoperated anthropomorphic robotic arm with gripping force sensing. *IEEE Transactions on Instrumentation and Measurement*, 55(6):2136–2145.

Hackwood, S., Beni, G., Hornak, L. A., Wolfe, R., and Nelson, T. J. (1983). A torque-sensitive tactile array for robotics. *The International Journal of Robotics Research*, 2(2):46–50.

Hartigan, J. A. and Wong, M. A. (1979). A k-means clustering algorithm. *Journal of the Royal Statistical Society. Series C (Applied Statistics)*, 28(1):100–108.

He, X. C. and Yung, N. H. C. (2008). Corner detector based on global and local curvature properties. *Optical Engineering*, 47(5):057008.

Heever, D. J., Schreve, K., and Scheffer, C. (2009). Tactile sensing using force sensing resistors and a super-resolution algorithm. *IEEE Sensors Journal*, 9(1):29–35.

Heo, J.-S., Chung, J.-H., and Lee, J.-J. (2006). Tactile sensor arrays using fiber bragg grating sensors. *Sensors and Actuators A: Physics*, 126(2):312–327.

Hosoda, K., Tada, Y., and Asada, M. (2006). Anthropomorphic robotic soft fingertip with randomly distributed receptors. *Robotics and Autonomous Systems*, 54(2):104–109.

Howe, R. D. and Matsuoka, Y. (1999). Robotics for surgery. *Annual Review of Biomedical Engineering*, 1:211–240.

Howe, R. D., Peine, W. J., Kontarinis, D. A., and Son, J. S. (1995). Remote palpation technology surgical applications. *IEEE Engineering in Medicine and Biology Magazine*, 14(3):318–323.

Hoyt, K., Forsberg, F., and Ophir, J. (2006). Comparison of shift estimation strategies in spectral elastography. *Ultrasonics*, 44(1):99–108.

Huber, S., Wagner, M., Medl, M., and Czembirek, H. (2002). Realtime spatial compound imaging in breast ultrasounds. *Ultrasound in Medicine and Biology*, 28(2):155–163.

Hummel, R. A. and Zucker, S. W. (1983). On the foundations of relaxation labeling processes. *IEEE Transactions on Pattern Analysis and Machine Intelligence*, 5(3):267–287.

Hwang, E.-S., Seo, J.-H., and Kim, Y.-J. (2007). A polymer-based flexible tactile sensor for both normal and shear load detections and its application for robotics. *Journal OF Microelectromechanical Systems*, 16(3):556–563.

Insana, M. F., Pellot-Barakat, C., Sridhar, M., and Lindfors, K. K. (2004). Viscoelastic imaging of breast tumor microenvironment with ultrasound. *Journal of Mammary Gland Biology and Neoplasia*, 9(4):393–404.

Itoh, A., Ueno, E., Tohno, E., Kamma, H., Takahashi, H., Shiina, T., Yamakawa, M., and Matsumura, T. (2006). Breast disease: Clinical application of us elastography for diagnosis. *Radiology*, 239(2):341–350.

Jayawant, B. V. (1989). Tactile sensing in robotics. *Journal of Physics E: Scientific Instruments*, 22(9):684–692.

Jemal, A., Siegel, R., Ward, E., Xu, Y. H. J., and Thun, M. J. (2009). Cancer statistics, 2009. *CA: A Cancer Journal for Clinicians*, 59(4):225–249.

Jian, B. and Vemuri, B. (2005). A robust algorithm for point set registration using mixture of gaussians. In *IEEE International Conference on Computer Vision*.

Johannson, R. S. and Vallbo, A. B. (1979). Tactile sensibility in the human hand relative and absolute densities of four types of mechanoreceptive units in glabrous skin. *The Journal of Physiology*, 286:283–300.

Johanson, K. O. and Philips, J. R. (1981). Tactile spatial resolution. i. two-point discrimination, gap detection, grating resolution, and letter recognition. *Journal of Neurophysiology*, 46(6):1177–1191.

Johnson, H. J. and Christensen, G. E. (2002a). Consistent landmark and intensity-based image registration. *IEEE Transactions on Medical Imaging*, 21(5):450–461.

Johnson, H. J. and Christensen, G. E. (2002b). Consistent landmark and intensity-based image registration. *IEEE Transactions on Medical Imaging*, 21(5):450–461.

Johnson, K. O. and Hsiao, S. S. (1992). Neural mechanisms of tactual form and texture perception. *Annual Review of Neuroscience*, 15:227–250.

Johnson, R. A. (2007). *Advancer euclidean geometry*. Dover.

Kamangar, F., Dores, G. M., and Anderson, W. F. (2006). Patterns of cancer incidence, mortality, and prevalence across five continents: defining priorities to reduce cancer disparities in different geographic regions of the world. *Journal of Clinical Oncology*, 24(14):2137–2150.

Kamiyama, K., Kajimoto, H., Inami, M., Kawakami, N., and Tachi, S. (2003). Development of a vision-based tactile sensor. *IEEJ Transactions on Sensors and Micromachines*, 123(1):16–22.

Kandel, E., Schwartz, J., and Jessell, T. (2000). *Principles of neural science*. McGraw-Hill Medical.

Karahaliou, A. N., Boniatis, I. S., Skiadopoulos, S. G., Sakellaropoulos, F. N., Arikidis, N. S., Likaki, E. A., Panayiotakis, G. S., and Costaridou, L. I. (2008). Breast cancer diagnosis: analyzing texture of tissue surrounding microcalcifications. *IEEE Transactions on Information Technology in Biomedicine*, 12(6):731–738.

Katz, M. (2002). *Introduction to geometrical optics*. World Scientific.

Keiser, G. (1999). *Optical fiber communications*. McGraw-Hill Science / Engineering / Math.

Kim, S.-H., Engel, J., Liu, C., and Jones, D. L. (2005). Texture classification using a polymer-based mems tactile sensor. *Journal of Micromechanics and Microengineering*, 15(5):912–920.

Koh, H., Yasunori, T., and Minoru, A. (2006). Anthropomorphic robotic soft fingertip with randomly distributed receptors. *Robotics and Autonomous Systems*, 54(2):104–109.

Kolesar, E. S. and Dyson, C. S. (1995). Object imaging with a piezoelecrtic robotic tactile sensor. *Journal of Micromechanical Systems*, 4(2):87–96.

Kotoulas, L. and Andreadis, I. (2007). Accurate calculation of image moments. *IEEE Transactions on Image Processing*, 16(8):2028–2037.

Krishna, G. M. and Rajanna, K. (2004). Tactile sensor based on piezoelectric resonance. *IEEE Sensors Journal*, 4(5):691–697.

Krouskop, T. A., Wheeler, T. M., Kallel, F., Garra, B. S., and Hall, T. (1998). Elastic moduli of breast and prostate tissues under compression. *Ultrasonic Imaging*, 20(4):260–274.

Lamotte, R. H. and Srinivasan, M. A. (1987). Tactile discrimination of shape: responses of slowly adapting mechanoreceptive afferents to a step stroked across the monkey fingerpad. *The Journal of Neuroscience*, 7(6):1672–1681.

Lee, H.-K., Chang, S.-I., and Yoon, E. (2006). A flexible polymer tactile sensor: fablication and modular expandability for large area development. *Journal of Microelectromechanical Systems*, 15(6):1681–1686.

Lee, J.-H., Garcia-Acosta, N., Te, K., and Won, C.-H. (2011). Tactile sensation imaging system for inclusion mechanical property characterization. In *SPIE, Photonics West 2011*.

Lee, J.-H. and Won, C.-H. (2011a). High resolution tactile imaging sensor using total internal reflection and non-rigid pattern matching algorithm. *IEEE Sensors Journal*.

Lee, J.-H. and Won, C.-H. (2011b). Topology preserving relaxation labeling for non-rigid point matching. *IEEE Transactions on Pattern Analysis and Machine Intelligence*, 33(2):427–432.

Lee, J.-H., Won, C.-H., and Kong, S. (2008). Estimation of operative line of resection using preoperative image and non-rigid registration. In *Annual International Conference of the IEEE Engineering in Medicine and Biology Society*.

Lee, J.-H., Won, C.-H., and Marchetti, N. (2010a). Determining the operative line of resection for image-guided emphysema surgery using a laser scanner and non-rigid registration. *International Journal of Medical Robotics and Computer Assisted Surgery*, 6(2):239–249.

Lee, J.-H., Won, C.-H., Yan, K., and Yu, Y. (2010b). Artificial tactile sensing for healthcare application. In *2010 US-Korea Conference on Science, Technology, and Entrepreneurship*.

Lee, J.-H., Won, C.-H., Yan, K., and Yu, Y. (2010c). Design and evaluation of an optical tactile imaging device for tumor detection. *Medical Physics*, 37(6):2139.

Lee, M. H. (2000). Tactile sensing: new direction, new challenges. *The International Journal of Robotics Research*, 19(7):636–643.

Lee, M. H. and Nicholls, H. R. (1999). Review article tactile sensing for mechatronics – a state of the art survey. *Mechatronics*, 9(1):1–31.

Leineweber, M., Pelz, G., Schmidt, M., Kappert, H., and Zimmer, G. (2000). New tactile sensor chip with silicone rubber cover. *Sensors and Actuators A: Physical*, 84(3):236–245.

Lind, P., Igerc, I., Beyer, T., Reinprecht, P., and Hausegger, K. (2004). Advantages and limitations of fdg pet in the follow-up of breast cancer. *European Journal of Nuclear Medicine and Molecular Imaging*, 31(1):125–134.

MedicalTactile (2011). Medical tactile. *Electronic Sources: http://www.medicaltactile.com/*.

Metz, C. E. (1978). Basic principles of roc analysis. *Seminars in nuclear medicine*, 8(4):283–298.

Mommography (2011). Mommography. *Electronic Sources: http://www.camoodle.org/*.

Morimura, H., Shigematsu, S., and Machinda, K. (2000). A novel sensor cell architecture and sensing circuit scheme for capacitive fingerprint sensors. *IEEE Journal of Solid-State Circuits*, 35(5):724–731.

MRI (2011). Magnetic resonance imaging technique. *Electronic Sources: http://www.cyclindevelopment.com/for-entrepreneurs-2/case-studies/*.

Mushlin, A. I., Kouides, R. W., and Shapiro, D. E. (1998). Estimating the accuracy of screening mammography: A meta-analysis. *American Journal of Preventive Medicine*, 14(2):143–153.

Myronenko and Song, X. (2010). Point set registration: Coherent point drift. *IEEE Transactions on Pattern Analysis and Machine Intelligence*, 32(12):2262–2275.

Najarian, S., Dargahi, J., and Mehrizi, A. A. (2009). *Artificial tactile sensing in biomedical engineering*. McGraw-Hill.

Najarian, S., Dargahi, J., and Zheng, X. Z. (2006). A novel method in measureing the stiffness of sensed objects with applications for biomedical robotic systems. *International Journal of Medical Robotics and Computer Assisted Surgery*, 2(1):84–90.

Niemisto, A., Korpelainen, T., Saleem, R., Yli-Harja, O., Aitchison, J., and Shimulevich, I. (2007). A k-means segmentation method for finding 2-d object areas based on 3-d image stacks obtained by confocal microscopy. In *Annual International Conference of the IEEE Engineering in Medicine and Biology Society*.

Ohka, M., Mitsuya, Y., Matsunaga, Y., and Takeuchi, S. (2004). Sensing characteristics of optical three-axis tactile sensor under combined loading. *Robotica*, 22(2):213–221.

Ohmura, Y., Kuniyoshi, Y., and Nagakubo, A. (2006). Conformable and scalable tactile sensor skin for curved surfaces. In *IEEE International Conference on Robotics and Automation*.

Olsen, O. and Gotzsche, P. C. (2001). Cochrane review on screening for breast cancer with mammography. *Lancet*, 358(9290):1340–1342.

Ong, K. G., Tan, E. L., Pereles, B., and Horton, B. (2009). Wireless, magnetic-based sensors for biomedical applications. In *Annual International Conference of the IEEE Engineering in Medicine and Biology Society*.

Ophir, J., Cespedes, I., Pennekanti, H., Yazdi, Y., and Li, X. (1991). Elastography, a quantitative method for imaging the elasticity of biological tissues. *Ultrasound in Medicine*, 13(2):111–134.

Orel, S. G. and Schnall, M. D. (2001). Mr imaging of the breast for the detection, diagnosis, and staging of breast cancer. *Radiology*, 220(1):13–30.

Parisky, Y. R., Sardi, A., Hamm, R., Hughes, K., Esserman, L., Rust, S., and Callahan, K. (2003). Efficacy of computerized infrared imaging analysis to evaluate mammographically suspicious lesions. *American Journal of Roentgenology*, 180(1):263–269.

Parker, K. J., Huang, S. R., Musulin, R. A., and Lerner, R. M. (1990). Tissue response to mechanical vibrations for sonoelasticity imaging. *Ultrasound in Medicine and Biology*, 16(3):241–246.

Peleg, S. and Rosenfeld, A. (1978). Determining compatibility coefficients for curve enhancement relaxation processes. *IEEE Transactions on Systems, Man and Cybernetics*, 8(7):548–555.

Pelillo, M. and Refice, M. (1994). Learning compatibility coefficients for relaxation labeling processes. *IEEE Transactions on Pattern Analysis and Machine Intelligence*, 16(9):933–945.

Picard, R. and Cook, D. (1984). Cross-validation of regression models. *Journal of the American Statistical Association*, 79(387):575–583.

Pirznieks, I., Jehmalm, P., Goodwin, A. W., and Johannson, R. S. (2001). Encoding of direction of fingertip forces by human tactile afferents. *The Journal of Neuroscience*, 21(20):8222–8237.

Rahbar, G., Sie, A., Hansen, G., Prince, J., Melany, M., Reynolds, H., Jackson, V., Sayre, J., and Bassett, L. (1999). Benign versus malignant solid breast masses: Us differentiation. *Radiology*, 213(3):889–894.

Rajan, G. S., Sur, G. S., Mark, J. E., Schaefer, D. W., and Beaucage, G. (2003). Preparation and characterization of some unusually transparent poly (dimethylsiloxane) nanocomposites. *Journal of Polymer Science Part B: Polymer Physics* , 41(16):1897–1901.

Rangarajan, A., Chui, H., and Bookstein, F. (1997). The softassign procrustes matching algorithm. *Information Processing in Medical Imaging*, pages 29–42.

Rangarajan, A., Chui, H., and Duncan, J. S. (1999). Rigid point feature registration using mutual information. *Medical Image Analysis*, 3(4):425–440.

Rangarajan, A., Gold, S., and Mjolsness, E. (1996). A novel optimizing network architecture with applications. *Neural Computation*, 8(5):1041–1060.

Rangayan, R. M. (2005). *Biomedical image analysis*. CRC Press.

Ratanachaikanont, T. (2005a). Clinical breast examination and its relevance to diagnosis of palpable breast lesion. *Journal of the Medical Association of Thailand*, 88(4):505–507.

Ratanachaikanont, T. (2005b). Clinical breast examination and its relevance to diagnosis of palpable breast lesion. *Journal of The Medical Association of Thailand*, 88(4):505–507.

Raza, S. and Baum, K. (1997). Solid breast lesions: evaluation with power doppler us. *Radiology*, 203(1):164–168.

Regini, E., Bagnera, S., Tota, D., Campanino, P., Luparia, A., Barisone, F., Durando, M., Mariscotti, G., and Gandini, G. (2010). Role of sonoelastography in characterising breast nodules. preliminary experience with 120 lesions. *Radiology Medicine*, 115(4):551–562.

Rico-Secades, M., Calleja, A. J., Ribas, J., Corominas, E. L., Alonso, J. M., Cardesin, J., and Garcia-Garcia, J. (2005). Evaluation of a low-cost permanent emergency lighting system based on high-efficiency leds. *IEEE Transactions on Industry Applications*, 41(5):1386–1390.

Rivaz, H., Boctor, E., Foroughi, P., Zellars, R., Fichtinger, G., and Hager, G. (2008). Ultrasound elastography: a dynamic programming approach. *IEEE Transactions on Medical Imaging*, 27(10):1373–1377.

Rogowska, J., Patel, N. A., Fujimoto, J. G., and Brezinski, M. E. (2004). Optical coherence tomographic elastography technique for measuring deformation and strain of atherosclerotic tissues. *Heart*, 90(5):556–562.

Roques, F., Nashef, S. A. M., Michel, P., Pintor, P., and Baudet, D. E. (2000). Does euroscore work in individual european countries? *European Journal of Cardio-thoracic Surgery*, 18(1):27–30.

Rosenfeld, A., Hummel, R. A., and Zucker, S. W. (1976). Scene labeling by relaxation operations. *IEEE Transactions on Systems, Man and Cybernetics*, 6(6):420–433.

Rossi, D. D. and Domenici, C. (1986). Piezoelectric properties of dry human skin. *IEEE Transactions on Electrical Insulation*, EI-21(3):511–517.

Saga, S., Kajimoto, H., and Tachi, S. (2007). High-resolution tactile sensor using the deformation of a reflection image. *Sensor Review*, 27(1):35–42.

Saleh, B. E. and Teich, M. C. (1991). *Fundamentals of photonics*. Wiley-Interscience.

Samaun, Wise, K. D., and Angell, J. B. (1973). An ic piezoresistive pressure sensor for biomedical instrumentation. *IEEE Transactions on Biomedical Engineering*, BME-20(2):101–109.

Saxena, A., Driemeyer, J., and Ng, A. (2008). Robotic grasping of novel objects using vision. *The International Journal of Robotics Research*, 27(2):157–173.

Schaffner, F., Wellscheid, R., and Jungnickel, B.-J. (1991). The hydrostatic piezoelectric coefficient of pvdf/pmma blends. *IEEE Transactions on Electrical Insulation*, 26(1):78–84.

Schmidt, P., Maeil, E., and Wurtz, R. (2006). A sensor for dynamic tactile information with applications in human-robot interaction and object exploration. *Robotics and Autonomous Systems*, 54(12):1005–1014.

Sehgal, C. M., Weinstein, S. P., Arger, P. H., and Conant, E. F. (2006). A review of breast ultrasound. *Journal of Mammary Gland Biology and Neoplasia*, 11(2):113–123.

Shipp, M. A., Ross, K. N., Tamayo, P., Weng, A. P., Kutok, J. L., Aguiar, R. C., Gaasenbeek, M., Angelo, M., Reich, M., Pinkus, G. S., Ray, T. S., Koval, M. A., Last, K. W., Norton, A., Lister, T. A., Mesirov, J., Neuberg, D. S., Lander, E. S., Aster, J. C., and Golub, T. R. (2002). Diffuse large b-cell lymphoma outcome prediction by gene expression profiling and supervised machine learning. *Nature Medicine*, 8(1):68–74.

Shojaku, H., Seto, H., Iwai, H., Kitazawa, S., Fukushima, W., and Saito, K. (2008). Detection of incidental breast tumors by noncontrast spiral computed tomography of the chest. *Radiation Medicine*, 26(6):362–367.

Siemens (2011). Ultrasound elastography technique. *Electronic Sources: http://www.medicaltactile.com/*.

Sridhar, M. and Insana, M. F. (2007). Ultrasonic measurements of breast viscoelasticity. *Medical Physics*, 34(12):4757–4767.

Stravros, A., Thickman, D., Dennis, M., Parker, S., and Sisney, G. (2011). Solid breast nodules: Use of sonography to distinguish between benign and malignant lesions. *Radiology*, 259(1):123–134.

Thermography (2011). Breast thermography technique. *Electronic Sources: http://www.breastthermography.biz/*.

Thitaikumar, A., Mobbs, L. M., Kraemer-Chant, C. M., Garra, B. S., and Ophir, J. (2008). Breast tumor classification using axial shear strain elastography: a feasibility study. *Physics in Medicine and Biology*, 53(17):4810–4823.

Tsin, Y. and Kanade, T. (2004). A correlation-based approach to robust point set registration. *Proceedings of the 8th European Conference on Computer Vision*, pages 558–569.

Ultrasound (2011). Ultrasound. *Electronic Sources: http://www.breastcancerimaging.com/.*

Uttal, W. R. (1973). *The psychology of sensory coding*. Harper and Row Publishing Co.

Vapnik, V. (1995). *The Nature of Statistical Learning Theory*. Springer-Verlag New York, Inc.

Vinckier, A. and Semenza, G. (1998). Measuring elasticity of biological materials by atomic force microscopy. *FEBS Letters*, 430(1–2):12–16.

Wang, Z. G., Liu, Y., Wang, G., and Sun, L. Z. (2009). Elastography method for reconstruction of nonlinear breast tissue properties. *International Journal of Biomedical Imaging*, 2009.

Weber, G. (2000). *Using tactile images to differentiate breast cancer types*. Ph.d. dissertation, harvard university.

Webster, J. G. (1988). *Tactile sensors for robotics and medicine*. John Wiley & Sons, Inc,.

Wellman, P. S., Dalton, E. P., Krag, D., Kern, K. A., and Howe, R. D. (2001a). Tactile imaging of breast masses: First clinical report. *Archives of Surgery*, 136(2):204–208.

Wellman, P. S., Dalton, E. P., Krag, D., Kern, K. A., and Howe, R. D. (2001b). Tactile imaging of breast masses: First clinical report. *Archives of Surgery*, 136(2):204–208.

Wu, Q. X. and Pairman, D. (1995). A relaxation labeling technique for computing sea surface velocities from sea surface temperature. *IEEE Transactions on Geoscience and Remote Sensing*, 33(1):216–220.

Yates, T. D., Hebden, J. C., Gibson, A. P., Enfield, L., Everdell, N. L., Arridge, S. R., and Delpy, D. T. (2005). Time-resolved optical mammography using a liquid coupled interface. *Journal of Biomedical Optics*, 10(5):054011.

Yegingil, H., Shih, W. Y., and Shih, W.-H. (2007). All-electrical palpation shear modulus and elastic modulus measurement using a piezoelectric cantilever with a tip. *Journal of Applied Physics*, 101(5):054510.

Yegingil, H., Shih, W. Y., and Shih, W. H. (2010). Probing model tumor interfacial properties using piezoelectric cantilevers. *Review of Scientific Instruments*, 81(9):095104.

Zhang, H. and Chen, N. N. (2000). Control of contact via tactile sensing. *IEEE Transactions on Robotics and Automation*, 16(5):482–495.

Zheng, Y. and Doermann, D. (2006). Robust point matching for nonrigid shapes by preserving local neighborhood structures. *IEEE Transactions on Pattern Analysis and Machine Intelligence*, 28(4):643–649.

Zitova, B. (2003). Image registration methods: A survey. *Image and Vision Computing*, 21(11):977–1000.